GEOMETRY OF INERTIAL MANIFOLDS IN NONLINEAR DISSIPATIVE DYNAMICAL SYSTEMS

A Thesis
Presented to
The Academic Faculty

by

Xiong Ding

In Partial Fulfillment
of the Requirements for the Degree
Doctor of Philosophy in the
School of Physics

Georgia Institute of Technology
version 2.0 April 3 2017

ACKNOWLEDGEMENTS

I would like to sincerely thank my advisor Prof. Predrag Cvitanović for his persistent and patient guidance in the past few years. He introduced me to the research of chaos, a fascinating field of physics. And I learned a lot from him about turbulence theory, cycle-averaging theory, group theory and so on. I really appreciate the resources he is providing for graduate students working at *Center for Nonlinear Science* at *Georgia Tech*. Especially, I admire his attitude of regarding studying and researching as lifetime habits.

At the same time, I thank everyone who has assisted my research. I thank Prof. Flavio Fenton for his guidance on the heart dynamics when I was trying different research topics. I thank Prof. Luca Dieci for his valuable suggestions on the periodic eigendecomposition algorithm. I thank Prof. Sung Ha Kang for her guidance in the adaptive time-stepping exponential integrators. I thank my colleague Matthew Gudorf for proofreading my thesis. I thank my classmate Nazmi Burak Budanur for the discussions of symmetry reduction. I thank Mohammad Farazmand, Christopher Marcotte, Han Li, Simon Berman, Kimberly Short, Pallantla Ravi Kumar and other colleagues for all the enlightening discussions.

At last, I thank my parents for insisting that I pursue higher education, and the efforts they made to make it possible.

TABLE OF CONTENTS

LIST OF TABLES

LIST OF FIGURES

SUMMARY

High- and infinite-dimensional nonlinear dynamical systems often exhibit complicated flow (spatiotemporal chaos or turbulence) in their state space (phase space). Sets invariant under time evolution, such as equilibria, periodic orbits, invariant tori and unstable manifolds, play a key role in shaping the geometry of such system's longtime dynamics. These invariant solutions form the backbone of the global attractor, and their linear stability controls the nearby dynamics.

In this thesis we study the geometrical structure of inertial manifolds of nonlinear dissipative systems. As an exponentially attracting subset of the state space, inertial manifold serves as a tool to reduce the study of an infinite-dimensional system to the study of a finite set of determining modes. We determine the dimension of the inertial manifold for the one-dimensional Kuramoto-Sivashinsky equation using the information about the linear stability of system's unstable periodic orbits. In order to attain the numerical precision required to study the exponentially unstable periodic orbits, we formulate and implement "periodic eigendecomposition", a new algorithm that enables us to calculate all Floquet multipliers and vectors of a given periodic orbit, for a given discretization of system's partial differential equations (PDEs). It turns out that the O(2) symmetry of Kuramoto-Sivashinsky equation significantly complicates the geometrical structure of the global attractor, so a symmetry reduction is required in order that the geometry of the flow can be clearly visualized. We reduce the continuous symmetry using so-called slicing technique. The main result of the thesis is that for one-dimensional Kuramoto-Sivashinsky equation defined on a periodic domain of size $L = 22$, the dimension of the inertial manifold is 8, a number considerably smaller that the number of Fourier modes, 62, used in our simulations.

Based on our results, we believe that inertial manifolds can, in general, be approximately constructed by using sufficiently dense sets of periodic orbits and their linearized neighborhoods. With the advances in numerical algorithms for finding periodic orbits in chaotic/turbulent flows, we hope that methods developed in this thesis for a one-dimensional nonlinear PDE, i.e., using periodic orbits to determine the dimension of an inertial manifold, can be ported to higher-dimensional physical nonlinear dissipative systems, such as Navier-Stokes equations.

CHAPTER I

INTRODUCTION

The study of nonlinear dynamics covers a huge range of research topics. In this thesis, we focus on the geometric or topological structures and statistic averages of dissipative systems. The progress in this area comes from collaborative contributions from both applied mathematicians and physicists, from both theoretical and numerical aspects. In this chapter, we introduce the mathematical framework to study the finite-dimensional behavior embedded in an infinite-dimensional function space of dissipative systems described by nonlinear partial differential equations (PDEs). In particular, we review the recent progress in use of "covariant vectors" for investigating the dimensionality of chaotic systems. We also focus on the important role that invariant structures such as periodic orbits play in the description of chaotic dynamics and review the *cycle averaging theory* [22] for calculating statistical properties of chaotic dynamical systems.

1.1 Overview of the thesis and its results

This thesis is organized as follows. In Chapter 1, we recall some basic facts about dissipative dynamical systems relevant to this thesis, the traditional types of fractal dimensions, and introduce the concept of the inertial manifold. We review the literature on estimating the dimension of inertial manifolds by covariant (Lyapunov) vectors, and related algorithms. Chapter 2 is devoted to the discussion of symmetries in dynamical systems. A reader who is familiar with the group representation theory can skip Sect. 2.1. Sect. 2.2 discusses the slicing technique we use to reduce continuous symmetries of dynamical systems, and the tangent dynamics in the slice. Methods of Chapter 2 are a prerequisite to the calculations of Chapter 3, where we study invariant structures in the symmetry-reduced state space of the one-dimensional Kuramoto-Sivashinsky equation. Chapter 4 contains the main result of this thesis. We investigate the dimension of the inertial manifold in the one-dimensional Kuramoto-Sivashinsky equation using the information about the linear stability of pre/relative periodic orbits of the system. Chapter 5 introduces our periodic eigendecomposition algorithm, essential tool for computation of the Floquet multipliers and Floquet vectors reported in Chapter 4. Readers not interested in the implementation details can go directly to Sect. 5.5, where the performance of the algorithm is reported. We summarize our results and outline some future directions in Chapter 6.

The original contributions of this thesis are mainly contained in Chapter 4 and Chapter 5. The periodic eigendecomposition introduced in Chapter 5 is capable of resolving Floquet multipliers as small as $10^{-27\,067}$. In Chapter 4, we estimate the dimension of an inertial manifold from the periodic orbits embedded in it, and verify that our results are consistent with earlier work based on averaging covariant vectors over ergodic trajectories. This calculation is the first of its kind on this subject that is not an ergodic average, but it actually pins down the geometry of inertial manifold's embedding in the state space. It opens a door to tiling inertial manifolds by invariant structures of system's dynamics.

1.2 Dissipative nonlinear systems

Dissipative nonlinear systems described by PDEs are infinite-dimensional in principle, but a lot of them exhibit finite dimensional behavior after a transient period of evolution. In this context, the concept of global attractor was introduced to describe the asymptotic behavior of a dissipative system. Different definitions of dimension have been proposed to characterize the dimensionality of a global attractor. The estimated dimension provides a sense of the size of the global attractor, but such numbers, usually not integers, are smaller than the number of degrees of freedom needed to determine the system. This is where the inertial manifold is introduced to account for the question that how many modes are needed to effectively describe a dissipative chaotic system.

1.2.1 Global attractor

Before we introduce a global attractor, let us define all necessary tools first. Here we follow expositions of Robinson [71] and Temam [81]. Let a dynamical system $u(t)$, $t \geq 0$ be defined in a state space $\mathcal{M}$. $\mathcal{M}$ is a Hilbert space, usually the L^2 space, with L^2 norm the appropriate norm for measuring distances between different states. f^t is a *semigroup* that evolves the system forward in time, $u(t) = f^t u_0$, with following properties:

$$
\begin{aligned}
&f^0 = 1\,,\\
&f^t f^s = f^{s+t}\,,\\
&f^t u_0 \text{ is continuous in } u_0 \text{ and } t\,.
\end{aligned}
$$

An absorbing set is a bounded set that attracts all orbits in this system. We define dissipative systems as follows.

Definition 1.1 *A semigroup is dissipative if it possesses a compact absorbing set B and for any bounded set X there exists a $t_0(X)$ such that*

$$f^t X \subset B \quad \textit{for all} \quad t \geq t_0(X)$$

Here, symbol $\subset$ means that the left side is a proper subset of, or equal to the right side. Therefore, in a dissipative system, all trajectories eventually enter and stay in an absorbing set. Moreover, we say that a set $X \subset \mathcal{M}$ is *invariant* if

$$f^t X = X \quad \text{for all} \quad t \geq 0 \tag{1}$$

and a set $X \subset \mathcal{M}$ is *positive-invariant* if

$$f^t X \subset X \quad \text{for all} \quad t \geq 0\,. \tag{2}$$

With the above setup, let us turn to the definition of a global attractor.

Definition 1.2 *The global attractor $\mathcal{A}$ is the maximal compact invariant set*

$$f^t \mathcal{A} = \mathcal{A} \quad \textit{for all} \quad t \geq 0 \tag{3}$$

and the minimal set that attracts all bounded sets:

$$\mathrm{dist}(f^t X, A) \to 0 \quad \textit{as} \quad t \to \infty \tag{4}$$

for any bounded set $X \subset \mathcal{M}$, where $\mathcal{M}$ is the state space.

Here, the distance between two sets is defined as

$$\mathrm{dist}(X, Y) = \sup_{x\in X} \inf_{y\in Y} |x - y| \,. \tag{5}$$

Requirement (3) says that a global attractor does not contain any transient trajectories, and any trajectory in the state space will approach the global attractor arbitrarily close according to (4). Note, the definition emphasizes that the attractor is "global/maximal" because it attracts any bounded sets in state space $\mathcal{M}$. If it only attracts some portion of $\mathcal{M}$, then it is an attractor but not a global one. On the other hand, the word "minimal" in the definition is a consequence of (4). Suppose there is a smaller compact set $\mathcal{B} \subsetneq \mathcal{A}$, then we take the bounded set $X = \mathcal{A}$ and get $\mathrm{dist}(f^t\mathcal{A}, \mathcal{B}) = \mathrm{dist}(\mathcal{A}, \mathcal{B})$ which cannot reach zero in a Hausdorff space. [1]

Now, we turn to the question that whether a global attractor exists for a dissipative system, and if it does, then what subsets in the state space should be included in it. We have some expectations in mind. First, the concept of global attractor was introduced to assist the study of the asymptotic behavior in a dissipative system, so we expect its existence in dissipative systems. Second, the global attractor should include all the important dynamical structures of a dissipative system, such as equilibria, periodic orbits, their unstable manifolds, homoclinic/heteroclinic orbits and so on. If a global attractor fails either of these two requirements, then it makes no sense to use it in practice. Both questions are answered by the following theorem.

Theorem 1.3 *If f^t is dissipative and $B \subset \mathcal{M}$ is a compact absorbing set then there exists a global attractor $\mathcal{A} = \omega(B)$.*

Here, $\omega(B)$ is the ω-limit set of B. For any subset $X \subset \mathcal{M}$, its ω-limit set is defined as

$$\omega(X) = \{y : \text{there exist sequences } t_n \to \infty \text{ and } u_n \in X \text{ with } f^{t_n}u_n \to y\} \,. \tag{6}$$

An equivalent limit supremum definition is

$$\omega(X) = \bigcap_{t\geq 0} \overline{\bigcup_{s\geq t} f^s X}$$

Here, the overbar of a set means taking the closure of this set. It is easy to see that the ω-limit set of a single point u consists of all limiting points of $f^{t_n}u$ given it converges for a sequence of $\{t_n\}_{n=1}^{\infty}$, $t_n \to \infty$, i.e.,

$$\omega(u) = \{y : \text{there exists a sequence } t_n \to \infty \text{ with } f^{t_n}u \to y\} \,. \tag{7}$$

Theorem 1.3 not only claims the existence of a global attractor in a dissipative system but also gives the explicit form of it as the ω-limit set of a bounded set. Now, let us check whether $\omega(B)$ contains all the important invariant structures in this system as expected. By definition (6) and (7), we can obtain the ω-limit set for a few invariant dynamical structures. For an equilibrium u: $f^t u = u$, so $\omega(u) = u$. For a periodic orbit p, $\omega(p) = p$, and for any $u \in p$, $\omega(u) = p$. These two simple examples may tempt you to think that $\cup_{u\in X}\omega(u) = \omega(X)$. However, this is not true. Actually, what we only know is that

$$\bigcup_{u\in X} \omega(u) \subset \omega(X) \,. \tag{8}$$

---

[1] A Hausdorff space is a topological space in which distinct points have disjoint neighborhoods. Therefore, distinct points have positive distance.

Usually, the left-side set in (8) is much smaller than the right-side set. To illustrate this point, Figure 1, taken from [71], depicts a planar system with 3 equilibria $\{a, b, c\}$. a and c are stable. b has a homoclinic orbit denoted as $W^u(b)$ [2] since it is also an unstable manifold of b. For any $u \in W^u(b)$, $\omega(u) = b$. However, for the whole orbit $\omega(W^u(b)) = W^u(b)$. An intuitive explanation goes as follows. For any $y \in W^u(b)$ and a $t_n > 0$, we can find a point u_n ahead of y on the homoclinic orbit $u_n \in W^u(b)$ such that $f^{t_n} u_n = y$. The larger t_n is, the closer u_n is to b. It takes an infinitely long time to go backward from y to b. So we find sequences $t_n \to \infty$ and $u_n \in W^u(b)$ such that $f^{t_n} x_n \to y$, and by definition, $y \in \omega(W^u(b))$. The same argument can be applied to the bounded stable manifold of c in Figure 1(a), $\omega(W^s(c)) = W^s(c)$.

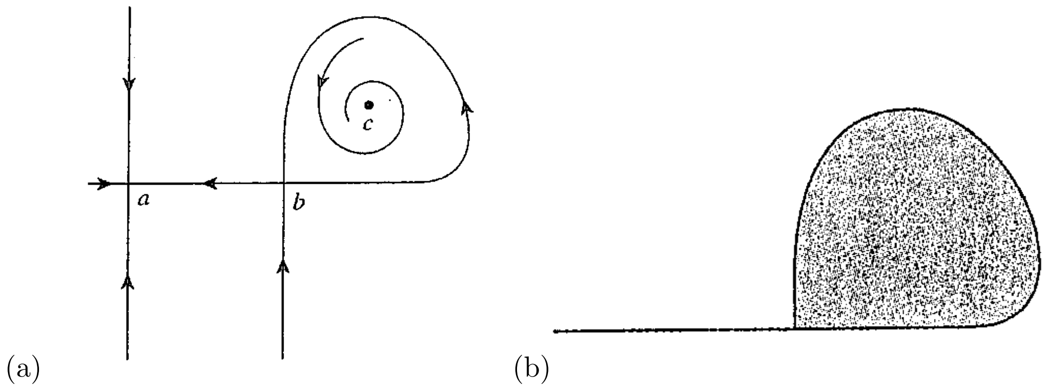

Figure 1: (a) State space portrait of a 2d system. (b) The corresponding global attractor.

The ω-limit sets of equilibria, periodic orbits, and homoclinic orbits are the objects themselves, so they all belong to the global attractor, as we would expect. Meanwhile, concerning the stable and unstable manifolds, we have the following theorem.

Theorem 1.4 *The unstable manifolds and bounded stable manifolds of a compact invariant set are contained in the global attractor.*

We stress that the global attractor does not contain unbounded stable/unstable manifolds. Unstable manifolds are intrinsically bounded in dissipative systems, so we omit the word "bounded" in front of it in theorem 1.4. The explanation is simple. Let $u(t)$ be a point in the unstable manifold of an invariant set X, i.e., $u(t) \in W^u(X)$, then $u(t)$ approaches X for $t \to -\infty$ by definition, and $u(t) \in B$ when $t \to \infty$ because the system is dissipative with B an absorbing set. Therefore, unstable manifold $W^u(X)$ is bounded. However, not all stable manifolds are bounded. For example, one-dimensional dissipative system $\dot{u} = -\lambda u$, $\lambda > 0$ has a global attractor $u = 0$, but its stable manifold extends to $u \to \pm\infty$. Such a distinction between stable and unstable manifolds in dissipative systems is crucial for us to understand the finite dimensionality of such systems. In an infinite-dimensional system described by a PDE, an unstable invariant structure usually has only a few unstable modes and the rest, infinite many, are all stable modes. Only a finite subset of these stable modes participates in the dynamics. As we shall show in this thesis, the rest stable modes are decoupled from other modes, decay exponentially, and do not belong to the global attractor.

---

[2] The stable and unstable manifolds of a subset $X \subset \mathcal{M}$ are denoted respectively as $W^s(X)$ and $W^u(X)$.

In the example shown in Figure 1(a), the 3 equilibria $\{a, b, c\}$, the stable manifold of c, the homoclinic orbit of b and the heteroclinic orbit from b to a compose the global attractor, which is shown in Figure 1(b).

The global attractor in the Lorenz system We now prove the existence of a global attractor for the Lorenz system to illustrate the concepts introduced in this section. Theorem 1.3 tells us that the key point of showing the existence of a global attractor is to find a compact absorbing set B in the system. For Lorenz system

$$\begin{aligned}\dot{x} &= -\sigma x + \sigma y \\ \dot{y} &= rx - y - xz \\ \dot{z} &= xy - bz\end{aligned}$$

with $\sigma, r, b > 0$, consider

$$V(x, y, z) = x^2 + y^2 + (z - r - \sigma)^2 .$$

Then,

$$\begin{aligned}\frac{dV}{dt} &= -2\sigma x^2 - 2y^2 - 2bz^2 + 2b(r+\sigma)z \\ &= -2\sigma x^2 - 2y^2 - b(z - r - \sigma)^2 - bz^2 + b(r+\sigma)^2 \\ &\leq -\alpha V + b(r+\sigma)^2\end{aligned}$$

Here $\alpha = \min(2\sigma, 2, b)$. By the Gronwall inequality, we obtain

$$V \leq \frac{2b(r+\sigma)^2}{\alpha} .$$

Lemma 1.5 *(Gronwall's Inequality) If*

$$\frac{du}{dt} \leq au + b ,$$

then

$$u(t) \leq (u_0 + \frac{b}{a})e^{at} - \frac{b}{a} .$$

Therefore, there is an absorbing sphere S with radius $(2b/\alpha)^{1/2}(r + \sigma)$ in Lorenz system. So a global attractor exists and it is given as $\omega(S)$.

1.2.2 The dimension of an attractor

Though the state space $\mathcal{M}$ may be infinite-dimensional, after a transient period of evolution, the dynamics is usually determined only by a finite number of degrees of freedom. The global attractor lives in a finite-dimensional subspace of the state space. Consequently, the study of the dimension of the global attractor is crucial for us to understand the longtime behavior of this system. According to ref. [31], the types of dimensions of chaotic attractors can be classified into three categories. One is *fractal dimensions*, based purely on the geometry of the attractor such as the box-counting dimension D_C and the Hausdorff dimension D_H. The second type incorporates the frequency with which a typical trajectory visits various parts of the attractor, namely the natural measure of the attractor, such as the information dimension D_I, correlation dimension D_μ [46], and so on. The third one, Kaplan-Yorke dimension D_{KY} is defined in terms of the dynamical properties of an attractor rather than the geometry or the natural measure. Kaplan and Yorke [38, 51] initially conjectured that $D_{KY} = D_C$, but later it was shown that D_{KY} is an upper bound of the information dimension. Some comparison of these various definitions of dimension can be found in refs. [31, 46, 49]. In this subsection, we list some representative definitions related to our research.

Box-counting dimension (capacity dimension, Kolmogorov dimension) By using a minimal set of balls with radius ϵ to cover the attractor and record the number of balls $N(\epsilon)$, the *box-counting dimension* is given by

$$D_C = \limsup_{\epsilon \to 0} \frac{\log N(\epsilon)}{\log(1/\epsilon)} \tag{9}$$

Note, we can also use cubes of side length ϵ, which does not change the result. Basically, D_C tells us how dense the state points are inside the attractor. Trivial cases, like $D_C = 1$ for a straight line and $D_C = 2$ for an area, are within our expectation, but for fractal objects, it usually produces fraction/irrational numbers. For instance, $D_C = \log 3/\log 2$ for the Sierpinski triangle shown in Figure 2.

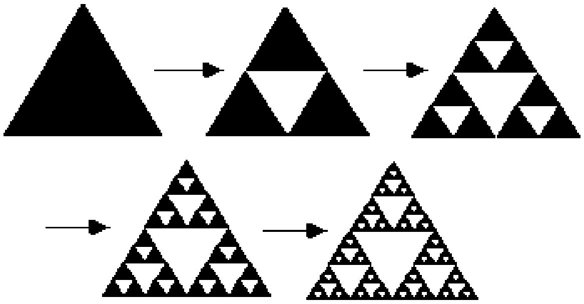

Figure 2: The iterative process to get the Sierpinski triangle (from ref. [23]).

Hausdorff dimension The box-counting dimension uses balls of the same radius ϵ to cover the attractor. Here, we try to cover the attractor with nonuniform open balls whose radius is no larger than ϵ. First, we define the d-dimensional Hausdorff measure of a set X in $\mathcal{M}$.

$$\mathcal{H}^d(X) = \liminf_{\epsilon \to 0} \left\{ \sum_{i=0}^{\infty} r_i^d : r_i < \epsilon \text{ and } X \subset \bigcup_{i=0}^{\infty} B_{r_i}(u_i) \right\} . \tag{10}$$

Here, $B_{r_i}(u_i)$ is a d-dimensional open ball centered at u_i with radius r_i. The definition is analogous to the definition of Lebesgue measure. The basic idea is to estimate the volume of the attractor by the total volume of finer and finer countable d-dimensional covering balls, where d is a parameter in this measure. If d is larger than the actual dimension of the attractor, then $\mathcal{H}^d(X) = 0$. For example, we need $1/2r$ circles whose radius is r to cover a unit one-dimensional segment. The total area of these circles goes to zero when $r \to 0$. On the other hand, if d is smaller than the actual dimension, then $\mathcal{H}^d(X) \to \infty$. For instance, we need infinitely long one-dimensional segments to cover a two-dimensional plane. Based on this observation, the *Hausdorff dimension* of a compact set X is defined as

$$D_H(X) = \inf\left\{d : \mathcal{H}^d(X) = 0 \text{ with } d > 0\right\} . \tag{11}$$

In general, the Hausdorff dimension is not easy to get for a dynamical system. But we do have an upper bound

$$D_H(X) \le D_C(X) . \tag{12}$$

This relation is easy to understand. In defining Hausdorff dimension we have more choices of the covering balls than that in box-counting dimension. Also, (10) is taking an infimum of all choices while D_C takes the supremum. For a rigorous proof of (12), see ref. [71].

Information dimension The fractal dimension does not count the frequency with which each small region is visited on the attractor. In order to incorporate such information, the number of covering balls $N(\epsilon)$ is replaced by the entropy function $-\sum^{N(\epsilon)} P_i \log P_i$, where P_i is the probability contained in cube c_i, namely the natural measure $\mu(c_i)$ of the attractor. The information dimension is then given as [31]

$$D_I = \lim_{\epsilon \to 0} \frac{-\sum_{i=1}^{N(\epsilon)} P_i \log P_i}{\log(1/\epsilon)} . \tag{13}$$

The information dimension is no larger than the box-counting dimension, and $D_I = D_C$ when the natural measure is constant across the attractor.

Kaplan-Yorke dimension (Lyapunov dimension) Kaplan and Yorke first proposed the idea of defining the dimension of a chaotic attractor by the Lyapunov exponents [3] in ref. [51], and later they elaborated their proposal it in ref. [38]. Here I sketch their basic idea [73].

Let $\lambda_1 \ge \cdots \ge \lambda_n$ are the Lyapunov spectrum of an n-dimensional chaotic system ($\lambda_1 > 0$). We try to determine how many cubes needed to cover the neighborhood of a template point $u(0)$ as the system evolves. Suppose the neighborhood is an n-dimensional parallelogram with initially each edge oriented in the covariant direction at $u(0)$, and the number of ϵ-cubes needed to cover this parallelogram is $N(\epsilon)$; then after an infinitesimal time δt, the neighborhood moves to $u(\delta t)$ and the parallelogram gets stretched/contracted in each covariant direction. Choose some $j+1$ such that $\lambda_{j+1} < 0$, we use a smaller cube with length $e^{\lambda_{j+1}\delta t}\epsilon$ to cover the new neighborhood, then

$$N(e^{\lambda_{j+1}\delta t}\epsilon) = \left(\prod_{i=1}^{j} e^{(\lambda_i - \lambda_{j+1})\delta t}\right) N(\epsilon) \tag{14}$$

Let's explain the coefficient above. The ith direction with $i < j+1$ has been stretched by a factor $e^{\lambda_i \delta t}$, and the new cube length is $e^{\lambda_{j+1}\delta t}\epsilon$, so it needs $e^{(\lambda_i - \lambda_{j+1})\delta t}$ times more cubes

---

[3] Actually, they used the magnitudes of multipliers or the 'Lyapunov numbers', defined as the exponentials of the Lyapunov exponents.

along this direction. Also, since choose $\lambda_{j+1} < 0$, then for the ith direction with $i > j+1$, the original number of cubes along this direction is enough to cover it, which means the above formula is actually over-counting in this direction. The exponential law $N(\epsilon) \propto \epsilon^{-d}$ from (9) is valid when ϵ is small enough. Then (14) reduces to $(e^{\lambda_{j+1}\delta t}\epsilon)^{-d} = \prod_{i=1}^{j} e^{(\lambda_i - \lambda_{j+1})\delta t}\epsilon^{-d}$ and thus

$$d(j) = j - \frac{\sum_{i=1}^{j}\lambda_i}{\lambda_{j+1}}\,. \tag{15}$$

Just as stated above, formula (15) is an upper bound of the dimension. We need to find the smallest $d(j)$ under condition $\lambda_{j+1} < 0$.

$$\begin{aligned} d(j+1) - d(j) &= 1 - \frac{\sum_{i=1}^{j+1}\lambda_i}{\lambda_{j+2}} + \frac{\sum_{i=1}^{j}\lambda_i}{\lambda_{j+1}} \\ &= \frac{(\lambda_{j+2} - \lambda_{j+1})(\lambda_1 + \cdots + \lambda_{j+1})}{\lambda_{j+2}\lambda_{j+1}} \end{aligned}$$

Let $\lambda_1 + \cdots + \lambda_k \geq 0$ and $\lambda_1 + \cdots + \lambda_{k+1} < 0$, then $d_{k+1} > d_k$ and $d_k < d_{k-1}$. Therefore

$$D_{KY} = k + \frac{\sum_{i=1}^{k}\lambda_i}{|\lambda_{k+1}|} \tag{16}$$

with k the largest number making $\lambda_1 + \cdots + \lambda_k$ non-negative.

Summary The definitions of dimension introduced in this section provide valuable information about the size of the global attractor. However, except for the Kaplan-Yorke dimension, all the other definitions try to cover the global attractor with cubes statically. The information about the topological structure of a global attractor has not been used. On the other hand, strange attractors are almost always fractal, and thus the dimension is an irrational number. With this number, we still do not know how many degrees of freedom are needed to effectively describe the dynamics of a dissipative PDE in an infinite-dimensional space. In the next section, we introduce the concept of the *inertial manifold* that contains the global attractor and determines the dynamics by a finite number of degrees of freedom.

1.2.3 Inertial manifold

For dissipative chaotic systems, asymptotic orbits are contained in a lower-dimensional subspace of the state space $\mathcal{M}$. Thus the effective dynamics can be described by a finite number of degrees of freedom. A global attractor usually has fractal dimension, which make it hard to analyze, so we need to construct a 'tight' smooth manifold that encloses it, and whose dimension gives the effective degrees of freedom of this system. This is called the *inertial manifold* [34, 70, 71, 81].

Here we use the concept of "*slaving*" in order to understand how the transition from infinite-dimensional space to finite-dimensional subspace happens. Let $u(t)$ be a dynamical system in an infinite-dimensional state space $\mathcal{M}$ governed by

$$\frac{du}{dt} + Au + F(u) = 0\,. \tag{17}$$

We split the "velocity" field into a linear part and a nonlinear part. Linear operator A is usually a negative Laplace operator or a higher-order spatial derivative. If the nonlinear term $F(u)$ is weak, then the dynamics is largely determined by the eigenspaces of A. That is why in practice solution $u(t)$ is usually expanded in terms of the eigenvectors of A. Specifically, if A is a negative Laplace operator, and the system is defined either on an infinite or periodic domain, then its eigenvectors are pure Fourier modes. $u(t)$ is determined by an infinite number of its Fourier coefficients. We say that high frequency modes are *slaved to* low frequency modes if there is a map that uniquely maps low frequency modes to high frequency modes. With such a map, the dynamics of the system is totally determined by the low frequency modes. To make this idea more precise, let P_n denote the projection from state space $\mathcal{M}$ to the subspace spanned by the eigenvectors of A corresponding to its smallest n eigenvalues, and let $Q_n = I - P_n$. Ranges of P_n and Q_n are denoted as $P_n\mathcal{M}$ and $Q_n\mathcal{M}$ respectively. Subspaces $P_n\mathcal{M}$ and $Q_n\mathcal{M}$ contain the low and high frequency modes of the solution $u(t)$. Though $Q_n\mathcal{M}$ is infinite-dimensional the effective dynamics is trapped in a finite-dimensional subspace of $\mathcal{M}$. So we anticipate that there is a map $\Phi : P_n\mathcal{M} \mapsto Q_n\mathcal{M}$ that determines the high frequency modes of $u(t)$ given its low frequency modes. Denote

$$p(t) = P_n u(t)\,, \quad q(t) = Q_n u(t) \tag{18}$$

and project (17) onto $P_n\mathcal{M}$, we obtain

$$\frac{dp}{dt} + Ap + P_n F(p + \Phi(p)) = 0\,. \tag{19}$$

So we have reduced the dynamics to a subspace given the existence of such a mapping Φ. Equation (19) is called the *inertial form* of this system. The graph of Φ

$$\mathcal{G}[\Phi] := \{u : u = p + \Phi(p)\,, p \in P_n\mathcal{M}\}$$

defines an n-dimensional manifold $\mathcal{I}$. This manifold is proved [71] to be an inertial manifold defined below.

Definition 1.6 *An inertial manifold $\mathcal{I}$ is a finite-dimensional Lipschitz manifold, which is positively invariant and attracts all trajectories exponentially,*

$$\mathrm{dist}(f^t u_0, \mathcal{I}) \leq C(|u_0|)e^{-kt} \quad \textit{for some } k > 0 \textit{ and all } u_0 \in \mathcal{M}\,. \tag{20}$$

Lipschitz means $|\Phi(p_1) - \Phi(p_2)| \leq L|p_1 - p_2|$ for any $p_1, p_2 \in P_n\mathcal{M}$ and some positive constant L. The Lipschitz condition is required for the initial form (19) to have unique solutions. There are several differences between a global attractor and an inertial manifold. First, an inertial manifold, by definition, has an integer number of dimensions, but a global attractor of a chaotic system usually has a fractal dimension. Second, an inertial manifold is only positive-invariant (2), but a global attractor is the maximal invariant subset of $\mathcal{M}$. Therefore, the global attractor is contained in the inertial manifold. Third, a global attractor can attract trajectories arbitrarily slowly by definition (4), while an inertial manifold attracts trajectories exponentially fast.

Equation (20) also implies that the error introduced by approximating $q(t)$ by $\Phi(p(t)$ decays exponentially with time:

$$|q(t) - \Phi(p(t))| \leq C(|u_0|)e^{-kt}\,. \tag{21}$$

The reason is as follows. From the definition of distance of two sets (5) and the fact that $u(t) = f^t u_0 = P_n u + Q_n u$, we have

$$\mathrm{dist}(f^t u_0, \mathcal{I}) = \inf_{s \in P_n\mathcal{M}} |(P_n u + Q_n u) - (s + \Phi(s))|\,.$$

Since projection P_n and Q_n are orthogonal to each other, the above infimum is reached when $s = P_n u$. Thus we have we

$$\mathrm{dist}(f^t u_0, \mathcal{I}) = |Q_n u - \Phi(P_n u))| = |q(t) - \Phi(p(t))| \ .$$

The equivalence between (20) and (21) confirms that the idea of *mode slaving* works in a dissipative system given the existence of an inertial manifold. For any point in the state space, we can find an approximate state on the inertial manifold. These two states share the same low frequency modes and only differ in their high frequency modes. High frequency modes are slaved to low frequency modes, and their difference decays exponentially. So after a short transient period, all orbits are effectively captured by the inertial manifold.

An inertial manifold exists in systems which possess the *strong squeezing property* [71]. A system says to have the strong squeezing property if for any two solutions $u(t) = p(t)+q(t)$ and $\bar{u}(t) = \bar{p}(t) + \bar{q}(t)$, the following two properties hold. (i) the *cone invariance property*: if

$$|q(0) - \bar{q}(0)| \le |p(0) - \bar{p}(0)| \tag{22}$$

then

$$|q(t) - \bar{q}(t)| \le |p(t) - \bar{p}(t)| \tag{23}$$

for all $t \le 0$, and (ii) the *decay property*: if

$$|q(t) - \bar{q}(t)| \ge |p(t) - \bar{p}(t)| \tag{24}$$

then

$$|q(t) - \bar{q}(t)| \le |q(0) - \bar{q}(0)|e^{-kt} \tag{25}$$

for some $k > 0$. The first property says that initially if two states satisfy the Lipschitz condition with Lipschitz constant 1, then such a Lipschitz condition holds at any later time. The second property accounts for the exponential attraction (20) of the inertial manifold. In practice, it is hard to verify the strong squeezing property directly. Here we provide an intuitive argument to show that a large gap in the eigenspectrum of operator A in (17) leads to the strong squeezing property. Let A have eigenvalues $\lambda_1 \le \lambda_2 \le \cdots$. Inertial form (19) describes the dynamics of the n low frequency modes which correspond to eigenvalues $\lambda_1, \cdots, \lambda_n$. The minimal growth rate in subspace $P_n\mathcal{M}$ is $-\lambda_n$. While, the rest high frequency modes should have approximately the largest growing rate $-\lambda_{n+1}$. If $-\lambda_{n+1}$ is far smaller than $-\lambda_n$, then we anticipate that $|p(t) - \bar{p}(t)|$ should grow faster than $|q(t) - \bar{q}(t)|$, so (23) holds. Also, if $-\lambda_{n+1} < 0$, then (25) should hold too. Note that we have not taken into consideration the coupling between low and high frequency modes by the nonlinear term $F(u)$ in (17). Therefore, to ensure strong squeezing property, the threshold of gap $\lambda_{n+1} - \lambda_n$ should depend on $F(u)$. Such a *spectral gap condition* is precisely described in the following theorem.

Theorem 1.7 *If $F(u)$ is Lipschitz*

$$|F(u) - F(v)| \le C_1 |u - v|, \quad u, v \in \mathcal{M}$$

and eigenvalues of A in (17) satisfies

$$\lambda_{n+1} - \lambda_n > 4C_1 \tag{26}$$

for some integer n, then the strong squeezing property holds, with k in (25) satisfying $k \ge \lambda_n + 2C_1$.

See [71] for the proof of this theorem.

The existence of an inertial manifold has been proved for many chaotic or turbulent systems such as Kuramoto-Sivashinsky equation, complex Ginzburg-Landau equation and the two-dimensional Navier-Stokes equations [81]. Also, numerical methods such as Euler-Galerkin [36] and nonlinear Galerkin method [61] have been proposed to approximate inertial manifolds. Approximating mapping $\Phi : P_n\mathcal{M} \mapsto Q_n\mathcal{M}$ requires choosing an appropriate n first. If n is smaller than the dimension of the inertial manifold, then Φ fails to describe the inertial manifold. However, if n is far larger than the dimension of the inertial manifold, then simulations on such approximations to the inertial manifold are not numerically efficient. At present, one uses empirical or some test number to truncate the original system. For example, in [36], 3 modes are used to represent the inertial manifold of the one-dimensional Kuramoto-Sivashinsky equation, but this truncated model is not sufficient to preserve the bifurcation diagram. At the same time, mathematical upper bounds for the dimension are not always tight. Therefore, little is known about the exact dimension of inertial manifolds in dissipative chaotic systems.

1.3 Covariant vectors

The recent progress in numerical methods to calculate *covariant vector*s [42, 54] has motivated us to explore an inertial manifold by covariant vectors locally through a statistical study of the tangency among covariant vectors [90] and difference vector projection [89]. The number of the covariant vectors needed for locally spanning the inertial manifold is regarded as the dimension of an inertial manifold. The key observation in this study is that tangent space can be decomposed into an entangled "physical" subspace and its complement, a contracting disentangled subspace. The latter plays no role in the longtime behavior on the inertial manifold.

In this section, we will introduce covariant vectors (often called "covariant Lyapunov vectors" in the literature [41, 42]) associated with periodic orbits and ergodic orbits. The general setup is that we have an autonomous continuous flow described by

$$\dot{u} = v(u)\,, \quad u(x,t) \in \mathbb{R}^n\,. \tag{27}$$

The corresponding time-forward trajectory starting from u_0 is $u(t) = f^t(u_0)$. In the linear approximation, the equation that governs the deformation of an infinitesimal neighborhood of $u(t)$ (dynamics in tangent space) is

$$\frac{d}{dt}\delta u = A\delta u\,, \quad A = \frac{\partial v}{\partial u}\,. \tag{28}$$

Matrix A is called the stability matrix of the flow. It describes the rates of instantaneous expansion/contraction and shearing in the tangent space. The Jacobian matrix of the flow transports linear perturbation along the orbit:

$$\delta u(u,t) = J^t(u_0, 0)\,\delta u(u_0, 0) \tag{29}$$

Here we make it explicit that the infinitesimal deformation δu depends on both the orbit and time. The Jacobian matrix is obtained by integrating equation

$$\frac{d}{dt}J = AJ\,, \quad J_0 = I\,. \tag{30}$$

Jacobian matrix satisfies the semi-group multiplicative property (chain rule) along an orbit,

$$J^{t-t_0}(u(t_0), t_0) = J^{t-t_1}(u(t_1), t_1)J^{t_1-t_0}(u(t_0), t_0)\,. \tag{31}$$

1.3.1 Floquet vectors

For a point $u(t)$ on a periodic orbit p of period T_p,

$$J_p = J^{T_p}(u,t) \tag{32}$$

is called the Floquet matrix (monodromy matrix), and its eigenvalues the Floquet multipliers Λ_j. The jth Floquet multiplier is a dimensionless ratio of the final/initial deformation along the jth eigendirection. It is an intrinsic, local property of a smooth flow, invariant under all smooth coordinate transformations. The associated Floquet vectors $\mathbf{e}_j(u)$,

$$J_p\,\mathbf{e}_j = \Lambda_j \mathbf{e}_j \tag{33}$$

define the invariant directions of the tangent space at periodic point $u(t) \in p$. Evolving a small initial perturbation aligned with an expanding Floquet direction will generate the corresponding unstable manifold along the periodic orbit. Written in exponential form

$$\Lambda_j = \exp(T_p \lambda_p^{(j)}) \;= \exp(T_p \mu^{(j)} + i\theta_j)\,,$$

where $\lambda_p^{(j)}$[4] are the Floquet exponents. Floquet multipliers are either real, $\theta_j = 0, \pi$, or form complex pairs, $\{\Lambda_j, \Lambda_{j+1}\} = \{|\Lambda_j|\exp(i\theta_j), |\Lambda_j|\exp(-i\theta_j)\}$, $0 < \theta_j < \pi$. The real parts of the Floquet exponents

$$\mu^{(j)} = (\ln|\Lambda_j|)/T_p \tag{34}$$

describe the mean contraction or expansion rates per one period of the orbit. Appendix A talks about the form of the Jacobian matrix of a general linear flow with periodic coefficients.

1.3.2 Covariant vectors

For a periodic orbit, the Jacobian matrix of n periods is the nth power of the Jacobian corresponding to a single period. However, for an ergodic orbit, there is no such simple relation. Integrating Jacobian matrix by (30) cannot be avoided for studying asymptotic stability of this orbit. However, similar to Floquet vectors of a periodic orbit, a set of covariant vectors exists for an ergodic orbit. *Multiplicative ergodic theorem* [66, 72] says that the forward and backward Oseledets matrices

$$\Xi^{\pm}(u) := \lim_{t\to\pm\infty} [J^t(u)^{\top} J^t(u)]^{1/2t} \tag{35}$$

both exist for an invertible dynamical system equipped with an invariant measure. Their eigenvalues are $e^{\lambda_1^+(u)} < \cdots < e^{\lambda_s^+(u)}$, and $e^{\lambda_1^-(u)} > \cdots > e^{\lambda_s^-(u)}$ respectively, with $\lambda_i^{\pm}(u)$ the Lyapunov exponents (characteristic exponents) and s the total number of distinct exponents ($s \le n$). For an ergodic system, Lyapunov exponents are the same almost everywhere, and

$$\lambda_i^+(u) = -\lambda_i^-(u) = \lambda_i \tag{36}$$

The corresponding eigenspaces $U_1^{\pm}(u), \cdots, U_s^{\pm}(u)$ can be used to construct the forward and backward invariant subspaces:

$$\begin{aligned} V_i^+(u) &= U_1^+(u) \oplus \cdots \oplus U_i^+(u) \\ V_i^-(u) &= U_i^-(u) \oplus \cdots \oplus U_s^-(u)\,. \end{aligned}$$

---

[4] Here, subscript p emphasizes that it is associated with a periodic orbit so as to distinguish it with the Lyapunov exponents defined in the next section.

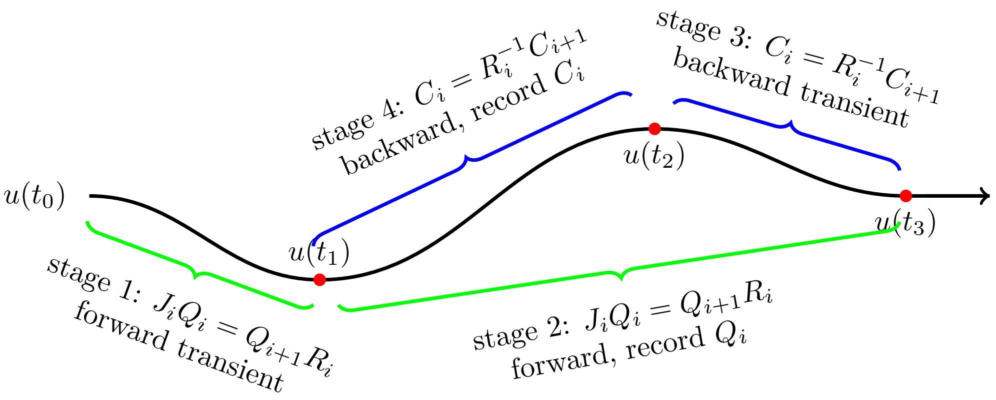

Figure 3: Four stages of covariant vector algorithm. The black line is a part of a long ergodic trajectory.

So the intersections

$$W_i(u) = V_i^+(u) \cap V_i^-(u) \tag{37}$$

are dynamically forward and backward invariant: $J^{\pm t}(u) W_i(u) \to W_i(f^{\pm t}(u))$, $i = 1, 2, \cdots, s$. (37) is called the Oseledets splitting. The expansion rate in the invariant subspace $W_i(u)$ is given by the corresponding Lyapunov exponent,

$$\lim_{t\to\pm\infty} \frac{1}{|t|} \ln \left\| \, J^t(u) v \, \right\| = \lim_{t\to\pm\infty} \frac{1}{|t|} \ln \left\| \, [J^t(u)^\top J^t(u)]^{1/2} v \, \right\| = \pm\lambda_i \,, \quad v \in W_i(u) \,. \tag{38}$$

If a Lyapunov exponent is nondegenerate, the corresponding subspace $W_i(u)$ reduces to a vector, called *covariant vector*. For periodic orbits, these λ_i (evaluated numerically as $t \to \infty$ limits of many repeats of the prime period T) coincide with the real parts of Floquet exponents (34). Subspace $W_i(u)$ coincides with a Floquet vector, or, if there is degeneracy, a subspace spanned by Floquet vectors.

The reorthonormalization procedure formulated by Benettin *et al.* [5] is the standard way to calculate the full spectrum of Lyapunov exponents, and it is shown [29] that the orthogonal vectors produced at the end of this procedure converge to $U_i^-(u)$, eigenvectors of $\Xi^-(u)$, called the Gram-Schmidt (GS) vectors (or backward Lyapunov vectors). Based on this technique, Wolf *et al.* [87] and Ginelli *et al.* [41, 42] independently invented distinct methods to recover covariant vectors from GS vectors. Here, we should emphasize that GS vectors are not invariant. Except for the leading one, all of them depend on the specific inner product imposed by the dynamics. Also, the local expansion rates of covariant vectors are not identical to the local expansion rates of GS vectors. Specifically for periodic orbits, Floquet vectors depend on no norm and map forward and backward as $\mathbf{e}_j \to J\,\mathbf{e}_j$ under time evolution. In contrast, the linearized dynamics does not transport GS vectors into the tangent space computed further downstream. For a detailed comparison, please see [54, 88].

1.3.3 Covariant vectors algorithm

Here we briefly introduce the method used by Ginelli *et al.* [41, 42] to extract covariant vectors from GS vectors. The setup is the same as computing Lyapunov exponents. We follow a long ergodic trajectory and integrate the linearized dynamics in tangent space (30) with orthonormalization regularly, shown as the first two stages in Figure 3. Here, J_i is the short-time Jacobian matrix, and $Q_{i+1}R_i$ is the QR decomposition of J_iQ_i. We use the new generated orthonormal matrix Q_{i+1} as the initial condition for the next short-time integration of (30). Therefore, if we choose an appropriate time length of each integration segment, we can effectively avoid numerical instability by repeated QR decomposition. Set the initial deformation matrix $Q_0 = I$, then after n steps in stage 1, we obtain

$$J_{n-1} \cdots J_0 = Q_n R_n \cdots R_0 \,.$$

The diagonal elements of upper-triangular matrices R_i store local Lyapunov exponents, longtime average of which gives the Lyapunov exponents of this system. In stage 1, we discard all these upper-triangular matrices R_i. We assume that Q_i converges to the GS vectors after stage 1, and start to record R_i in stage 2. Since the first m GS vectors span the same subspace as the first m covariant vectors, which means

$$T_i = Q_i C_i \,. \tag{39}$$

Here $T_i = [W_1, W_2, \cdots, W_n]$ refers to the matrix whose columns are covariant vectors at step i of this algorithm. C_i is an upper-triangular matrix, giving the expansion coefficients of covariant vectors in the GS basis. Since $J_{i-1}Q_{i-1} = Q_iR_i$, we have $T_i = J_{i-1}Q_{i-1}R_i^{-1}C_i$. Also since $T_{i-1} = Q_{i-1}C_{i-1}$, we get

$$T_i = J_{i-1}T_{i-1}C_{i-1}^{-1}R_i^{-1}C_i \tag{40}$$

Since T_i is invariant in the tangent space, namely, $J_{i-1}T_{i-1} = T_iD_i$ with D_i a diagonal matrix concerning the stretching and contraction of covariant vectors. Substitute it into (40), we get $I = D_iC_{i-1}^{-1}R_i^{-1}C_i$. Therefore, we obtain the backward dynamics of matrix C_i :

$$C_{i-1} = R_i^{-1}C_iD_i \tag{41}$$

Numerically, D_i is not formed explicitly since it is only a normalization factor. Ginelli *et al.* [41, 42] cleverly uncover this backward dynamics and show that C_i converges after a sufficient number of iterations (stage 3 in Figure 3). We choose an arbitrary upper-triangular matrix as the initial input for the backward iteration (41), R_i are those upper-triangular matrices recorded during stage 2, and R_i^{-1} are also upper-triangular. The product of two upper-triangular matrices is still upper-triangular. Thus, backward iteration (41) guarantees that C_i are all upper-triangular. This process is continued in stage 4 in Figure 3, and C_i are recorded at this stage. For trajectory segment $u(t_1)$ to $u(t_2)$ in Figure 3, we have the converged GS basis Q_i and the converged C_i, then by (39), we obtain the covariant vectors corresponding to this segment.

Covariant vector algorithm is invented to stratify the tangent spaces along an ergodic trajectory, so it is hard to observe degeneracy numerically. However, for periodic orbits, it is possible that some Floquet vectors form conjugate complex pairs. When this algorithm is applied to periodic orbits, it is reduced to a combination of simultaneous iteration and inverse power iteration; consequently, complex conjugate pairs cannot be told apart. This means that we need to pay attention to the two-dimensional rotation when checking the convergence of each stage in Figure 3. As is shown in Chapter 5, a complex conjugate pair of Floquet vectors can be extracted from a converged two-dimensional subspace.

$$
\begin{aligned}
&\begin{bmatrix} x&x&x&x&x&x\\ x&x&x&x&x&x\\ x&x&x&x&x&x\\ x&x&x&x&x&x\\ x&x&x&x&x&x\\ x&x&x&x&x&x \end{bmatrix}
\begin{bmatrix} x&x&x&x&x&x\\ x&x&x&x&x&x\\ x&x&x&x&x&x\\ x&x&x&x&x&x\\ x&x&x&x&x&x\\ x&x&x&x&x&x \end{bmatrix}
\begin{bmatrix} x&x&x&x&x&x\\ x&x&x&x&x&x\\ x&x&x&x&x&x\\ x&x&x&x&x&x\\ x&x&x&x&x&x\\ x&x&x&x&x&x \end{bmatrix}
\xrightarrow{\text{stage 1}}
\begin{bmatrix} x&x&x&x&x&x\\ x&x&x&x&x&x\\ &x&x&x&x&x\\ &&x&x&x&x\\ &&&x&x&x\\ &&&&x&x \end{bmatrix}
\begin{bmatrix} x&x&x&x&x&x\\ &x&x&x&x&x\\ &&x&x&x&x\\ &&&x&x&x\\ &&&&x&x\\ &&&&&x \end{bmatrix}
\begin{bmatrix} x&x&x&x&x&x\\ &x&x&x&x&x\\ &&x&x&x&x\\ &&&x&x&x\\ &&&&x&x\\ &&&&&x \end{bmatrix}\\
&\xrightarrow{\text{stage 2}}
\begin{bmatrix} x&x&x&x&x&x\\ &x&x&x&x&x\\ &x&x&x&x&x\\ &&&x&x&x\\ &&&&x&x\\ &&&&&x \end{bmatrix}
\begin{bmatrix} x&x&x&x&x&x\\ &x&x&x&x&x\\ &&x&x&x&x\\ &&&x&x&x\\ &&&&x&x\\ &&&&&x \end{bmatrix}
\begin{bmatrix} x&x&x&x&x&x\\ &x&x&x&x&x\\ &&x&x&x&x\\ &&&x&x&x\\ &&&&x&x\\ &&&&&x \end{bmatrix}
\end{aligned}
$$

Figure 4: Two stages of periodic Schur decomposition algorithm illustrated by three [6×6] matrices. Empty locations are zeros.

1.3.4 Periodic Schur decomposition algorithm

Here, we review another algorithm related to our work. The double-implicit-shift QR algorithm [84, 85] is the standard way of solving the eigen-problem of a single matrix in many numerical packages, such as the `eig()` function in Matlab. Bojanczyk *et al.* [8] extend this idea to obtain *periodic Schur decomposition* of the product of a sequence of matrices. Later on, Kurt Lust [60] describes the implementation details and provides the corresponding Fortran code. On the other hand, by use of the chain rule (31), the Jacobian matrix can be decomposed into a product of short-time Jacobians with the same dimension. Therefore, periodic Schur decomposition is well suited for computing Floquet exponents.

As illustrated in Figure 4, periodic Schur decomposition proceeds in two stages. First, the sequence of matrices is transformed to the *Hessenberg-Triangular* form, one of which has upper-Hessenberg form while the others are upper-triangular, by a series of Householder transformations [84]. The second stage tries to diminish the sub-diagonal components of the Hessenberg matrix until it becomes quasi-upper-triangular, that is, there are some [2×2] blocks on the diagonal corresponding to complex eigenvalues. The eigenvalues of the matrix product are given by the products of all individual matrices' diagonal elements. However, periodic Schur decomposition is not sufficient for extracting eigenvectors, except the leading one. Kurt Lust [60] claims to formulate the corresponding Floquet vector algorithm, but to the best of our knowledge, such an algorithm is not present in the literature. Fortunately, Granat *et al.* [44] have proposed a method to reorder diagonal elements after periodic Schur decomposition. This provides an elegant way to compute Floquet vectors as we will see in Chapter 5.

1.4 Dynamics averaged over periodic orbits

Statistical properties and the geometrical structure of the global attractor are among the major questions in the study of chaotic nonlinear dissipative systems. Generally, such a system will get trapped to the global attractor after a transient period, and we are only interested in the dynamics on the attractor. The intrinsic instability of orbits on the attractor make the longtime simulation unreliable, which is also time-consuming. Fortunately, ergodic theorem [78] indicates that longtime average converges to the same answer as a spatial average over the attractor, provided that a natural measure exists on the attractor.

$$\overline{\langle a \rangle} = \lim_{t\to\infty} \frac{1}{|\mathcal{M}|}\int_{\mathcal{M}} du_0 \, \frac{1}{t}\int_0^t d\tau \, a(u(\tau)) \tag{42}$$

$$= \frac{1}{|\mathcal{M}_\rho|}\int_{\mathcal{M}} du \, \rho(u)\, a(u)\,. \tag{43}$$

Here, $a(u(t))$ is an observation, namely, a temporal physical quantity such as average diffusion rate, energy dissipation rate, Lyapunov exponents and so on. $\overline{\langle a \rangle}$ refers to its spatiotemporal average on the attractor. $u(t)$ defines a dynamical system described by (27). $\mathcal{M}$ is the state space of this system. $\rho(u)$ is the natural measure. Normalization quantities are

$$|\mathcal{M}| = \int_{\mathcal{M}} du \ , \quad |\mathcal{M}_\rho| = \int_{\mathcal{M}} du \, \rho(u) \tag{44}$$

We make a distinction between the notation for spatiotemporal average $\overline{\langle a \rangle}$ and that for spatial average

$$\langle a \rangle = \frac{1}{|\mathcal{M}|}\int_{\mathcal{M}} du \ a(u)\,.$$

So if we define the integrated observable

$$A^t(u_0) = \int_0^t d\tau \, a(u(\tau))\,, \tag{45}$$

then

$$\overline{\langle a \rangle} = \lim_{t\to\infty}\frac{1}{t}\langle A^t\rangle = \lim_{t\to\infty}\frac{1}{t}\frac{1}{|\mathcal{M}|}\int_{\mathcal{M}} du_0 \, A^t(u_0)\,. \tag{46}$$

Formula (43) provides a nice way to calculate spatiotemporal average while avoiding long-time integration. However, as a strange attractor usually has a fractal structure and the natural measure $\rho(u)$ could be arbitrarily complicated and non-smooth, computation by (43) is not numerically feasible. This is where the *cycle averaging theory* [22] enters. In this section, we illustrate the process of obtaining the spatiotemporal average (42) by the weighted contributions from a set of periodic orbits.

1.4.1 The evolution operator

Towards the goal of calculating spatiotemporal averages, it does not suffice to follow a single orbit. Instead, we study a swarm of orbits and see how they evolve as a whole. Equation (46) deploys this idea exactly. We take all points in the state space and evolve them for a certain time, after which we study their overall asymptotic behavior. By formula (46), the spatiotemporal average of observable $a(u(t))$ is given by the asymptotic behavior of the corresponding integrated observable $A^t(u)$. However, instead of calculating $\langle A^t\rangle$, we turn to

$$\langle e^{\beta A^t}\rangle = \frac{1}{|\mathcal{M}|}\int_{\mathcal{M}} du_s \, e^{\beta A^t(u_s)}\,. \tag{47}$$

Here we use u_s instead of u_0 as in (46) to denote the starting point of the trajectory. β is an auxiliary variable. The motivation of studying $e^{\beta A^t}$ instead of A^t will be manifest later. Actually, this form resembles the partition function in statistical mechanics where

$\beta = -1/kT$. And we will find several analogous formulas in this section with those in the canonical ensemble. Equation (47) can be transformed as follows.

$$\langle e^{\beta A^t} \rangle = \frac{1}{|\mathcal{M}|} \int_{\mathcal{M}} du_s \, \left(\int_{\mathcal{M}} du_e \, \delta\big(u_e - f^t(u_s)\big) \right) e^{\beta A^t(u_s)} \tag{48}$$

$$= \frac{1}{|\mathcal{M}|} \int_{\mathcal{M}} du_e \int_{\mathcal{M}} du_s \, \delta\big(u_e - f^t(u_s)\big) \, e^{\beta A^t(u_s)} \tag{49}$$

$$= \frac{1}{|\mathcal{M}|} \sum_{\substack{\text{all trajectories} \\ \text{of length } t}} e^{\beta A^t(u_s)} \, . \tag{50}$$

From (47) to (48), we insert an identity in the integral, and from (48) to (49), we change the integral order. Here, u_s and u_e denote respectively the starting state and end state of a trajectory. Basically, (50) says that whenever there is a path from u_s to u_e, we should count its contribution to the spatiotemporal average. This idea is inspired by the path integral in quantum mechanics. Feynman interprets the *propagator* (transition probability) $\langle \psi(x', t') | \psi(x, t) \rangle$ as a summation over all possible paths connecting the starting and end states, where the classical path is picked out when $i/\hbar \to \infty$. Here, in (49) we are on a better standing because the Dirac delta function picks out paths that obey the flow equation exactly. Actually, the transition from a procedural law (42) to a high-level principle (50) is a tendency in physics, similar to the transition from Lagrangian mechanics to the principle of least action, or the transition from Schrödinger equation to the path integral.

The kernel of the integral in (49) is called the *evolution operator*

$$\mathcal{L}^t(u_e, u_s) \; = \; \delta\big(u_e - f^t(u_s)\big) \; e^{\beta A^t(u_s)} \, . \tag{51}$$

The evolution operator shares a lot of similarities with the propagator in quantum mechanics. For example, the evolution operator also forms a semigroup:

$$\mathcal{L}^{t_1 + t_2}(u_e, u_s) \; = \; \int_{\mathcal{M}} du' \, \mathcal{L}^{t_2}(u_e, u') \mathcal{L}^{t_1}(u', u_s) \tag{52}$$

We define the action of the evolution operator on a function as

$$\mathcal{L}^t \circ \phi \; = \; \int_{\mathcal{M}} du_s \, \mathcal{L}^t(u_e, u_s) \phi(u_s) \tag{53}$$

which is a function of the end state u_e. A function $\phi(u)$ is said to be the eigenfunction of $\mathcal{L}^t$ if $\mathcal{L}^t \circ \phi = \lambda(t) \, \phi$. Here $\lambda(t)$ is the eigenvalue. We make it explicit that it depends on time. Note, $\mathcal{L}^t$ acts on a function space, so in principle, $\mathcal{L}^t$ is an infinite-dimensional operator. However, in some cases such as piece-wise maps, if the observable is defined uniformly in each piece of the domain, then $\mathcal{L}^t$ can effectively be expressed as a finite-dimensional matrix. Here we give two examples of the eigenfunctions of $\mathcal{L}^t$.

Example 1.1 The invariant measure of an equilibrium is an eigenfunction of $\mathcal{L}^t$ *The invariant measure of an equilibrium u_q is given by*

$$\phi(u) = \delta(u - u_q) \, .$$

Then

$$\begin{aligned}
\mathcal{L}^t \circ \phi &= \int_{\mathcal{M}} du_s \, \mathcal{L}^t(u_e, u_s)\delta(u_s - u_q) \\
&= \int_{\mathcal{M}} du_s \, \delta\big(u_e - f^t(u_s)\big) \; e^{\beta A^t(u_s)}\delta(u_s - u_q) \\
&= \delta\big(u_e - f^t(u_q)\big) \; e^{\beta A^t(u_q)} \\
&= \delta(u_e - u_q) \; e^{t\beta a(u_q)} \\
&= e^{t\beta a(u_q)}\phi(u_e) \, .
\end{aligned}$$

Therefore, the invariant measure of an equilibrium is an eigenfunction of the evolution operator with eigenvalue $e^{t\beta a(u_q)}$*.*

Example 1.2 The invariant measure of a periodic orbit is an eigenfunction of $\mathcal{L}^{nT}$ *The invariant measure of a periodic orbit is given by*

$$\phi(u) = \frac{1}{T}\int_0^T \delta(u - f^t(u_0)dt \, . \tag{54}$$

Here, T *is the period of this orbit.* u_0 *is an arbitrarily chosen point on this orbit. Then*

$$\begin{aligned}
\mathcal{L}^{nT} \circ \phi &= \frac{1}{T}\int_0^T \int_{\mathcal{M}} du_s \, \delta\big(u_e - f^{nT}(u_s)\big) \; e^{\beta A^{nT}(u_s)}\delta(u_s - f^{nT}(u_0)dt \\
&= \frac{1}{T}\int_0^T \int_{\mathcal{M}} du_s \, \delta\big(u_e - f^{nT+t}(u_s)\big) \; e^{\beta A^{nT}(f^t(u_0)}\delta(u_s - f^t(u_0)dt \\
&= \frac{1}{T}\int_0^T \delta\big(u_e - f^t(u_0)\big) \, e^{n\beta A^T(u_0)}dt \int_{\mathcal{M}} du_s \, \delta(u_s - f^t(u_0) \\
&= \frac{1}{T}\int_0^T \delta\big(u_e - f^t(u_0)\big) \; e^{n\beta A^T(u_0)}dt \\
&= e^{n\beta A^T(u_0)}\phi(u_e) \, .
\end{aligned}$$

In the above derivation, we have used the identity $A^{nT}(f^t(u_0) = nA^T(u_0)$ *which is manifest because* u_0 *is a periodic point. In general, (54) is not an eigenfunction of* $\mathcal{L}^t$*, but it is for* $t = nT$*. In the above formula,* $A^T(u_0)$ *actually does not depend on the choice of the starting point* u_0 *as long as it is one point on the periodic orbit.*

Let us now turn to the original problem of how to calculate (46) and why we choose the exponential form in (47). Combine (46), (47) and (49), we have

$$\overline{\langle a \rangle} = \lim_{t\to\infty} \frac{1}{t} \frac{\partial}{\partial\beta} \langle e^{\beta A^t} \rangle \Big|_{\beta=0} \tag{55}$$

$$= \frac{\partial}{\partial\beta} \lim_{t\to\infty} \frac{1}{t} \frac{1}{|\mathcal{M}|} \int_{\mathcal{M}} du_e \int_{\mathcal{M}} du_s \, \mathcal{L}^t(u_e, u_s) \Big|_{\beta=0} \, . \tag{56}$$

Here, we have used a trick to obtain the spatial average by using an auxiliary variable β, which is similar to what we do in the canonical ensemble. $\overline{\langle a \rangle}$ is given by the longtime average of the evolution operator. From example 1.1 and 1.2, we see that the eigenvalues of $\mathcal{L}^t$ go to ∞ when $t \to \infty$. Therefore, asymptotically, the leading eigenvalue of $\mathcal{L}^t$ will dominate the spatiotemporal average in (56). By the semi-Lie group property (52), we define $\mathcal{L}^t = e^{t\mathcal{A}}$ with $\mathcal{A}$ defined as the generator of the evolution operator. Then (56) is simplified as follows,

$$\overline{\langle a \rangle} = \lim_{t\to\infty} \frac{1}{|\mathcal{M}|} \int_{\mathcal{M}} du_e \int_{\mathcal{M}} du_s \, \mathcal{L}^t(u_e, u_s) \frac{\partial}{\partial \beta} \mathcal{A} \Big|_{\beta=0} \tag{57}$$

$$= \lim_{t\to\infty} \frac{1}{|\mathcal{M}|} \int_{\mathcal{M}} du_e \int_{\mathcal{M}} du_s \, \delta\big(u_e - f^t(u_s)\big) \frac{\partial}{\partial \beta} \mathcal{A} \Big|_{\beta=0} \tag{58}$$

$$= \lim_{t\to\infty} \langle \frac{\partial}{\partial \beta} \mathcal{A} \rangle \Big|_{\beta=0} \,. \tag{59}$$

As we said, the time limit above will converge to the leading eigenvalue of $\mathcal{A}$. By letting

$$s_0(\beta) := \text{the largest eigenvalue of } \mathcal{A} \text{ when } t \to \infty \,, \tag{60}$$

we ultimately reach the formula for spatiotemporal averages,

$$\overline{\langle a \rangle} = \frac{\partial s_0}{\partial \beta} \Big|_{\beta=0} \,. \tag{61}$$

Equation (61) connects the spatiotemporal averages with the largest eigenvalue of the generator of the evolution operator. It is one of the most important formulas in the cycle averaging theory. We need to study $\mathcal{L}^t$ for $t \to \infty$ to obtain (60). To make calculations easier, we turn to the *resolvent* of $\mathcal{L}^t$, i.e., the Laplace transform of $\mathcal{L}^t$.

$$\int_0^\infty dt \, e^{-st} \mathcal{L}^t = \frac{1}{s - \mathcal{A}} \,, \qquad \mathrm{Re}\, s > s_0 \,. \tag{62}$$

So, the leading eigenvalue of $\mathcal{A}$ is the pole of the resolvent of the evolution operator. In the next subsection, we will obtain the expression for the resolvent of $\mathcal{L}^t$ by a set of periodic orbits.

1.4.2 Spectral determinants

The discussion in Sect. 1.4.1 motivates us to calculate the leading eigenvalue of the generator $\mathcal{A}$. Put it in another way, we need to solve equation

$$\det(s - \mathcal{A}) = 0 \tag{63}$$

whose answer gives the full spectrum of $\mathcal{A}$. We claim that spatiotemporal average can be calculated by periodic orbits in this system. Still, there isn't any hint how (63) is related to periodic orbits. On one hand, we see that periodic orbits are related to the trace of the evolution operator by the definition (51).

$$\mathrm{tr}\, \mathcal{L}^t = \int_{\mathcal{M}} du \, \mathcal{L}^t(u, u) = \int_{\mathcal{M}} du \, \delta\big(u - f^t(u)\big) \, e^{\beta A^t(u)} \,. \tag{64}$$

On the other hand, matrix identity

$$\ln \det M = \mathrm{tr}\, \ln M \tag{65}$$

relates the determinant of a matrix M on the left-hand side in (65) with its trace on the right-hand side. With these two pieces of information, we can express (63) in terms of $\mathrm{tr}\,\mathcal{L}^t$.

$$\ln\det\left(s-\mathcal{A}\right)=\mathrm{tr}\,\ln(s-\mathcal{A})=\int \mathrm{tr}\,\frac{1}{s-\mathcal{A}}\,ds\,. \tag{66}$$

Also by the definition of resolvent (62), we have

$$\det\left(s-\mathcal{A}\right)=\exp\left(\int ds\int_0^\infty dt\,e^{-st}\mathrm{tr}\,\mathcal{L}^t\right)\,. \tag{67}$$

The remaining part of this subsection is devoted to calculating $\int_0^\infty dt\,e^{-st}\mathrm{tr}\,\mathcal{L}^t$. For a given periodic orbit with period T_p, we decompose the trace (64) in two directions: one is parallel to the velocity field $u_\parallel$ and the other in the transverse direction $u_\perp$,

$$\int_0^\infty dt\,e^{-st}\mathrm{tr}\,\mathcal{L}^t=\int_0^\infty dt\,e^{-st}\int_{\mathcal{M}} du_\perp\,du_\parallel\delta\big(u_\perp-f_\perp^t(u)\big)\,\delta\Big(u_\parallel-f_\parallel^t(u)\Big)\,e^{\beta A^t(u)}\,.$$

We first calculate the integration in the parallel direction. This is a one-dimensional spatial integration. Due to the periodicity $u_\parallel=f_\parallel^{rT}(u)$ for $r=1,2,\cdots$, we split the integration in this parallel direction into infinitely many periods:

$$\begin{aligned}\int_0^\infty dt\,e^{-st}\oint_p du_\parallel\delta\Big(u_\parallel-f_\parallel^t(u)\Big)&=\int_0^\infty dt\,e^{-st}\int_0^{T_p}d\tau\,\|v(\tau)\|\,\delta\big(u_\parallel(\tau)-u_\parallel(\tau+t)\big) &(68)\\ &=\sum_{r=1}^\infty e^{-sT_pr}\int_0^{T_p}d\tau\,\|v(\tau)\|\int_{-\epsilon}^{\epsilon}dt\,e^{-st}\,\delta\big(u_\parallel(\tau)-u_\parallel(\tau+rT_p+t)\big)\,. &(69)\end{aligned}$$

The integrand in (69) is defined in a small time window $[-\epsilon,\epsilon]$. Within this window $u_\parallel(\tau)-u_\parallel(\tau+rT+t)=u_\parallel(\tau)-u_\parallel(\tau+t)\simeq-v(\tau)t$. So if we take $\epsilon\to0$,

$$\int_{-\epsilon}^{\epsilon}dt\,e^{-st}\,\delta\big(u_\parallel(\tau)-u_\parallel(\tau+rT_p+t)\big)=\frac{1}{\parallel v(\tau)\parallel}\,.$$

Therefore, we obtain the integration in the parallel direction,

$$\int_0^\infty dt\,e^{-st}\oint_p du_\parallel\delta\Big(u_\parallel-f_\parallel^t(u)\Big)=T_p\sum_{r=1}^\infty e^{-sT_pr}\,. \tag{70}$$

Now we calculate the trace integration in the transverse direction. In this case, we are actually integrating on a Poincaré section transverse to this periodic orbit. So $f_\perp^t(u)$ is the projected evolution function in this section, which has codimension one with the full state space. Therefore,

$$\int_{\mathcal{P}} du_\perp\delta\Big(u_\perp-f_\perp^{rT_p}(u)\Big)=\frac{1}{\left|\det\left(\mathbf{1}-M_p^r\right)\right|}\,. \tag{71}$$

Here M_p is the Floquet matrix projected on the Poincaré section of this periodic orbit.

Combine (70) and (71) and consider all periodic orbits inside this system, we obtain the *trace formula*

$$\int_0^\infty dt\,e^{-st}\mathrm{tr}\,\mathcal{L}^t=\sum_p T_p\sum_{r=1}^\infty\frac{e^{r(\beta A_p-sT_p)}}{\left|\det\left(\mathbf{1}-M_p^r\right)\right|}\,. \tag{72}$$

A_p is the integrated observable along the orbit for one period. Note, summation $\sum_p$ counts all periodic orbits inside this system. Substitute (72) into (67), we obtain the *spectral determinant*

$$\det(s-\mathcal{A}) = \exp\left(-\sum_p \sum_{r=1}^{\infty} \frac{1}{r} \frac{e^{r(\beta A_p - sT_p)}}{\left|\det\left(\mathbf{1}-M_p^r\right)\right|}\right) \tag{73}$$

of the flow.

1.4.3 Dynamical zeta functions

In the spectral determinant (73), $\left|\det\left(\mathbf{1}-M_p^r\right)\right|$ is approximately equal to the product of all the expanding eigenvalues of M_p. That is, $\left|\det\left(\mathbf{1}-M_p^r\right)\right| \simeq |\Lambda_p|^r$. Here, $\Lambda_p = \prod_e \Lambda_{p,e}$ is the product of the expanding eigenvalues of the Floquet matrix M_p. The accuracy of this approximation improves as $r \to \infty$. Substitute it into the spectral determinant (73), we have

$$\exp\left(-\sum_p \sum_{r=1}^{\infty} \frac{1}{r} \frac{e^{r(\beta A_p - sT_p)}}{|\Lambda_p|^r}\right) = \exp\left(\sum_p \ln\left(1-\frac{e^{\beta A_p - sT_p}}{|\Lambda_p|}\right)\right) = \prod_p \left(1-\frac{e^{\beta A_p - sT_p}}{|\Lambda_p|}\right),$$

where we have used the Taylor expansion $\ln(1-x) = -\sum_{n=1}^{\infty} \frac{x^n}{n}$. Then we obtain the *dynamical zeta function*,

$$1/\zeta = \prod_p (1-t_p), \qquad \text{with} \qquad t_p = \frac{e^{\beta A_p - sT_p}}{|\Lambda_p|}. \tag{74}$$

Formulas (61), (73) and (74) are the ultimate goal of the discussion in this section. They tell us that the spatiotemporal average is determined by the leading eigenvalue of the generator of the evolution operator $\mathcal{A}$, and the eigenspectrum of $\mathcal{A}$ can be obtained by the whole set of periodic orbits inside this system. Formula (73) precisely describes our perspective on chaotic deterministic flows. The flow on the global attractor can be visualized as a walk chaperoned by a hierarchy of unstable invariant solutions (equilibria, periodic orbits) embedded in the attractor. An ergodic trajectory shadows one such invariant solution for a while, is expelled along its unstable manifold, settles into the neighborhood of another invariant solution for a while, and repeats this process forever. Together, the infinite set of these unstable invariant solutions forms the skeleton of the strange attractor, and in fact, spatiotemporal averages can be accurately calculated as a summation taken over contributions from periodic orbits weighted by their stabilities [16, 22].

In practice, we truncate (73) or (74) according to the topological length of periodic orbits, which is primarily established by symbolic dynamics, or if not available, by the stability of periodic orbits. This technique is called *cycle expansion*, whose effectiveness has been demonstrated in a few one-dimensional maps [3, 4] and ergodic flows [13, 16, 56]. See [22] for more details.

CHAPTER II

SYMMETRIES IN DYNAMICAL SYSTEMS

Symmetries play an important role in physics. In the study of pattern formation [20], patterns with different symmetries form under different boundary conditions or initial conditions. By considering symmetries only, quite a few prototype equations such as complex Ginzburg-Landau equation [2] are proposed and have abundant applications in many fields. So, in general, symmetries help create a wonderful physical world for us. However, in the analysis of chaotic systems, symmetries introduce drifts of orbits along the symmetry directions and thus make the geometrical structure of the global attractor more complicated than it really is. In this case, symmetries should be reduced before we conducting any analysis. In this chapter, we review the basic notions of group theory, symmetry reduction methods, and establish the relation between dynamics in the full state space and that in the symmetry-reduced state space.

2.1 Group theory and symmetries: a review

In quantum mechanics, whenever a system exhibits some symmetry, the corresponding symmetry group commutes with the Hamiltonian of this system, namely, $[U(g), H] = U(g)H - HU(g) = 0$. Here $U(g)$ denotes the operation corresponding to symmetry g whose meaning will be explained soon. The set of eigenstates with degeneracy ℓ, $\{\phi_1, \phi_2, \cdots, \phi_\ell\}$, corresponding to the same system energy $H\psi_i = E_n\psi_i$, is invariant under the symmetry since $U(g)\psi_i$ are also eigenvectors for the same energy. This information helps us understand the spectrum of a Hamiltonian and the quantum mechanical selection rules. We now apply the same idea to the classical evolution operator $\mathcal{L}^t(u_e, u_s)$ for a system $f^t(u)$ equivariant under a discrete symmetry group $G = \{e, g_2, g_3, \cdots, g_{|G|}\}$ of order $|G|$:

$$f^t(Dg)u) = D(g)\, f^t(u) \quad \text{for} \quad \forall g \in G\,. \tag{75}$$

We start with a review of some basic facts of the group representation theory. Some examples of good references on this topic are ref. [47, 82].

Suppose group G acts on a linear space V and function $\rho(u)$ is defined on this space $u \in V$. Each element $g \in G$ will transform point u to $D(g)u$. At the same time, $\rho(u)$ is transformed to $\rho'(u)$. The value $\rho(u)$ is unchanged after state point u is transformed to $D(g)u$, so $\rho'(D(g)u) = \rho(u)$. Denote $U(g)\rho(u) = \rho'(u)$, so we have

$$U(g)\rho(u) = \rho(D(g)^{-1}u)\,. \tag{76}$$

This is how functions are transformed by group operations. Note, $D(g)$ is the representation of G in the form of space transformation matrices. The operator $U(g)$, which acts on the function space, is not the same as group operation $D(g)$, so (76) does not mean that $\rho(u)$ is invariant under G. Example 2.1 gives the space transformation matrices of C_3.

Example 2.1 A matrix representation of cyclic group C_3. *A 3-dimensional matrix representation of the 3-element cyclic group $C_3 = \{e, C^{1/3}, C^{2/3}\}$ is given by the three rotations by $2\pi/3$ around the*

z-axis in a 3-dimensional state space,

$$\begin{aligned} D(e) &= \begin{bmatrix} 1 & & \\ & 1 & \\ & & 1 \end{bmatrix}, \quad D(C^{1/3}) = \begin{bmatrix} \cos\frac{2\pi}{3} & -\sin\frac{2\pi}{3} & \\ \sin\frac{2\pi}{3} & \cos\frac{2\pi}{3} & \\ & & 1 \end{bmatrix}, \\ D(C^{2/3}) &= \begin{bmatrix} \cos\frac{4\pi}{3} & -\sin\frac{4\pi}{3} & \\ \sin\frac{4\pi}{3} & \cos\frac{4\pi}{3} & \\ & & 1 \end{bmatrix}. \end{aligned}$$

(continued in Example 2.2)

2.1.1 Regular representation

An operator $U(g)$ which acts on an infinite-dimensional function space is too abstract to analyze. We would like to represent it in a more familiar way. Suppose there is a function $\rho(u)$ with symmetry G defined in full state space $\mathcal{M}$, then full state space can be decomposed as a union of $|G|$ tiles each of which is obtained by transforming the fundamental domain,

$$\mathcal{M} = \bigcup_{g \in G} g\hat{\mathcal{M}}\,, \tag{77}$$

where $\hat{\mathcal{M}}$ is the chosen fundamental domain. So $\rho(u)$ takes $|G|$ different forms by (76) in each sub-domain in (77). Now, we obtained a natural choice of a set of bases in this function space called the *regular bases*,

$$\{\rho_1^{reg}(\hat{u}), \rho_2^{reg}(\hat{u}), \cdots, \rho_{|G|}^{reg}(\hat{u})\} = \{\rho(\hat{u}), \rho(g_2\hat{u}), \cdots, \rho(g_{|G|}\hat{u})\}\,. \tag{78}$$

Here, for notation simplicity we use $\rho(g_i\hat{u})$ to represent $\rho(D(g_i\hat{u}))$ without ambiguity. These bases are constructed by applying $U(g^{-1})$ to $\rho(\hat{u})$ for each $g \in G$, with $\hat{u}$ a point in the fundamental domain. The $[|G| \times |G|]$ matrix representation of the action of $U(g)$ in bases (78) is called the *(left) regular representation* $D^{reg}(g)$. Relation (76) says that $D^{reg}(g)$ is a permutation matrix, so each row or column has only one nonzero element.

We have a simple trick to obtain the regular representation quickly. Suppose the element at the ith row and the jth column of $D^{reg}(g)$ is 1. It means $\rho(g_i\hat{u}) = U(g)\rho(g_j\hat{u})$, which is $g_i = g^{-1}g_j \implies g^{-1} = g_i g_j^{-1}$. Namely,

$$D^{reg}(g)_{ij} = \delta_{g^{-1},\, g_i g_j^{-1}}\,. \tag{79}$$

So if we arrange the columns of the multiplication table by the inverse of the group elements, then setting positions with g^{-1} to 1 defines the regular representation $D^{reg}(g)$. Note, the above relation can be further simplified to $g = g_j g_i^{-1}$, but it exchanges the rows and columns of the multiplication table, so $g = g_j g_i^{-1}$ should not be used to get $D^{reg}(g)$. On the other hand, it is easy to see that the regular representation of group element e is always the identity matrix.

Example 2.2 The regular representation of cyclic group C_3. *(continued from Example 2.1) Take an arbitrary function $\rho(u)$ over the state space $u \in \mathcal{M}$, and define a fundamental domain $\hat{\mathcal{M}}$ as a 1/3 wedge, with axis z as its (symmetry invariant) edge. The state space is tiled with three copies of the wedge,*

$$\mathcal{M} = \hat{\mathcal{M}}_1 \cup \hat{\mathcal{M}}_2 \cup \hat{\mathcal{M}}_3 = \hat{\mathcal{M}} \cup C^{1/3}\hat{\mathcal{M}} \cup C^{2/3}\hat{\mathcal{M}}\,.$$

Table 1: The multiplication tables of the (a) group C_2 and (b) C_3.

(a)

C_2	e	σ^{-1}
e	e	σ
σ	σ	e

(b)

C_3	e	$(C^{1/3})^{-1}$	$(C^{2/3})^{-1}$
e	e	$C^{2/3}$	$C^{1/3}$
$C^{1/3}$	$C^{1/3}$	e	$C^{2/3}$
$C^{2/3}$	$C^{2/3}$	$C^{1/3}$	e

Function $\rho(u)$ can be written as the 3-dimensional vector of functions over the fundamental domain $\hat{u} \in \hat{\mathcal{M}}$,

$$(\rho_1^{reg}(\hat{u}), \rho_2^{reg}(\hat{u}), \rho_3^{reg}(\hat{u})) = (\rho(\hat{u}), \rho(C^{1/3}\hat{u}), \rho(C^{2/3}\hat{u}))\,. \tag{80}$$

The multiplication table of C_3 is given in Table 1. By (79), the regular representation matrices $D^{reg}(g)$ have '1' at the location of g^{-1} in the multiplication table, '0' elsewhere. The actions of the operator $U(g)$ are now represented by permutations matrices (blank entries are zeros):

$$D^{reg}(e) = \begin{bmatrix} 1 & & \\ & 1 & \\ & & 1 \end{bmatrix}\,, \quad D^{reg}(C^{1/3}) = \begin{bmatrix} & 1 & \\ & & 1 \\ 1 & & \end{bmatrix}\,, \quad D^{reg}(C^{2/3}) = \begin{bmatrix} & & 1 \\ 1 & & \\ & 1 & \end{bmatrix}\,. \tag{81}$$

Table 2: The multiplication table of D_3, the group of symmetries of an equilateral triangle.

D_3	e	$(\sigma_{12})^{-1}$	$(\sigma_{23})^{-1}$	$(\sigma_{31})^{-1}$	$(C^{1/3})^{-1}$	$(C^{2/3})^{-1}$
e	e	σ_{12}	σ_{23}	σ_{31}	$C^{2/3}$	$C^{1/3}$
σ_{12}	σ_{12}	e	$C^{1/3}$	$C^{2/3}$	σ_{31}	σ_{23}
σ_{23}	σ_{23}	$C^{2/3}$	e	$C^{1/3}$	σ_{12}	σ_{31}
σ_{31}	σ_{31}	$C^{1/3}$	$C^{2/3}$	e	σ_{23}	σ_{12}
$C^{1/3}$	$C^{1/3}$	σ_{31}	σ_{12}	σ_{23}	e	$C^{2/3}$
$C^{2/3}$	$C^{2/3}$	σ_{23}	σ_{31}	σ_{12}	$C^{1/3}$	e

Example 2.3 The regular representation of dihedral group D_3. $D_3 = \{e, \sigma_{12}, \sigma_{23}, \sigma_{31}, C^{1/3}, C^{2/3}\}$ *represents the symmetries of a triangle with equal sides. $C^{1/3}$ and $C^{2/3}$ are rotations by $2\pi/3$ and $4\pi/3$ respectively. σ_{12}, σ_{23} and σ_{31} are 3 reflections. The regular bases in this case are*

$$\Big(\rho(\hat{u}),\, \rho(\sigma_{12}\hat{u}),\, \rho(\sigma_{23}\hat{u}),\, \rho(\sigma_{31}\hat{u}),\, \rho(C^{1/3}\hat{u}),\, \rho(C^{2/3}\hat{u})\Big)\,.$$

It helps us obtain the multiplication table quickly by the following relations

$$\sigma_{31} = C^{1/3}\sigma_{12}\,, \quad \sigma_{23} = C^{2/3}\sigma_{12}\,, \quad C^{1/3}\sigma_{12} = \sigma_{12}C^{2/3}\,, \quad C^{2/3}\sigma_{12} = \sigma_{12}C^{1/3}\,. \tag{82}$$

The multiplication table of D_3 is given in Table 2. By (79), the 6 regular representation matrices $D^{reg}(g)$ have '1' at the location of g^{-1} in the multiplication table, '0' elsewhere. For example, the regular representation of the action of operators $U(\sigma_{23})$ and $U(C^{2/3})$ are, respectively:

$$D^{reg}(\sigma_{23}) = \begin{bmatrix} 0 & 0 & 1 & 0 & 0 & 0 \\ 0 & 0 & 0 & 0 & 0 & 1 \\ 1 & 0 & 0 & 0 & 0 & 0 \\ 0 & 0 & 0 & 0 & 1 & 0 \\ 0 & 0 & 0 & 1 & 0 & 0 \\ 0 & 1 & 0 & 0 & 0 & 0 \end{bmatrix}\,, \quad D^{reg}(C^{1/3}) = \begin{bmatrix} 0 & 0 & 0 & 0 & 1 & 0 \\ 0 & 0 & 0 & 1 & 0 & 0 \\ 0 & 1 & 0 & 0 & 0 & 0 \\ 0 & 0 & 1 & 0 & 0 & 0 \\ 0 & 0 & 0 & 0 & 0 & 1 \\ 1 & 0 & 0 & 0 & 0 & 0 \end{bmatrix}\,.$$

2.1.2 Irreducible representations

$U(g)$ is a linear operator under the regular bases. Any linearly independent combination of the regular bases can be used as new bases, and then the representation of $U(g)$ changes respectively. So we ask a question: can we find a new set of bases

$$\rho_i^{irr} = \sum_j S_{ij} \rho_j^{reg} \tag{83}$$

such that the new representation $D^{irr}(g) = S D^{reg}(g) S^{-1}$ is block-diagonal for any $g \in G$?

$$D^{irr}(g) = \begin{bmatrix} D^{(1)}(g) & & \\ & D^{(2)}(g) & \\ & & \ddots \end{bmatrix} = \bigoplus_{\mu=1}^{r} d_\mu D^{(\mu)}(g) \,. \tag{84}$$

In such a block-diagonal representation, the subspace corresponding to each diagonal block is invariant under G and the action of $U(g)$ can be analyzed subspace by subspace. It can be easily checked that for each μ, $D^{(\mu)}(g)$ for all $g \in G$ form another representation (*irreducible representation*, or *irrep*) of group G. Here, r denotes the total number of irreps of G. The same irrep may show up more than once in the decomposition (84), so the coefficient d_μ denotes the number of its copies. Moreover, it is proved [47] that d_μ is also equal to the dimension of $D^{(\mu)}(g)$ in (84). Therefore, we have a relation

$$\sum_{\mu=1}^{r} d_\mu^2 = |G| \,.$$

Example 2.4 Irreps of cyclic group C_3. *(continued from Example 2.2) For C_2 whose multiplication table is in Table 1, we can form the symmetric base $\rho(\hat{u})+\rho(\sigma\hat{u})$ and the antisymmetric base $\rho(\hat{u})-\rho(\sigma\hat{u})$. You can verify that under these new bases, C_2 is block-diagonalized. We would like to generalize this symmetric-antisymmetric decomposition to the order 3 group C_3. Symmetrization can be carried out on any number of functions, but there is no obvious anti-symmetrization. We draw instead inspiration from the Fourier transformation for a finite periodic lattice, and construct from the regular bases (80) a new set of bases*

$$\rho_0^{irr}(\hat{u}) = \frac{1}{3}\left[\rho(\hat{u}) + \rho(C^{1/3}\hat{u}) + \rho(C^{2/3}\hat{u})\right] \tag{85}$$

$$\rho_1^{irr}(\hat{u}) = \frac{1}{3}\left[\rho(\hat{u}) + \omega\,\rho(C^{1/3}\hat{u}) + \omega^2\rho(C^{2/3}\hat{u})\right] \tag{86}$$

$$\rho_2^{irr}(\hat{u}) = \frac{1}{3}\left[\rho(\hat{u}) + \omega^2\rho(C^{1/3}\hat{u}) + \omega\,\rho(C^{2/3}\hat{u})\right] \,. \tag{87}$$

Here $\omega = e^{2i\pi/3}$. The representation of group C_3 in this new bases is block-diagonal by inspection:

$$D^{irr}(e) = \begin{bmatrix} 1 & & \\ & 1 & \\ & & 1 \end{bmatrix} \,, \quad D^{irr}(C^{1/3}) = \begin{bmatrix} 1 & 0 & 0 \\ 0 & \omega & 0 \\ 0 & 0 & \omega^2 \end{bmatrix} \,, \quad D^{irr}(C^{2/3}) = \begin{bmatrix} 1 & 0 & 0 \\ 0 & \omega^2 & 0 \\ 0 & 0 & \omega \end{bmatrix} \,. \tag{88}$$

So C_3 has three 1-dimensional irreps. Generalization to any C_n is immediate: this is just a finite lattice Fourier transform.

Character tables. Finding a transformation S which simultaneously block-diagonalizes the regular representation of each group element sounds difficult. However, suppose it can be achieved and we obtain a set of irreps $D^{(\mu)}(g)$, then according to Schur's lemmas [47], $D^{(\mu)}(g)$ must satisfy a set of orthogonality relations:

$$\frac{d_\mu}{|G|}\sum_g D^{(\mu)}_{il}(g)D^{(\nu)}_{mj}(g^{-1}) = \delta_{\mu\nu}\delta_{ij}\delta_{lm}\,. \tag{89}$$

Denote the trace of irrep $D^{(\mu)}$ as $\chi^{(\mu)}$, which is referred to as the *character* of $D^{(\mu)}$. Properties of irreps can be derived from (89), and we list them as follows:

1. The number of irreps is the same as the number of classes.
2. Dimensions of irreps satisfy $\sum_{\mu=1}^{r} d_\mu^2 = |G|$
3. Orthonormal relation I : $\sum_{i=1}^{r} |K_i|\chi_i^{(\mu)}\chi_i^{(\nu)*} = |G|\delta_{\mu\nu}$.
   Here, the summation goes through all classes of this group, and $|K_i|$ is the number of elements in class i. This weight comes from the fact that elements in the same class have the same character. Symbol $*$ means the complex conjugate.
4. Orthonormal relation II : $\sum_{\mu=1}^{r} \chi_i^{(\mu)}\chi_j^{(\mu)*} = \frac{|G|}{|K_i|}\delta_{ij}$.

The characters for all classes and irreps of a finite group are conventionally arranged into a *character table*, a square matrix whose rows represent different classes and columns represent different irreps. Rules 1 and 2 help determine the number of irreps and their dimensions. As the matrix representation of class $\{e\}$ is always the identity matrix, the first row is always the dimension of the corresponding representation. All entries of the first column are always 1, because the symmetric irrep is always one-dimensional. To compute the remaining entries, we should use properties 3, 4 and the class multiplication tables. Spectroscopists conventions use labels A and B for symmetric, respectively antisymmetric nondegenerate irreps, and E, T, G, H for doubly, triply, quadruply, quintuply degenerate irreps.

Table 3: Character tables of C_2, C_3 and D_3. The classes $\{\sigma_{12}, \sigma_{13}, \sigma_{14}\}$, $\{C^{1/3}, C^{2/3}\}$ are denoted 3σ, $2C$, respectively.

C_2	A	B
e	1	1
σ	1	-1

C_3	A	E	
e	1	1	1
$C^{1/3}$	1	ω	ω^2
$C^{2/3}$	1	ω^2	ω

D_3	A	B	E
e	1	1	2
3σ	1	-1	0
$2C$	1	1	-1

Example 2.5 Character table of D_3. *(continued from Example 2.3) Let us construct Table 3. one-dimensional representations are denoted by A and B, depending on whether the basis function is symmetric or antisymmetric with respect to transpositions σ_{ij}. E denotes the two-dimensional representation. As D_3 has 3 classes, the dimension sum rule $d_1^2 + d_2^2 + d_3^2 = 6$ has only one solution $d_1 = d_2 = 1$, $d_3 = 2$. Hence there are two one-dimensional irreps and one two-dimensional irrep. The first row is $1, 1, 2$, and the first column is $1, 1, 1$ corresponding to the one-dimensional symmetric representation. We take two approaches to figure out the remaining 4 entries. First, since B is an antisymmetric one-dimensional representation, so the characters should be ± 1. We anticipate $\chi^B(\sigma) = -1$ and can quickly figure out the remaining 3 positions. Then we check that the obtained table satisfies the orthonormal relations.*

Second, denote $\chi^B(\sigma) = x$ and $\chi^E(\sigma) = y$, then from the orthonormal relation of the second column with the first column and itself, we obtain $1 + x + 2y = 0$ and $1 + x^2 + y^2 = 6/3$. Then we get two sets of solutions, one of which is incompatible with other orthonormal relations, so we are left with $x = -1$, $y = 0$. Similarly, we can get the other two characters.

2.1.3 Projection operator

We have listed the properties of irreps and the techniques of constructing a character table, but we still do not know how to construct the similarity transformation S which takes a regular representation into a block-diagonal form. Think of it in another way, each irrep is associated with an invariant subspace, so by projecting an arbitrary function $\rho(u)$ into its invariant subspaces, we find the transformation (83). One of these invariant subspaces is $\sum_g \rho(g\hat{u})$, which is the basis of the one-dimensional symmetric irrep A. For C_3, it is (85). But how to get the others? We resort to the projection operator:

$$P_i^{(\mu)} = \frac{d_\mu}{|G|} \sum_g \left(D_{ii}^{(\mu)}(g) \right)^* U(g) \,. \tag{90}$$

It projects an arbitrary function into the ith basis of irrep $D^{(\mu)}$ provided the diagonal elements of this representation $D_{ii}^{(\mu)}$ are known. $P_i^{(\mu)} \rho(u) = \rho_i^{(\mu)}$. Here, symbol $*$ means the complex conjugate. For unitary groups $\left(D_{ii}^{(\mu)}(g) \right)^* = D_{ii}^{(\mu)}(g^{-1})$. Summing i in (90) gives

$$P^{(\mu)} = \frac{d_\mu}{|G|} \sum_g \left(\chi^{(\mu)}(g) \right)^* U(g) \,. \tag{91}$$

This is also a projection operator which projects an arbitrary function onto the sum of the bases of irrep $D^{(\mu)}$.

Note, for one-dimensional representations, (91) is equivalent to (90). The projection operator is known after we obtain the character table, since the character of an one-dimensional matrix is the matrix itself. However, for two-dimensional or higher-dimensional representations, we need to know the diagonal elements $D_{ii}^{(\mu)}$ in order to get the bases of invariant subspaces. That is to say, (90) should be used instead of (91) in this case. Example 2.6 illustrates this point. The two one-dimensional irreps are obtained by (91), but the other four two-dimensional irreps are obtained by (90).

Example 2.6 Bases for irreps of D_3. *(continued from Example 2.3) We use projection operator (91) to obtain the bases of irreps of D_3. From Table 3, we have*

$$P^A \rho(\hat{u}) = \frac{1}{6}\left[\rho(\hat{u}) + \rho(\sigma_{12}\hat{u}) + \rho(\sigma_{23}\hat{u}) + \rho(\sigma_{31}\hat{u}) + \rho(C^{1/3}\hat{u}) + \rho(C^{2/3}\hat{u}) \right] \tag{92}$$

$$P^B \rho(\hat{u}) = \frac{1}{6}\left[\rho(\hat{u}) - \rho(\sigma_{12}\hat{u}) - \rho(\sigma_{23}\hat{u}) - \rho(\sigma_{31}\hat{u}) + \rho(C^{1/3}\hat{u}) + \rho(C^{2/3}\hat{u}) \right] \,. \tag{93}$$

For projection into irrep E, we need to figure out the explicit matrix representation first. Obviously, the following 2 by 2 matrices are E irreps.

$$D^E(e) = \begin{bmatrix} 1 & 0 \\ 0 & 1 \end{bmatrix} , \quad D^E(C^{1/3}) = \begin{bmatrix} \omega & 0 \\ 0 & \omega^2 \end{bmatrix} , \quad D^E(C^{2/3}) = \begin{bmatrix} \omega^2 & 0 \\ 0 & \omega \end{bmatrix} \tag{94}$$

$$D^E(\sigma_{12}) = \begin{bmatrix} 0 & 1 \\ 1 & 0 \end{bmatrix} , \quad D^E(\sigma_{23}) = \begin{bmatrix} 0 & \omega^2 \\ \omega & 0 \end{bmatrix} , \quad D^E(\sigma_{31}) = \begin{bmatrix} 0 & \omega \\ \omega^2 & 0 \end{bmatrix} \,. \tag{95}$$

So apply projection operator (90) on $\rho(\hat{u})$ *and* $\rho(\sigma_{12}\hat{u})$*, we get*

$$P_1^E\rho(\hat{u}) = \frac{1}{6}\left[\rho(\hat{u}) + \omega\rho(C^{1/3}\hat{u}) + \omega^2\rho(C^{2/3}\hat{u})\right] \tag{96}$$

$$P_2^E\rho(\hat{u}) = \frac{1}{6}\left[\rho(\hat{u}) + \omega^2\rho(C^{1/3}\hat{u}) + \omega\rho(C^{2/3}\hat{u})\right] \tag{97}$$

$$P_1^E\rho(\sigma_{12}\hat{u}) = \frac{1}{6}\left[\rho(\sigma_{12}\hat{u}) + \omega\rho(\sigma_{31}\hat{u}) + \omega^2\rho(\sigma_{23}\hat{u})\right] \tag{98}$$

$$P_2^E\rho(\sigma_{12}\hat{u}) = \frac{1}{6}\left[\rho(\sigma_{12}\hat{u}) + \omega^2\rho(\sigma_{31}\hat{u}) + \omega\rho(\sigma_{23}\hat{u}) \,.\right] \tag{99}$$

The above derivation has used formulas (82). Under the invariant bases

$$\left\{P^A\rho(\hat{u}), P^B\rho(\hat{u}), P_1^E\rho(\hat{u}), P_2^E\rho(\sigma_{12}\hat{u}), P_1^E\rho(\sigma_{12}\hat{u}), P_2^E\rho(\hat{u})\right\} ,$$

we have

$$D^{irr}(\sigma_{23}) = \begin{bmatrix} 1 & 0 & 0 & 0 & 0 & 0 \\ 0 & -1 & 0 & 0 & 0 & 0 \\ 0 & 0 & 0 & \omega^2 & 0 & 0 \\ 0 & 0 & \omega & 0 & 0 & 0 \\ 0 & 0 & 0 & 0 & 0 & \omega^2 \\ 0 & 0 & 0 & 0 & \omega & 0 \end{bmatrix} \quad D^{irr}(C^{1/3}) = \begin{bmatrix} 1 & 0 & 0 & 0 & 0 & 0 \\ 0 & 1 & 0 & 0 & 0 & 0 \\ 0 & 0 & \omega & 0 & 0 & 0 \\ 0 & 0 & 0 & \omega^2 & 0 & 0 \\ 0 & 0 & 0 & 0 & \omega & 0 \\ 0 & 0 & 0 & 0 & 0 & \omega^2 \end{bmatrix} .$$

The C_3 and D_3 examples used in this section can be generalized to any C_n and D_n. For references, Example 2.7, Example 2.8 and Example 2.9 give the character tables of C_n and D_n.

Example 2.7 Character table of cyclic group C_n. *The symmetry under a discrete rotation by angle* $2\pi/n$ *gives birth to a cyclic group* $C_n = \{e, C_n, C_n^2, \cdots, C_n^{n-1}\}$*. Since* C_n *is Abelian, each element forms a separate class, and thus* C_n *has* n *one-dimensional irreducible representations. The characters multiply as group elements:* $\chi_\alpha(C_n^i)\chi_\alpha(C_n^j) = \chi_\alpha(C_n^{i+j}) \mod n$*. Therefore, we get Table 4.*

Table 4: Character table of cyclic group C$_n$. Here $k, j = 1, 2, \cdots, n-1$.

C$_n$	A	Γ_j
e	1	1
C_n^k	1	$\exp(\frac{i2\pi kj}{n})$

Example 2.8 Character table of dihedral group $D_n = C_{nv}$, n odd. *The* D_n *group*

$$D_n = \{e, C_n, C_n^2, \cdots, C_n^{n-1}, \sigma, C_n\sigma, \cdots, C_n^{n-1}\sigma\}$$

has n *rotation elements and* n *reflections. Group elements satisfies* $C_n^i \cdot C_n^j\sigma = C_n^j\sigma \cdot C_n^{n-i}$*, so* C_n^i *and* C_n^{n-i} *form a class. Also,* $C_n^{n-i} \cdot C_n^{2i+j}\sigma = C_n^j\sigma \cdot C_n^{n-i}$ *implies that* $C_n^j\sigma$ *and* $C_n^{2i+j}\sigma$ *are in the same class. Therefore, there are only three different types of classes:* $\{e\}$, $\{C_n^k, C_n^{n-k}\}$ *and* $\{\sigma, C_n\sigma, \cdots, C_n^{n-1}\sigma\}$*. The total number of classes is* $(n+3)/2$*. In this case, there are 2 one-dimensional irreducible representations (symmetric* A_1 *and anti-symmetric* A_2 *) and* $(n-1)/2$ *two-dimensional irreducible representations. In the* j*th two-dimensional irreducible representation, class* $\{e\}$ *has form* $\left(\begin{smallmatrix} 1 & 0 \\ 0 & 1 \end{smallmatrix}\right)$*, class* $\{C_n^k, C_n^{n-k}\}$ *has form* $\left(\begin{smallmatrix} \exp(\frac{i2\pi kj}{n}) & 0 \\ 0 & \exp(-\frac{i2\pi kj}{n}) \end{smallmatrix}\right)$*, and class* $\{\sigma, C_n\sigma, \cdots, C_n^{n-1}\sigma\}$ *has form* $\left(\begin{smallmatrix} 0 & 1 \\ 1 & 0 \end{smallmatrix}\right)$*. We get Table 5.*

Example 2.9 Character table of dihedral group $D_n = C_{nv}$, n even. *In this case, there are* $(n+6)/2$ *classes:* $\{e\}$, $\{C^{1/2}\}$, $\{C^{k/n}, C^{(n-k)/n}\}$, $\{\sigma, \sigma C^{2/n}, \cdots, \sigma C^{(n-2)/n}\}$ *and* $\{\sigma C^{1/n}, \sigma C^{3/n}, \cdots, \sigma C^{(n-1)/n}\}$*. There are four different one-dimensional irreducible representations, whose characters are* ± 1 *under reflection* σ *and shift-reflect operation* $\sigma C^{1/n}$*. We get Table 6.*

Table 5: Character table of dihedral group $\mathrm{D}_n = C_{nv}$, n odd.

D_n (n odd)	A_1	A_2	E_j
e	1	1	2
C_n^k, C_n^{n-k}	1	1	$2\cos(\frac{2\pi kj}{n})$
$\sigma, \sigma C_n^1, \cdots, \sigma C_n^{n-1}$	1	-1	0

Table 6: Character table of dihedral group $\mathrm{D}_n = C_{nv}$, n even. Here $k, j = 1, 2, \cdots, n-1$.

D_n (n even)	A_1	A_2	B_1	B_2	E_j
e	1	1	1	1	2
$C^{1/2}$	1	1	$(-1)^{n/2}$	$(-1)^{n/2}$	$2(-1)^j$
$C^{k/n}, C^{(n-k)/n}$ (k odd)	1	1	-1	-1	$2\cos(\frac{2\pi kj}{n})$
$C^{k/n}, C^{(n-k)/n}$ (k even)	1	1	1	1	$2\cos(\frac{2\pi kj}{n})$
$\sigma, \sigma C^{2/n}, \cdots, \sigma C^{(n-2)/n}$	1	-1	1	-1	0
$\sigma C^{1/n}, \sigma C^{3/n}, \cdots, \sigma C^{(n-1)/n}$	1	-1	-1	1	0

2.2 *Symmetry reduction for dynamical systems*

In a dynamical system with discrete or continuous symmetries, points in the state space which are related to each other by symmetry operation should be treated as a group. Each member of this group has the same dynamical properties, so we say that they are dynamically equivalent. It is a good practice to choose a single representative in each group and study the dynamics of this representative point instead. This treatment is called *symmetry reduction*. The new state space that this representative point lives in is called the *(symmetry-)reduced state space* After it was invented, symmetry reduction becomes extremely successful for simplifying the analysis of a dynamical system with symmetries. In this section, we will discuss symmetry reduction techniques and study the tangent dynamics in the reduced state space.

2.2.1 Continuous symmetry reduction

We use the same setup as in Sect. 1.3 and copy a few equations here for convenience. The content of this subsection is based on the materials in [22]. Let $\dot{u} = v(u)\,, u(x,t) \in \mathbb{R}^n$ define a flow. Usually we omit the dependence on coordinates, and write $u(t)$. Denote the evolution semigroup of this flow by $u(t) = f^t(u_0)$. We say that this flow is equivariant under a continuous symmetry group G if

$$gv(u) = v(gu)\,, \quad gf^t(u) = f^t(gu) \quad \text{for any} \quad g \in G\,. \tag{100}$$

The two equations above are equivalent. In practical applications, G is always a Lie group. Basically, (100) means that if two starting states, which are related to each other by a group operation, evolve for the same period of time, then the end states are related by the same group operation.

Now we introduce the terminology that will be used in the later discussion. In is often more convenient to write the Lie group G in its exponential form

$$g(\phi) = e^{\phi \cdot \mathbf{T}} , \qquad \phi \cdot \mathbf{T} = \sum_{a=1}^{s} \phi_a \mathbf{T}_a , \tag{101}$$

where $\mathbf{T}_a$, $a = 1, 2 \cdots , s$ are the *generators* of G, and ϕ_a are the parameters of this group. Dot product refers to a sum over generators in this section. Generators of a real representation are antisymmetric:

$$\mathbf{T}_a{}^{\top} = -\mathbf{T}_a , \tag{102}$$

where $\mathbf{T}_a{}^{\top}$ denotes the transpose of $\mathbf{T}_a$. Let's work out a simple example. The translation group $\{g : g(x_0)u(x, t) = u(x + x_0, t)\}$ is denoted as $g(x_0) = \exp(x_0 \frac{\partial}{\partial x})$. Here, $\frac{\partial}{\partial x}$ is the only generator and x_0 is the parameter. Furthermore, we assume that the generators of $g(\phi)$ commute with each other: $\mathbf{T}_a \mathbf{T}_b = \mathbf{T}_b \mathbf{T}_a$.

We define the *group orbit* of a point u as

$$\mathrm{Orb}(u) = \{g\, u : g \in G\} . \tag{103}$$

A group orbit is an s-dimensional manifold, but it is not a real orbit. It is a collection of all dynamically equivalent points. The *group tangent* of state u is defined as

$$t_a(u)_i = (\mathbf{T}_a)_{ij} u_j , \tag{104}$$

which is basically a matrix-vector product. Note, (100) says that the flow equation is equivariant under G, but it does not mean that any orbit in the state space possesses all symmetries in G. Now we define several important invariant structures.

Equilibrium $u(t) = u(0)$. Namely, $v(u) = 0$.

Relative equilibrium A state point $u(x, t)$ is a relative equilibrium if

$$u(t) = g(t\, c)\, u(0) \; = \; e^{t\, c \cdot \mathbf{T}} u(0) , \tag{105}$$

where c is a constant. Definition (105) is equivalent to $v(u) = c \cdot t(u)$. A relative equilibrium is very similar to an equilibrium except for a constant drifting in the group direction.

Periodic orbit $u(T_p) = u(0)$. T_p is the period.

Relative periodic orbit Similar to periodic orbits, if a state returns to its initial state except for a group translation after a center time, then we say that this point is on a relative periodic orbit.

$$u_p(0) = g_p u_p(T_p) , \tag{106}$$

where T_p is the period. $g_p = g(\phi_p)$ takes the end state to the initial state. We use subscript p to indicate that the variable belongs to a periodic orbit or relative periodic orbit.

With the above setup, we illustrate how to use *slice* to reduce continuous symmetries. The idea is similar to a Poincaré section. We define a slice that cuts every group orbit only once, so that we can use this intersection point as the representative of the whole group orbit. The simplest slice is a flat hypersurface that is normal to the group tangent of a pre-specified point $\hat{u}'$:

$$\langle \hat{u} - \hat{u}' | t'_a \rangle = \langle \hat{u} | t'_a \rangle = 0 , \quad t'_a = t_a(\hat{u}') = \mathbf{T}_a \, \hat{u}' , \quad \text{for} \quad a = 1, 2, \cdots , s . \tag{107}$$

Here, we use a bra-ket notation for the inner product of two real vectors in $\mathbb{R}^n$,

$$\langle u|w\rangle = u^\top w = \sum_{i=1}^{n} u_i w_i \,.$$

A hat on a state indicates that it is a state in the symmetry-reduced state space. Definition (107) has used $\langle \hat{u}'|t'_a\rangle = \langle \hat{u}'|\mathbf{T}_a\,\hat{u}'\rangle = 0$ which is the result of the antisymmetry of $\mathbf{T}_a$ (102). Now, symmetry reduction turns out to be a process of finding a specific group element $g(\phi)$ that transforms each state u into the slice.

$$\hat{u} = g^{-1}(\phi)\,u\,. \tag{108}$$

$\hat{u}$ is the state on the slice that represents u and the whole group orbit of u. Note, it usually requires different group parameter ϕ for different states in (108). Equivalently, we can recover the state in the full state space by the state in the symmetry-reduced state space and the group parameter ϕ,

$$u = g(\phi)\,\hat{u}\,. \tag{109}$$

The symmetry reduction process described above is called the *post-processing* method. That is, we need to know the trajectory beforehand in order to reduce it into the slice. However, many a time, it is more efficient to integrate the system in the slice directly. This posts a question of what the dynamics is like in the slice. Let us start from finding the reduced velocity in the slice. Take the time derivative of both sides of (109), $v(g\hat{u}) = v(u) = \dot{g}\hat{u} + g\hat{v}$. Rewrite it with $\hat{v} = g^{-1}v(g\,\hat{u}) - g^{-1}\dot{g}\,\hat{u}$ and the equivariance condition (100) leads to $\hat{v} = v - g^{-1}\dot{g}\,\hat{u}$. Also, by (101) and the definition of the group tangent (104), we get

$$g^{-1}\dot{g}\,\hat{u} = \sum_{a=1}^{s}\dot{\phi}_a(\hat{u})\,\mathbf{T}_a\hat{u} = \sum_{a=1}^{s}\dot{\phi}_a(\hat{u})t_a(\hat{u})\,.$$

So the velocity in the slice is given as

$$\hat{v}(\hat{u}) = v(\hat{u}) \; - \sum_{a=1}^{s}\dot{\phi}_a(\hat{u})t_a(\hat{u}) \tag{110}$$

The dynamics of $\phi_a(\hat{u})$ is governed by the slice. Taking the time derivative of the slice condition (107) and substituting (110), we get

$$\langle t'_a|\hat{v}(\hat{u})\rangle = \langle t'_a|v(\hat{u})\rangle - \sum_{b=1}^{s}\langle t'_a|t_b(\hat{u})\rangle\,\dot{\phi}_b = 0\,, \quad \text{for} \quad a = 1, 2, \cdots, s\,.$$

This defines s linear equations with total s unknowns. Define the coefficient matrix as L whose element is

$$L(\hat{u})_{ab} = \langle t'_a|t_b(\hat{u})\rangle\,, \tag{111}$$

then we can solve the equation for $\dot{\phi}_a(\hat{u})$. In summary, the dynamics in the slice is governed by

$$\hat{v}(\hat{u}) \;=\; v(\hat{u}) - \sum_{a=1}^{s}\dot{\phi}_a(\hat{u})t_a(\hat{u})\,, \qquad \hat{u}\in\hat{\mathcal{M}} \tag{112}$$

$$\dot{\phi}_a(\hat{u}) \;=\; \sum_{b=1}^{s}(L^{-1})_{ab}\langle t'_b|v(\hat{u})\rangle\,, \qquad a = 1, 2, \cdots, s\,. \tag{113}$$

The above in-slice dynamics fails when L is singular. One obvious cause of failure is a situation where some t'_a are parallel. So when choosing the template points for defining the slice, we need to guarantee that t'_a, $a = 1, 2, \cdots, s$ are not parallel. Under this assumption, a slice fails only when the in-slice state $\hat{u}$ makes (111) singular. The set of these points defines the *border* of the slice.

When the group has only one parameter ϕ, then matrix L is a scalar and the above formula can be simplified as

$$\hat{v}(\hat{u}) = v(\hat{u}) - \dot{\phi}(\hat{u})t(\hat{u})\,, \qquad \hat{u} \in \hat{\mathcal{M}} \tag{114}$$

$$\dot{\phi}(\hat{u}) = \langle v(\hat{u})|t'\rangle / \langle t(\hat{u})|t'\rangle\,. \tag{115}$$

2.2.2 Tangent dynamics in the slice

Equations (112)(113) or (114)(115) describe the dynamics in the slice, by which we can obtain the whole in-slice trajectory given a starting in-slice state. However, sometimes we not only desire the in-slice orbit but also the tangent dynamics in the slice. More precisely, formulas (28) and (30) describe the tangent dynamics in the full state space. What are the corresponding formulas in the slice? What is the relation between Jacobian matrix in the slice and that in the full state space? This subsection is devoted to answering these questions. For simplicity, in the following, we assume that the continuous group has only one parameter, i.e., $s = 1$ in (101). Nevertheless, the technique described below can be easily extended to symmetries with more than one group parameter.

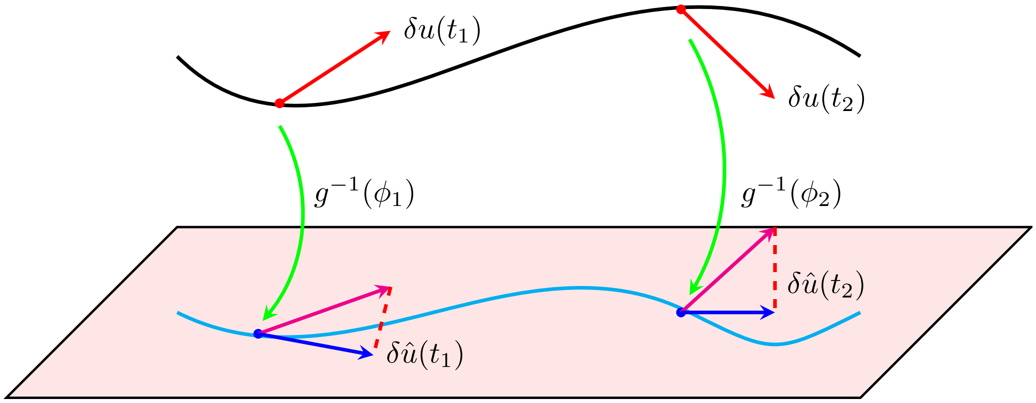

Figure 5: The relation between deformations in the full state space and in the slice. The pink plane is the slice. The black curve is a trajectory in the state space. The cyan curve is the corresponding trajectory in the slice. Infinitesimal deformation $\delta u(t_1)$ at time t_1 is transported to $\delta u(t_2)$ at time t_2. $\delta\hat{u}(t_1)$ and $\delta\hat{u}(t_2)$ are the in-slice correspondents.

First, we investigate how infinitesimal deformation is transformed into the slice from the full state space. We start from the slice condition (107). Infinitesimal deformation $\delta\hat{u}$ at $\hat{u}$ should be confined to the slice too, so we have a constraint

$$\langle \delta\hat{u}|t'\rangle = 0\,. \tag{116}$$

Here, the subscript of t' is omitted because we assume that there is only one group parameter. Taking the derivative of (109) we get $\delta u = \delta g(\phi)\hat{u} + g(\phi)\delta\hat{u}$ which is equivalent to

$$\delta\hat{u} = -\mathbf{T}\hat{u}\delta\phi + g(\phi)^{-1}\delta u\,.$$

Substituting it into (116), we get $\langle -\mathbf{T}\hat{u}\delta\phi + g(\phi)^{-1}\delta u | t'\rangle = 0$ which is

$$\delta\phi = \frac{\langle t'|g(\phi)^{-1}\delta u\rangle}{\langle t(\hat{u})|t'\rangle}\,. \tag{117}$$

Now $\delta\hat{u}$, the infinitesimal deformation in the slice, can be expressed by the deformation in the full state space δu:

$$|\delta\hat{u}\rangle = -\frac{\langle t'|g(\phi)^{-1}\delta u\rangle}{\langle t(\hat{u})|t'\rangle}|t(\hat{u})\rangle + g(\phi)^{-1}|\delta u\rangle\,,$$

that is,

$$|\delta\hat{u}\rangle = \left(\mathbf{1} - \frac{|t(\hat{u})\rangle\langle t'|}{\langle t(\hat{u})|t'\rangle}\right) g(\phi)^{-1}|\delta u\rangle := h(\hat{u})g(\phi)^{-1}|\delta u\rangle \tag{118}$$

The physical interpretation of (118) is manifest. Infinitesimal deformation δu at u in the full state space is first transformed to point $\hat{u}$ by $g(\phi)^{-1}$ and then projected into the slice by $h(\hat{u})$ illustrated in Figure 5. The matrix

$$h(\hat{u}) = \mathbf{1} - \frac{|t(\hat{u})\rangle\langle t'|}{\langle t(\hat{u})|t'\rangle} \tag{119}$$

projects infinitesimal deformation in the full state space into the slice. It is singular and has the following properties.

- $h(\hat{u})|t(\hat{u})\rangle = 0$: any infinitesimal deformation along the group tangent direction at $\hat{u}$ in the full state space will disappear after projection.
- $\langle t'|h(\hat{u}) = 0$: any vector projected into the slice will be perpendicular to the group tangent of the template point as expected. This property and the above one both prove that matrix $h(\hat{u})$ is not full-rank.
- In-slice velocity (114) turns out to be

  $$\hat{v}(\hat{u}) = v(\hat{u}) - \frac{\langle v(\hat{u})|t'\rangle}{\langle t(\hat{u})|t'\rangle}t(\hat{u}) = h(\hat{u})v(\hat{u})\,.$$

  The velocity field is transformed by matrix $h(\hat{u})$.

Since projection matrix (119) is singular, the projection reduces the dimension of the system by one. However, (119) is still expressed in the full state space. In practice, we desire to work in a lower-dimensional system after quotienting out the continuous symmetry. Now let's decrease the dimension of all matrices and vectors in the slice by one explicitly. Denote

$$h(\hat{u}) = \begin{bmatrix} h_1 \\ h_2 \\ \vdots \\ h_n \end{bmatrix}\,.$$

Each h_i is a row vector and n is the dimension of the full state space. From the second property of $h(\hat{u})$ we know that h_i are linear dependent: $t'_1 h_1 + t'_2 h_2 + \cdots + t'_n h_n = 0$. Here t'_i are components of vector t'. Assume $t'_\xi \neq 0$, then

$$h_\xi = \sum_{i=1, i\neq\xi}^{n} -\frac{t'_i}{t'_\xi} h_i$$

so h_ξ can be eliminated from $h(\hat{u})$:

$$h(\hat{u}) = \underbrace{\begin{bmatrix} 1 & & & & \\ & 1 & & & \\ & & \ddots & & \\ -\frac{t'_1}{t'_\xi} & -\frac{t'_2}{t'_\xi} & & \cdots & -\frac{t'_n}{t'_\xi} \\ & & & \ddots & \\ & & & & 1 \end{bmatrix}}_{n\times(n-1)} \underbrace{\begin{bmatrix} h_1 \\ \vdots \\ h_{\xi-1} \\ h_{\xi+1} \\ \vdots \\ h_n \end{bmatrix}}_{(n-1)\times n} := P' h^{(-)}(\hat{u})\,.$$

The above expression is the rank factorization of $h(\hat{u})$ with $h^{(-)}(\hat{u})$ a full-rank matrix. The superscript of the minus sign indicates that the matrix (vector) is $(n-1)$-dimensional. Similarly, from the slice condition $\langle t'|\hat{u}\rangle = 0$, we can reduce the dimension of a point on the slice by one

$$\hat{u} = P'\hat{u}^{(-)}$$

and also reduce the dimension of an infinitesimal deformation by one

$$\delta\hat{u} = P'\delta\hat{u}^{(-)}\,.$$

Here, $\hat{u}^{(-)}$ and $\delta\hat{u}^{(-)}$ are both $(n-1)$-dimensional vectors.

$$\hat{u}^{(-)} = [\hat{u}_1, \cdots, \hat{u}_{\xi-1}, \hat{u}_{\xi+1}, \cdots, \hat{u}_n]^\top\,, \quad \delta\hat{u}^{(-)} = [\delta\hat{u}_1, \cdots, \delta\hat{u}_{\xi-1}, \delta\hat{u}_{\xi+1}, \cdots, \delta\hat{u}_n]^\top\,.$$

Now relation (118) can be rewritten as:

$$|\delta\hat{u}^{(-)}\rangle = h^{(-)}(\hat{u}) g(\phi)^{-1} |\delta u\rangle \tag{120}$$

Note that the left side of the above equation is an $(n-1)$-dimensional vector while the right side $|\delta u\rangle$ is an n-dimensional vector and the $[(n-1)\times n]$ matrix $h^{(-)}(\hat{u})$ is the "projection" operator.

2.2.3 In-slice Jacobian matrix

Now let's turn to the transformation of the Jacobian matrix. In Figure 5, there is a trajectory from $u(t_1)$ to $u(t_2)$ in the full state space. The corresponding transformed in-slice trajectory is from $\hat{u}(t_1)$ to $\hat{u}(t_2)$. Infinitesimal deformations in the full state space and in the slice will be evolved by the Jacobian matrix in the full state space and in the slice respectively.

$$\begin{aligned} J\delta u(t_1) &= \delta u(t_2) && (121)\\ \hat{J}\delta\hat{u}^{(-)}(t_1) &= \delta\hat{u}^{(-)}(t_2)\,. && (122) \end{aligned}$$

Here, $J = J^{t_2-t_1}(u(t_1), t_1)$ and $\hat{J} = J^{t_2-t_1}(\hat{u}^{(-)}(t_1), t_1)$. For notation simplicity, we omit all parameters of Jacobian matrix if no confusion occurs. Substituting (120) into (122), we get

$$\hat{J}h^{(-)}(\hat{u}(t_1))g(\phi_1)^{-1}\delta u(t_1) = h^{(-)}(\hat{u}(t_2))g(\phi_2)^{-1}\delta u(t_2) = h^{(-)}(\hat{u}(t_2))g(\phi_2)^{-1}J\delta u(t_1)\,.$$

The last step above has used relation (121). This results in

$$\hat{J}h^{(-)}(\hat{u}(t_1))g(\phi_1)^{-1} = h^{(-)}(\hat{u}(t_2))g(\phi_2)^{-1}J\,. \tag{123}$$

$\hat{J}$ is an $[(n-1)\times(n-1)]$ matrix as we can easily see. The geometrical meaning of relation (123) is obvious in Figure 5. On the left side, the infinitesimal deformation $\delta u(t_1)$ at $u(t_1)$ is transported to the slice first, and then projected into the slice, after which it is evolved by $\hat{J}$ to in-slice point $\hat{u}(t_2)$. On the right side, the infinitesimal deformation $\delta u(t_1)$ at $u(t_1)$ is evolved first to $u(t_2)$ by J, then transported to the slice, and finally projected into the slice.

By (123), the relation between covariant vectors in the full state space and in the slice can be obtained for physically interesting invariant subsets: equilibria, relative equilibria, periodic orbits, and relative periodic orbits.

In-slice stability matrix of an equilibrium For an equilibrium $u(t_1) = u(t_2) := u_q$, we have $\hat{u}(t_1) = \hat{u}(t_2) := \hat{u}_q$ and $\phi_1 = \phi_2 := \phi_q$. Formula (123) becomes

$$\hat{J}h^{(-)}(\hat{u}_q)g(\phi_q)^{-1} = h^{(-)}(\hat{u}_q)g(\phi_q)^{-1}J\,. \tag{124}$$

Moreover, by (30) we have $J = e^{(t_2-t_1)A}$ for equilibria, so (124) becomes

$$\hat{A}h^{(-)}(\hat{u}_q)g(\phi_q)^{-1} = h^{(-)}(\hat{u}_q)g(\phi_q)^{-1}A\,, \tag{125}$$

where $\hat{A}$ is the in-slice stability matrix. (125) relates stability matrix in the slice and that in the full state space by a similarity transformation. So

$$\hat{\Lambda}_j = \Lambda_j\,, \quad \hat{\mathbf{e}}_j = h^{(-)}(\hat{u}_q)g(\phi_q)^{-1}\mathbf{e}_j\,. \tag{126}$$

Here, $\hat{\Lambda}_j$ and Λ_j are the stability exponents in the slice and in the full state space respectively. $\hat{\mathbf{e}}$ and $\mathbf{e}$ are the corresponding eigenvectors.

In-slice stability matrix of a relative equilibrium For an relative equilibrium $g(c(t_2-t_1))u(t_2) = u(t_1)$, we also have $\hat{u}(t_1) = \hat{u}(t_2) := \hat{u}_q$ and $\phi_1 = \phi_2 - c(t_2 - t_1)$. Formula (123) reduces to

$$\hat{J}\left(h^{(-)}(\hat{u}_q)g(\phi_1)^{-1}\right) = \left(h^{(-)}(\hat{u}_q)g(\phi_1)^{-1}\right)g(c(t_2-t_1))^{-1}J\,. \tag{127}$$

If let $t_2 - t_1 = \delta t$ be an infinitesimal time lapse. Then

$$J = \mathbf{1} + A\delta t \quad \text{and} \quad g(c(t_2-t_1)) = \mathbf{1} + c\mathbf{T}\delta t$$

are first-order accurate. Thus (127) gives

$$\hat{A}\left(h^{(-)}(\hat{u}_q)g(\phi_1)^{-1}\right) = \left(h^{(-)}(\hat{u}_q)g(\phi_1)^{-1}\right)(-c\mathbf{T} + A)\,. \tag{128}$$

Actually, $-c\mathbf{T} + A$ is the *effective* stability matrix of a relative equilibrium in the full state space, so (128) relates the stability matrix in the slice with the effective stability matrix in the full state space by a similarity transformation. Therefore, their spectra and eigenvectors have the same relation as in (126).

In-slice Jacobian matrix of a periodic orbit For a periodic orbit $u(0) = u(T_p)$, if we set $t_2 = t_1 + T_p$ we have $\hat{u}(t_1) = \hat{u}(t_2) := \hat{u}_p$ and $\phi_1 = \phi_2 := \phi_p$. So, the Floquet matrix has relation $\hat{J}_p h^{(-)}(\hat{u}_p) g(\phi_p)^{-1} = h^{(-)}(\hat{u}_p) g(\phi_p)^{-1} J_p$. Therefore, the Floquet vectors and Floquet multipliers in the slice and those in the full state space have the same relation as in (126).

In-slice Jacobian matrix of a relative periodic orbit For a relative periodic orbit $u(0) = g(\phi_p)u(T_p)$, if we also set $t_2 = t_1 + T_p$ then we have $\hat{u}(t_1) = \hat{u}(t_2) := \hat{u}_p$ and $\phi_1 = \phi_p + \phi_2$. Relation (123) becomes

$$\hat{J} h^{(-)}(\hat{u}_p) g(\phi_1)^{-1} = h^{(-)}(\hat{u}_p) g(\phi_1)^{-1} J_p \,. \tag{129}$$

Here $J_p = g(\phi_p)J$ is the Floquet matrix in the full state space for a relative periodic orbit. So the same as periodic orbits, we have relation (126).

In summary, relation (126) holds for equilibria, relative equilibria, periodic orbits, and relative periodic orbits. The stability spectrum (Floquet spectrum) in the slice is the same as that in the full state space. Eigenvectors (Floquet vectors) in the full state space are first transported to the slice and then projected into the slice. This is the exact reason that using a slice to reduce continuous symmetries not only keeps the dynamical properties unchanged but also simplifies the analysis.

2.2.4 An example: the two-mode system

In this subsection, we use the two-mode system as an example to illustrate the techniques described in the previous two subsections. We follow Chaosbook [22] for the setup of the two-mode system

$$\begin{aligned}
\dot{x}_1 &= (\mu_1 - r^2)\, x_1 + c_1\, (x_1 x_2 + y_1 y_2)\,, \qquad r^2 = x_1^2 + y_1^2 \\
\dot{y}_1 &= (\mu_1 - r^2)\, y_1 + c_1\, (x_1 y_2 - x_2 y_1) \\
\dot{x}_2 &= x_2 + y_2 + x_1^2 - y_1^2 + a_2 x_2 r^2 \\
\dot{y}_2 &= -x_2 + y_2 + 2\, x_1 y_1 + a_2 y_2 r^2 \,.
\end{aligned} \tag{130}$$

and the choice of parameters:

$$\mu_1 = -2.8\,, \quad a_2 = -2.66\,, \quad c_1 = -7.75\,.$$

Full state space points are represented as $u = (x_1, y_1, x_2, y_2)^\top$. The two-mode system (130) has an SO(2) symmetry

$$g(\phi) = \begin{pmatrix} \cos\phi & \sin\phi & 0 & 0 \\ -\sin\phi & \cos\phi & 0 & 0 \\ 0 & 0 & \cos 2\phi & \sin 2\phi \\ 0 & 0 & -\sin 2\phi & \cos 2\phi \end{pmatrix}$$

with the corresponding Lie group generator

$$\mathbf{T} = \begin{pmatrix} 0 & 1 & 0 & 0 \\ -1 & 0 & 0 & 0 \\ 0 & 0 & 0 & 2 \\ 0 & 0 & -2 & 0 \end{pmatrix} . \tag{131}$$

In order to reduce this continuous symmetry, $\hat{u}' = (1,0,0,0)^\top$ is chosen as the template point the same as that in Chaosbook [22], and thus the resulting slice condition is

$$\langle \hat{u} | t' \rangle = 0 \text{ and } \hat{x}_1 > 0 \quad \text{with} \quad t' = (0,-1,0,0)^\top \,.$$

The in-slice state is denoted as $\hat{u} = (\hat{x}_1, 0, \hat{x}_2, \hat{y}_2)^\top$. Symmetry reduction is equivalent to rotating every state into the positive real axis in the (x_1, y_1) plane.

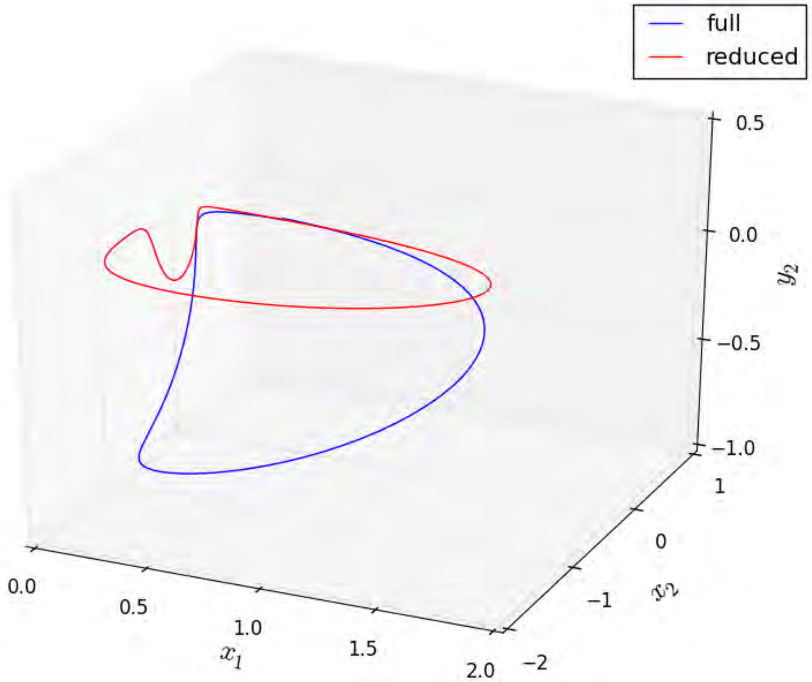

Figure 6: The configuration of $\overline{1}$ in the full state space projected into subspace $[x_1, x_2, y_2]$ (the blue curve) and in the slice (the red curve).

In this subsection, we focus on one relative periodic orbit in the two-mode system whose initial condition is

$$\overline{1}: \quad (0.4525719, \quad 0.0, \quad 0.0509257, \quad 0.0335428)\,. \tag{132}$$

The orbit has period 3.6415. Figure 6 depicts relative periodic orbit $\overline{1}$ in the full state space and in the slice. The Floquet multipliers associated with this orbit are

$$\Lambda_j: \quad (-1.481177, \quad -1.066888 \cdot 10^{-09}, \quad 0.999414, \quad 0.999913)\,. \tag{133}$$

It has a weak expanding direction, a strong contracting direction, and two marginal directions.

The velocity field $v(u)$ and the group tangent $t(u)$ are Floquet vectors of this system and give rise to the two marginal multipliers in (133), but the corresponding two Floquet vectors are degenerate which cannot be told apart when we solving the eigenequation of the Jacobian matrix. However, we can check whether $v(u)$ and $t(u)$ are contained in the subspace spanned by these two Floquet vectors. This is the idea of Figure 7, in which we show the planes spanned by the two marginal Floquet vectors, the velocity field, and the group tangent, along this orbit. As we can see, $v(u)$ and $t(u)$ do lie in the planes.

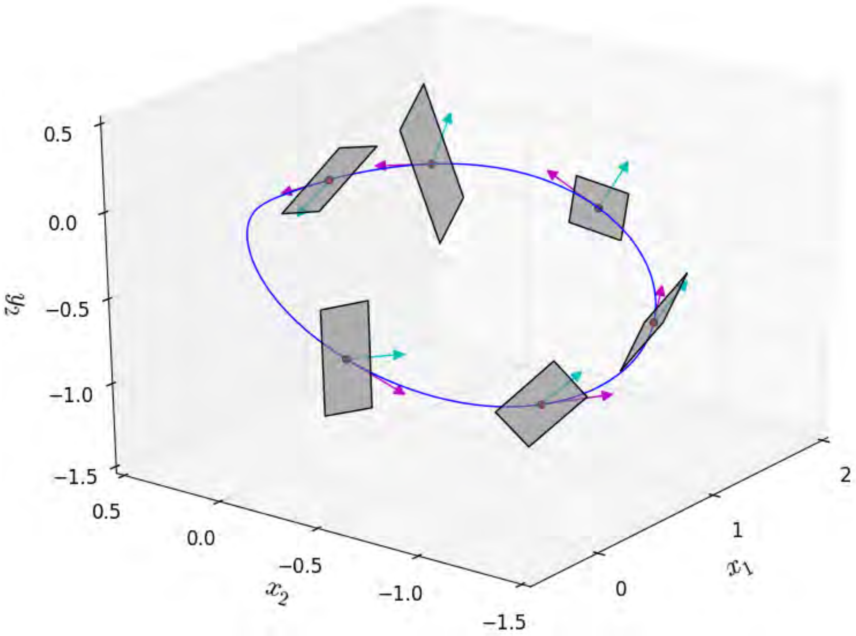

Figure 7: The gray planes are spanned by the two marginal Floquet vectors. of relative periodic orbit $\overline{1}$. The pink, green arrows are the velocity vectors and the group tangents on this orbit respectively. The blue curve is relative periodic orbit $\overline{1}$ projected into the subspace $[x_1, x_2, y_2]$.

Therefore, the calculation of Floquet spectrum and Floquet vectors of $\overline{1}$ is accurate at least for illustration purpose.

Now the task is to transform these Floquet vectors into the slice. By the Lie group generator (131), we get the group tangent of an in-slice point $\hat{u} = (\hat{x}_1, 0, \hat{x}_2, \hat{y}_2)^\top$:

$$t(\hat{u}) = (0, -\hat{x}_1, 2\hat{y}_2, -2\hat{x}_2)\,.$$

Then by (119) we have

$$h(\hat{u}) = \begin{pmatrix} 1 & 0 & 0 & 0 \\ 0 & 0 & 0 & 0 \\ 0 & 2\hat{y}_1/\hat{x}_1 & 1 & 0 \\ 0 & -2\hat{x}_2/\hat{x}_1 & 0 & 1 \end{pmatrix}\,.$$

We choose to eliminate the second coordinate $\hat{y}_1$, then

$$h^{(-)}(\hat{u}) = \begin{pmatrix} 1 & 0 & 0 & 0 \\ 0 & 2\hat{y}_1/\hat{x}_1 & 1 & 0 \\ 0 & -2\hat{x}_2/\hat{x}_1 & 0 & 1 \end{pmatrix}\,.$$

Matrix $h^{(-)}(\hat{u})$ transforms Floquet vectors in the full state space into the slice which are shown in Figure 8. The group tangent $t(\hat{u})$, as one marginal vector, disappears and the planes in Figure 7 collapse to the velocity field along the orbit shown in Figure 8(a). The other two projected Floquet vectors are shown in Figure 8(b).

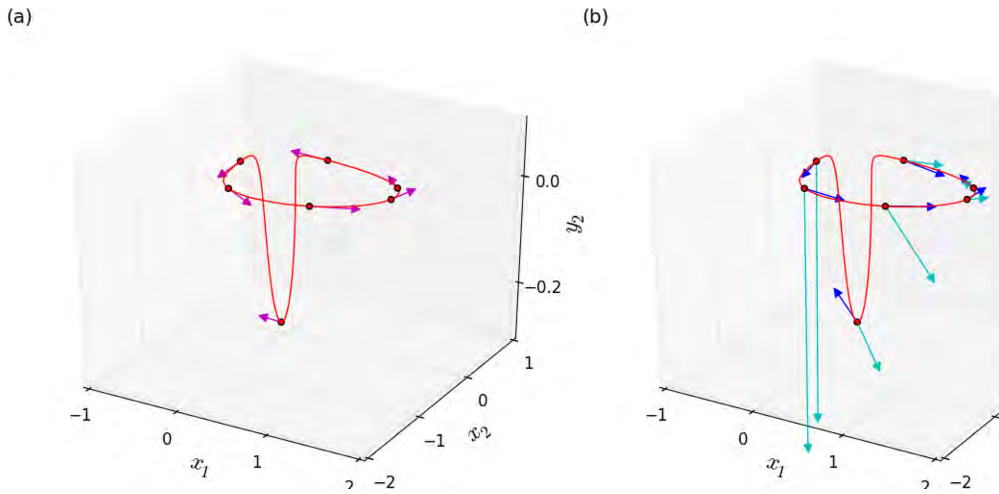

Figure 8: In-slice Floquet vectors for relative periodic orbit $\overline{1}$. The red closed curve is $\overline{1}$. (a) The marginal Floquet vector (pink). (b) The expanding (blue) and contracting (green) Floquet vectors in the slice.

In a similar way [22], Floquet vectors on the slice could be projected onto a Poincaré section. The projection matrix is

$$h_{\mathcal{P}}(\hat{u}) = \mathbf{1} - \frac{|\hat{v}\rangle\langle\partial U|}{\langle\hat{v}|\partial U\rangle} \,,$$

where $U(x) = 0$ defines the Poincaré section with ∂U its normal direction. $\hat{v}$ is the in-slice velocity. A Poincaré section can be fixed by choosing three points on it, or equivalently, by three conditions. Here, we choose a "vertical" Poincaré section, namely, we demand that the $\hat{y}_2$ component of its normal direction vanishes. Next, this Poincaré section goes through the origin $(0, 0, 0)$ and a relative equilibrium

$$(\hat{x}_{e1}, \hat{x}_{e2}, \hat{y}_{e2}) = (0.439965, \quad -0.386267, \quad 0.070204) \,,$$

shown in Figure 9. In this case, $\partial U = (\hat{x}_{e2}, -\hat{x}_{e1}, 0)$ and we get

$$h_{\mathcal{P}}(\hat{u}) = \frac{1}{\hat{v}_1\hat{x}_{e2} - \hat{v}_2\hat{x}_{e1}} \begin{pmatrix} -\hat{v}_2\hat{x}_{e1} & \hat{v}_1\hat{x}_{e1} & 0 \\ -\hat{v}_2\hat{x}_{e2} & \hat{v}_1\hat{x}_{e2} & 0 \\ -\hat{v}_3\hat{x}_{e1} & \hat{v}_3\hat{x}_{e1} & \hat{v}_1\hat{x}_{e2} - \hat{v}_2\hat{x}_{e1} \end{pmatrix} .$$

Figure 9 shows the projected expanding and contracting Floquet vectors on the Poincaré section. The marginal vector (velocity field) disappears.

Last, Figure 10 shows the Poincaré section and the two projected Floquet vectors. A set of circularly distributed points around the intersection point evolves for one period and their first returning points are recorded. The contracting direction is close to the vertical direction, and (133) says that the contracting rate is large in this direction. Therefore, the returning points are squashed heavily in the vertical direction; however, the magnitude of expanding multiplier is about 1.5, so the elongation in the horizontal direction is relatively small.

In summary, we have reduced the SO(2) symmetry of the two-mode system and discussed the Floquet vectors of a specific relative periodic orbit in the full state space and in the

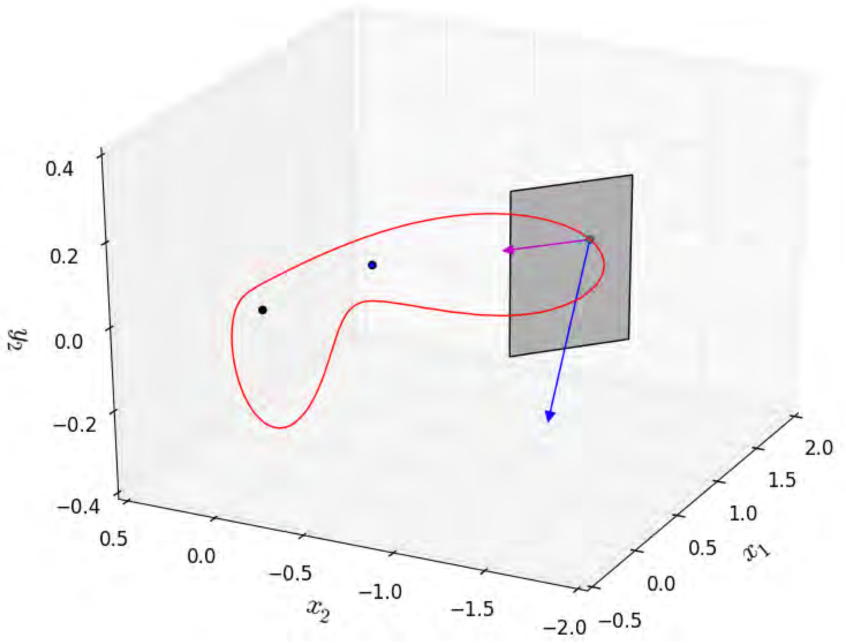

Figure 9: A vertical Poincaré section is constructed from the origin (black point) and a relative equilibrium (blue point) in the slice. The Poincaré section intersects $\overline{1}$ (the red closed curve) at the green point. In-slice Floquet vectors are projected into the Poincaré section. The red/blue vector is the expanding/contracting Floquet vector. The marginal vector along the orbit disappears on the Poincaré section.

slice. The marginal direction along the group orbit tangent is eliminated by the slice. Furthermore, we have constructed a Poincaré section of codimension two with respect to the original system. In this Poincaré section, the relative periodic orbit $\overline{1}$ is reduced to a fixed point with one expanding and one contracting Floquet vector, and the dynamics is greatly simplified. This simple example illustrates why symmetry reduction is an indispensable tool when studying dynamical systems with continuous symmetries.

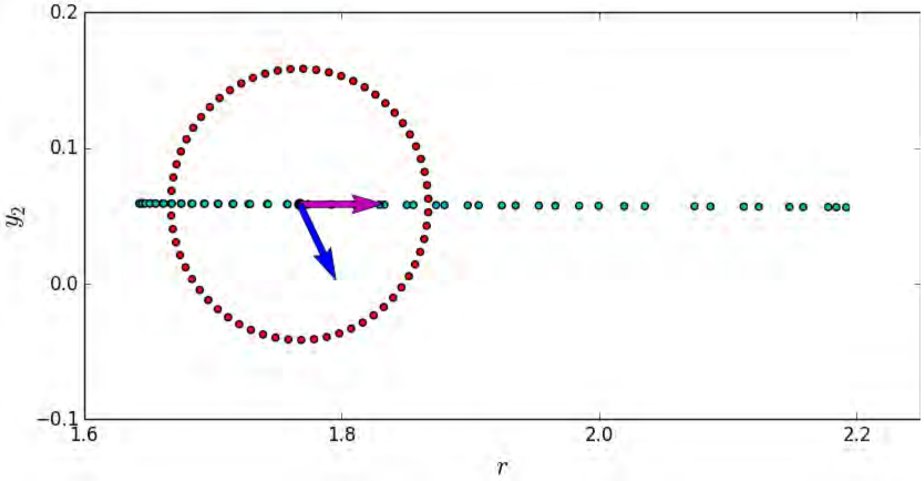

Figure 10: A set of circularly (radis=0.1) distributed points (red) around the intersection point evolves for one period. Their first returning points (green) are recorded. The pink and blue arrows are the expanding and contracting Floquet vectors projected onto the Poincaré section respectively. Here $r = (\hat{x}_1^2 + \hat{x}_2^2)^{1/2}$.

CHAPTER III

KURAMOTO-SIVASHINSKY EQUATION

Kuramoto-Sivashinsky equation is one of the most studied models of complex spatiotemporal dynamics in spatially extended systems. It was formulated independently by Kuramoto in the context of angular phase turbulence in reaction-diffusion systems [55], and by Sivashinsky in the study of hydrodynamic instability of laminar flames [63]. It also describes the instabilities of dissipative trapped ion modes in plasmas [58] and the flow of a viscous liquid film down a vertical wall [75]. Its one-dimensional form is frequently written as

$$u_t + \frac{1}{2}(u^2)_x + u_{xx} + u_{xxxx} = 0\,,\ x \in [0, L] \tag{134}$$

defined on a periodic domain $u(x,t) = u(x+L,t)$. In the combustion formulation, $u(x,t)$ represents the flame front velocity. Everyday experience tells us that a candle flame flickers and its shape changes quite often, without any exterior influence. Therefore, Kuramoto-Sivashinsky equation is expected to exhibit chaotic behaviors. Figure 11 displays its spatiotemporal profiles with domain size $L = 100$ and 200 respectively. Recurrent patterns appear not only along the temporal axis but also along the spatial axis. This spatiotemporal chaotic behavior is also observed in other spatially-extended dynamical systems such as complex Ginzburg-Landau equation [76]. At the same time, Figure 11 provides coarse information about the time and length scale of this "dimensionless" system. In all our simulations, we set $L = 22$, which is large enough to exhibit complex spatiotemporal chaotic dynamics [21].

3.1 Numerical setup

Periodic boundary condition enables us to transform (134) into a set of ODEs in the Fourier space

$$\dot{a}_k \quad = (q_k^2 - q_k^4)\, a_k - i\frac{q_k}{2} \sum_{m=-\infty}^{\infty} a_m a_{k-m} \tag{135}$$

where $q_k = 2\pi k/L$ and the coefficients are complex,

$$a_k = b_k + i c_k\,.$$

Pseudo-spectral method [83] is deployed to evaluate terms in (135). That is, the linear term is calculated in the Fourier space; while the nonlinear term is first transformed to the physical space, calculated there and then transformed back to the Fourier space. In our simulations, discrete Fourier transform is used with $N = 64$ modes, i.e., $k = -N/2 + 1$ up to $N/2$ in (135).

Since $u(x,t)$ is real, $a_k(t) = a^*_{-k}(t)$; thus, only half of the Fourier modes are independent. As $\dot{a}_0 = 0$ from (135), we can set $a_0 = 0$ corresponding to zero mean velocity without loss of generality. Also, the nonlinear term of $\dot{a}_{N/2}$, in fact, has coefficient $-i(q_{N/2} + q_{-N/2})/2 = 0$ from symmetric consideration [83]; thus, $a_{N/2}$ is decoupled from other modes and it can be set to zero as well. Therefore, the number of independent variables is $N - 2$,

$$\tilde{u} = (b_1, c_1, b_2, c_2, \cdots, b_{N/2-1}, c_{N/2-1})^\top\,. \tag{136}$$

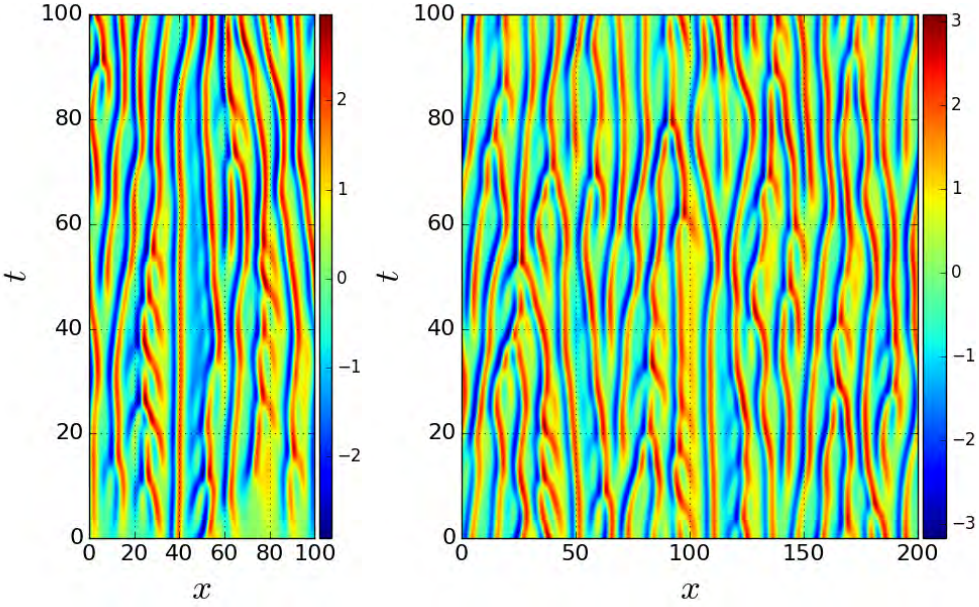

Figure 11: Simulations of the one-dimensional Kuramoto-Sivashinsky equation for domain size $L = 100, 200$ respectively with random initial conditions. The color represents the magnitude of $u(x, t)$.

This is the full state space in the discussion that follows.

The stiffness caused by the quaternary term in the linear part makes popular integration methods such as fourth order Runge-Kutta inefficient in this case. Therefore, we resort to exponential integrators [48, 64] to integrate the linear part exactly. In our simulations, exponential time-differencing scheme combined with fourth order Runge-Kutta [19, 52] is implemented to integrate (135). By this scheme, a relatively large time step can be used to achieve a fourth-order global accuracy.

3.2 Symmetries

The one-dimensional Kuramoto-Sivashinsky equation has three different symmetries. Suppose $u(x, t)$ is an orbit in this system, then we have

- *Galilean invariance*: $u(x - ct, t) + c$ is also a valid orbit, where c is a constant number. These two orbits have different mean velocity $\int dx\, u$.
- *Reflection invariance*: $-u(-x, t)$ is also a valid orbit. In the Fourier mode space, reflection takes form $a_k \to -a_k^*$.
- *Translation invariance*: $u(x + \ell, t)$ is another valid orbit. In the Fourier mode space, translation takes form $a_k \to e^{iq_k\phi} a_k$ with $\phi = 2\pi\ell/L$.

The zeroth Fourier mode a_0 represents the mean velocity of $u(x, t)$. by setting $a_0 = 0$ in the integrator, we eliminate the Galilean symmetry. Therefore, we only need to account for the O(2) symmetry of this system. Reflection in state space (136) takes the form

$$R = \mathrm{Diag}(-1,\, 1,\, -1,\, 1, \cdots)\,.$$

The translation symmetry corresponds to an one-parameter SO(2) group in the state space,

$$g(\phi) = \mathrm{Diag}(r_1, r_2, \cdots, r_{N/2-1})$$

with

$$r_k = \begin{pmatrix} \cos k\phi & \sin k\phi \\ -\sin k\phi & \cos k\phi \end{pmatrix} .$$

The corresponding Lie group generator is

$$\mathbf{T} = \mathrm{Diag}(t_1, t_2, \cdots, t_{N/2-1}), \quad t_k = \begin{pmatrix} 0 & k \\ -k & 0 \end{pmatrix} .$$

Based on the consideration of these symmetries, there are three types of invariant orbits in Kuramoto-Sivashinsky system: periodic orbits in the $b_k = 0$ invariant antisymmetric subspace, preperiodic orbits which are self-dual under reflection, and relative periodic orbits with a shift along group orbit after one period. As claimed in ref. [21], the first type is absent for a domain as small as $L = 22$, and thus we focus on the last two types of orbits.

- For preperiodic orbits $\tilde{u}(0) = R\tilde{u}(T_p)$, we only need to evolve the system for a prime period T_p which is half of the whole period. The Floquet matrix is $J_p(\tilde{u}) = RJ^{T_p}(\tilde{u})$.
- A relative periodic orbit, $\tilde{u}(0) = g_p\tilde{u}(T_p)$, returns after one period T_p to the initial state upon the group transform $g_p = g(\phi_p)$, so the corresponding Floquet matrix is $J_p(\tilde{u}) = g_p J^{T_p}(\tilde{u})$.

In later sections, we calculate the stability of both preperiodic orbits and relative periodic orbits. We anticipate that there are two marginal directions for both types of orbits. One marginal direction corresponds to the velocity field and the other one is the group tangent, which is proved in Example 3.1.

Example 3.1 **$v(\tilde{u})$ and $t(\tilde{u})$ are the two marginal directions of both preperiodic orbits and relative periodic orbits** *The Jacobian matrix transports both velocity field and group tangent along the flow $J^{T_p}v(\tilde{u}(0)) = v(\tilde{u}(T_p))$, $J^{T_p}t(\tilde{u}(0)) = t(\tilde{u}(T_p))$. Therefore, for preperiodic orbits, we have $J_p v(\tilde{u}(0)) = Rv(\tilde{u}(T_p)) = Rv(R\tilde{u}(0))$. Here, we have used the definition of a preperiodic orbit and the form of its Floquet matrix. By use of the equivariance relation of the velocity field under reflection $v(R\tilde{u}(0)) = Rv(\tilde{u}(0))$, we get*

$$J_p v(\tilde{u}(0)) = R \cdot Rv(\tilde{u}(0)) = v(\tilde{u}(0)) .$$

So, we see that the velocity field is one marginal direction of preperiodic orbits with Floquet multiplier 1. Similarly, for the group tangent we have $J_p t(\tilde{u}(0)) = Rt(R\tilde{u}(0)) = R \cdot \mathbf{T} \cdot R\tilde{u}(0)$ following definition (104). Since reflection anti-commutes with rotation $R\mathbf{T} + \mathbf{T}R = 0$, then we have

$$J_p t(\tilde{u}(0)) = -\mathbf{T} \cdot R \cdot R\tilde{u}(0) = -t(\tilde{u}(0)) .$$

Therefore, the group tangent is also a marginal direction of preperiodic orbits but with Floquet multiplier -1. A group tangent reverses direction after one period for preperiodic orbits.

For relative periodic orbits, by a similar process we have

$$J_p v(\tilde{u}(0)) = g_p v(g_p^{-1}\tilde{u}(0)) = v(\tilde{u}(0))$$

and

$$J_p t(\tilde{u}(0)) = g_p t(g_p^{-1}\tilde{u}(0)) = t(\tilde{u}(0)) .$$

So, the velocity field $v(\tilde{u})$ and the group tangent $t(\tilde{u})$ are two degenerate Floquet vectors for relative periodic orbits, but not degenerate for preperiodic orbits.

In order to reduce O(2) symmetry, we can choose to reduce reflection symmetry first and then translation symmetry, or vice versa. Note that reflection does not commute with translation $Rg(\phi) = g(-\phi)R$, so the result of symmetry reduction depends on the order we choose. In this section, we elect to quotient out the SO(2) symmetry by the technique described in Sect. 2.2, more precisely, by the 1st mode slice [14] defined by

$$c_1 = 0,\, b_1 > 0\,. \tag{137}$$

This corresponds to choosing $\hat{u}' = (1, 0, \cdots, 0)$ as the template point in (107). The reduced state space is denoted as

$$\hat{u} = (\hat{b}_1, \hat{b}_2, \hat{c}_2, \cdots, \hat{b}_{N/2-1}, \hat{c}_{N/2-1})^\top\,. \tag{138}$$

Here, $\hat{c}_1 = 0$ is omitted explicitly. We can rotate orbits in the full state space to the SO(2)-reduced state space by transformation $a_k \to e^{-ik\phi_1}a_k$ where ϕ_1 is the phase of the first Fourier mode. Alternatively, we can choose to integrate the system directly in the slice. For a reduced state space point (138), which is a $(N-3)$-element vector, the corresponding group tangent in the full state space is $t(\hat{u}) = (0, -\hat{b}_1, 2\hat{c}_2, -2\hat{b}_2, \cdots, (N/2-1)\hat{c}_{N/2-1}, -(N/2-1)\hat{b}_{N/2-1})^\top$. The template point is $\hat{u}' = (1, 0, \cdots, 0)$; then the corresponding group tangent is $t' = (0, -1, 0, \cdots, 0)$. From (115) we get the dynamics in the slice

$$\hat{v}(\hat{u}) = v(\hat{u}) \;-\; \dot{\phi}(\hat{u})t(\hat{u})\,, \quad \dot{\phi}(\hat{u}) = \frac{-\mathrm{Im}\,[v_1(\hat{u})]}{\hat{b}_1}\,.$$

When an in-slice orbit gets close to the slice border $\hat{b}_1 = 0$, the trajectory can attain arbitrarily high speed. To alleviate this numerical difficulty, we rescale the time step by $dt = \hat{b}_1 d\tau$. Thus the time-rescaled dynamics in the slice is

$$\frac{d\hat{u}}{d\tau} = \hat{b}_1 v(\hat{u}) + \mathtt{Im}[v_1(\hat{u})]t(\hat{u})\,. \tag{139}$$

3.3 Invariant solutions

Invariant structures, together with their stable and unstable manifolds, shape the geometrical structure of the state space. We also anticipate that spatiotemporal averages can be calculated by periodic orbits, as discussed in Sect. 1.4.2. Since invariant structures play such an important role in chaotic systems, we now discuss them in the one-dimensional Kuramoto-Sivashinsky equation with $L = 22$. These include equilibria, relative equilibria, preperiodic orbits, and relative periodic orbits, whose definitions can be found in Sect. 2.2.1.

3.3.1 Equilibria and relative equilibria

There are only three equilibria and two relative equilibria for domain size $L = 22$ [21]. They can be obtained by Newton-based numerical search such as the Levenberg-Marquardt algorithm [59, 62] even with random initial inputs.

Figure 12 shows the profiles of these three equilibria. E_1 is in the anti-symmetric subspace $u(x,t) = -u(-x,t)$. E_2 and E_3 are period-2 and period-3 harmonic solutions. Since $a_1 = 0$, E_2 and E_3 are in the slice border.

Figure 13 shows the profiles of the two relative equilibria. Their time-evolution profiles are shown in Figure 14(a)(c). The color of the heat map represents $u(x,t)$. Both of them

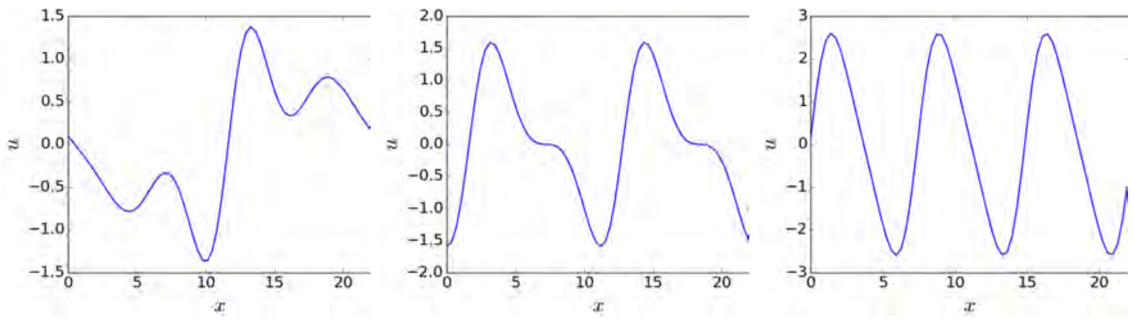

Figure 12: Three equilibria E_1, E_2, and E_3 from left to right in the one-dimensional Kuramoto-Sivashinsky equation.

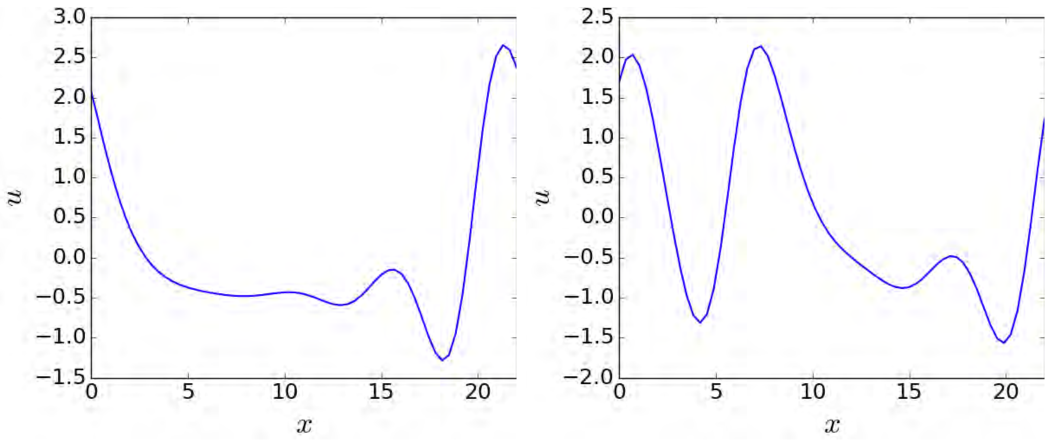

Figure 13: Two relative equilibria TW_1 (left) and TW_2 (right) in the one-dimensional Kuramoto-Sivashinsky equation.

have constant spatial translation velocity. That is why they are also called *traveling waves*. The in-slice trajectories are shown in Figure 14(b)(d), in which translation symmetry has been reduced. Note, TW_2 fails to maintain its profile after $t = 80$ due to its instability. For the stability exponents of these three equilibria and two relative equilibria, please see [21].

3.3.2 Preperiodic orbits and relative periodic orbits

Using a multishooting method, over 60 000 preperiodic orbits and relative periodic orbits [21] are found with periods ranging from 10.25 to 200. All of them have either one or two unstable directions. Let $\overline{ppo}_T$ and $\overline{rpo}_T$ denote the preperiodic orbit and relative periodic orbit with period T respectively. Figure 15 shows the shortest three preperiodic orbits and shortest three relative periodic orbits. A preperiodic orbit reflects itself after one prime period, so it is truly periodic after two prime periods. While a relative periodic orbit has a specific spatial translation after each period. Figure 16 shows the corresponding in-slice orbits. Since translation symmetry has been reduced, relative periodic orbits become periodic in the slice. Note, some of them undergo quick twists at certain times. This is because we are using a post-processing method to transform orbits in the full state space to the slice; therefore, when an orbit gets close to the slice border, the rotation phase jumps sharply. If we integrate the system directly in the slice by (139), then time will dilate when an orbit

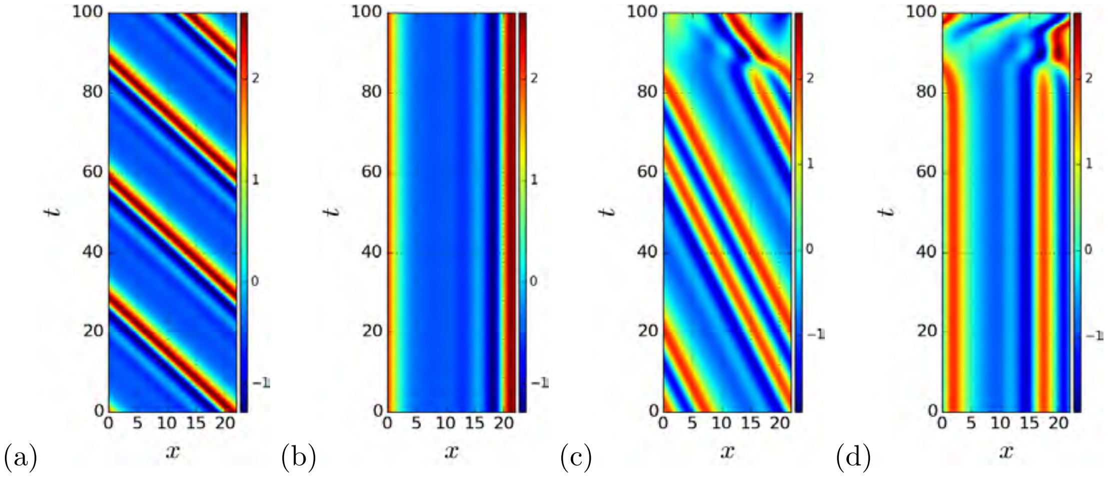

Figure 14: (a)(c) TW_1 and TW_2 in the full state space. (b)(d) TW_1 and TW_2 in the slice.

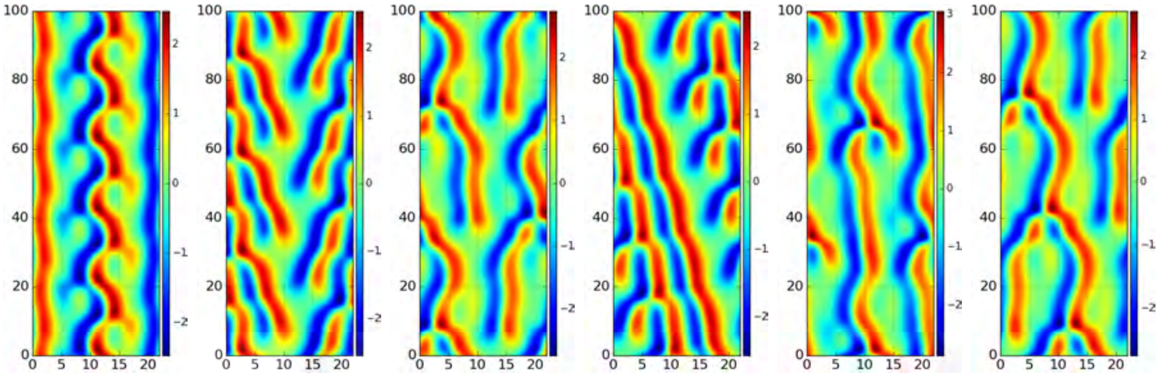

Figure 15: The shortest three preperiodic orbits and three relative periodic orbits in the full state space. Left three: $\overline{ppo}_{10.25}$, $\overline{ppo}_{14.33}$ and $\overline{ppo}_{32.36}$. Right three: $\overline{rpo}_{16.31}$, $\overline{rpo}_{32.80}$ and $\overline{rpo}_{33.50}$.

gets close to the slice border.

This set of preperodic or relative periodic orbits forms the backbone of the global attractor. An ergodic trajectory shadows one orbit for a certain period and then is repelled to the neighborhood of another orbit. This random walk is determined by the stability of the preperodic and relative periodic orbits. Table 7 gives the Floquet exponents of the six orbits in Figure 15, which are obtained by periodic eigendecomposition algorithm that will be covered in Chapter 5. There are a few observations. First, all orbits have one or two unstable directions and are weakly unstable. $\overline{ppo}_{14.33}$ and $\overline{rpo}_{16.31}$ are the two most unstable orbits in our database. Second, all orbits have two marginal directions. For preperiodic orbits, one marginal direction has inverse hyperbolicity, i.e., one Floquet multiplier is equal to -1. This was proved in Example 3.1. Third, the leading 8 Floquet exponents vary sharply among different orbits, but the remaining spectrum is similar. More precisely, for large index k, the real parts of Floquet exponents lie on the curve $(q_k^2 - q_k^4)$ as shown in Figure 17 for $\overline{ppo}_{10.25}$. This means that the nonlinear term in (135) is almost negligible for higher Fourier modes, and thus they are decoupled from other modes and shrink exponentially with rate $|q_k^2 - q_k^4|$. Also, Floquet exponents appear in pairs for large indices

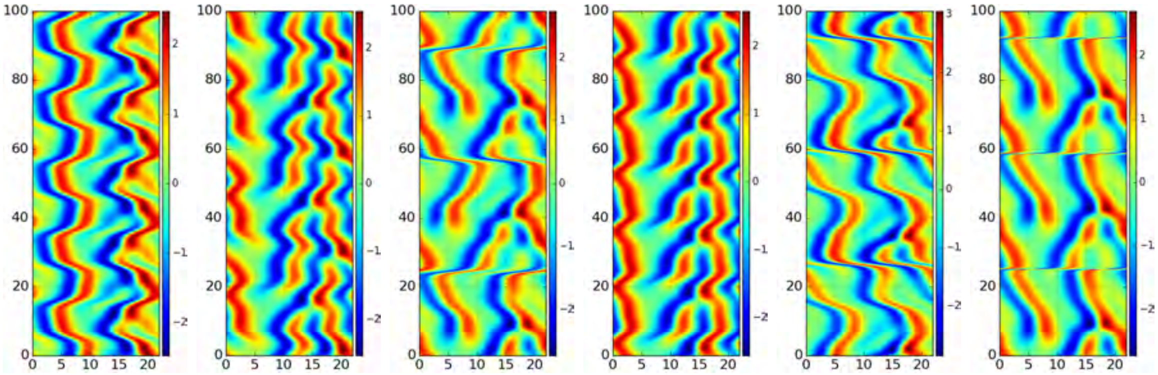

Figure 16: Orbits of Figure 15 in the slice.

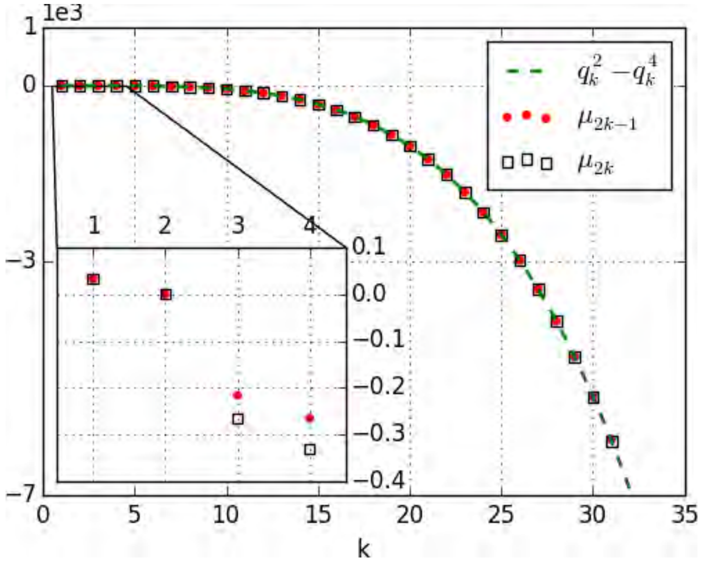

Figure 17: The real parts of the Floquet exponents paired for a given k as $(k, \mu^{(2k-1)})$ and $(k, \mu^{(2k)})$ for $\overline{ppo}_{10.25}$. The dashed line (green) is $q_k^2 - q_k^4$ with $q_k = 2\pi k/L$. The inset is a magnification of the region containing the 8 leading exponents.

simply because the real and complex part of high Fourier modes have a similar contraction rate. From these observations, we gain an intuition of how many directions are important in shaping the neighborhood of a pre/relative periodic orbit.

3.4 Floquet vectors

Floquet vectors are important for shaping the geometrical structure of the global attractor in a dissipative system. Floquet vectors of a pre/relative periodic orbit stratify the neighborhood of this orbit. They give a rough picture of the dynamics close to this orbit. On the other hand, the stable and unstable manifolds of this orbit are tangent to the Floquet vectors, so numerically we grow the unstable manifolds from unstable Floquet vectors. Thus, Floquet vectors provide a way of studying the dynamics far away from this orbit. Calculating Floquet vectors is not an easy task due to the large range of orders of expansion/contraction rates indicated by Table 7. However, with the invention of periodic

Table 7: The first 10 and last four Floquet multipliers $\Lambda_i = \exp(T\mu^{(i)} \pm i\theta_i)$ for six representative orbits. θ_i column lists either the phase, if the Floquet multiplier is complex, or '-1' if the multiplier is real, but inverse hyperbolic.

$\overline{ppo}_{10.25}$			$\overline{ppo}_{14.33}$			$\overline{ppo}_{32.36}$		
i	$\mu^{(i)}$	θ_i	i	$\mu^{(i)}$	θ_i	i	$\mu^{(i)}$	θ_i
1,2	0.033209	±2.0079	1	0.31095	-1	1,2	0.064755	±1.9790
3	-4.1096e-13		2	-1.7825e-12		3	-6.3772e-14	
4	-3.3524e-14	-1	3	2.5049e-13	-1	4	1.9306e-13	-1
5	-0.21637		4	-0.12154	-1	5	-0.17511	
6,7	-0.26524	±2.6205	5	-0.20150		6	-0.24418	1
8	-0.33073	-1	6	-0.29265	-1	7,8	-0.27968	±0.6990
9	-1.9605		7,8	-0.34313	±1.7872	9	-1.9868	-1
10	-1.9676	-1	9	-1.9530	-1	10	-1.9891	
			10	-1.9928				
	...			...			...	
59	-5313.6	-1	59	-5312.7	-1	59	-5313.3	-1
60	-5317.6		60	-5318.4		60	-5317.9	
61	-6051.8	-1	61	-6057.8		61	-6052.9	
62	-6080.4		62	-6074.4	-1	62	-6079.2	-1

$\overline{rpo}_{16.31}$			$\overline{rpo}_{32.80}$			$\overline{rpo}_{33.50}$		
i	$\mu^{(i)}$	θ_i	i	$\mu^{(i)}$	θ_i	i	$\mu^{(i)}$	θ_i
1	0.32791		1,2	0.018610	±1.397964	1	0.073049	
2	2.8679e-12		3	6.1717e-14		2	0.015160	-1
3	2.3559e-13		4	-5.7430e-14		3	1.1725e-14	
4	-0.13214	-1	5	-0.19688	-1	4	-8.8541e-14	
5,6	-0.28597	±2.7724	6	-0.24726	-1	5	-0.11390	-1
7	-0.32821	-1	7,8	-0.30869	±2.20628	6	-0.25224	
8	-0.36241		9	-1.9660	-1	7,8	-0.26398	±1.0521
9,10	-1.9617	±2.2411	10	-1.9575	-1	9,10	-1.993196	±0.60493
	...			...			...	
59	-5314.4		59	-5313.9		59	-5313.2	-1
60	-5317.7		60	-5317.2		60	-5318.0	-1
61	-6059.2		61	-6053.9	-1	61	-6052.5	
62	-6072.9		62	-6078.3	-1	62	-6079.7	

eigendecomposition algorithm (Chapter 5), we are able to get a full set of Floquet vectors at each point of a pre/relative periodic orbit.

Figure 18 shows the real part of the 1st Floquet vector, the 5th, the 10th and 30th Floquet vectors of $\overline{ppo}_{10.25}$. As index increases, Floquet vectors behave more like pure Fourier modes. Figure 19 shows a few selected Floquet vectors along $\overline{ppo}_{10.25}$ and $\overline{rpo}_{16.13}$ for one prime period respectively. We can see that the spatiotemporal plots of the few leading Fv s, see panels (a,b) and (e,f), exhibit turbulent structures containing only long waves, for both $\overline{ppo}_{10.25}$ and $\overline{rpo}_{16.13}$, but for Floquet vectors corresponding to strong contraction rates, i.e., panels (c,d), (g,h), the configurations are almost pure sinusoidal curves. The power spectra in Figure 20 demonstrate this point too. The leading 8 Floquet vectors have large components in the first 5 Fourier modes and the spectra are entangled with each

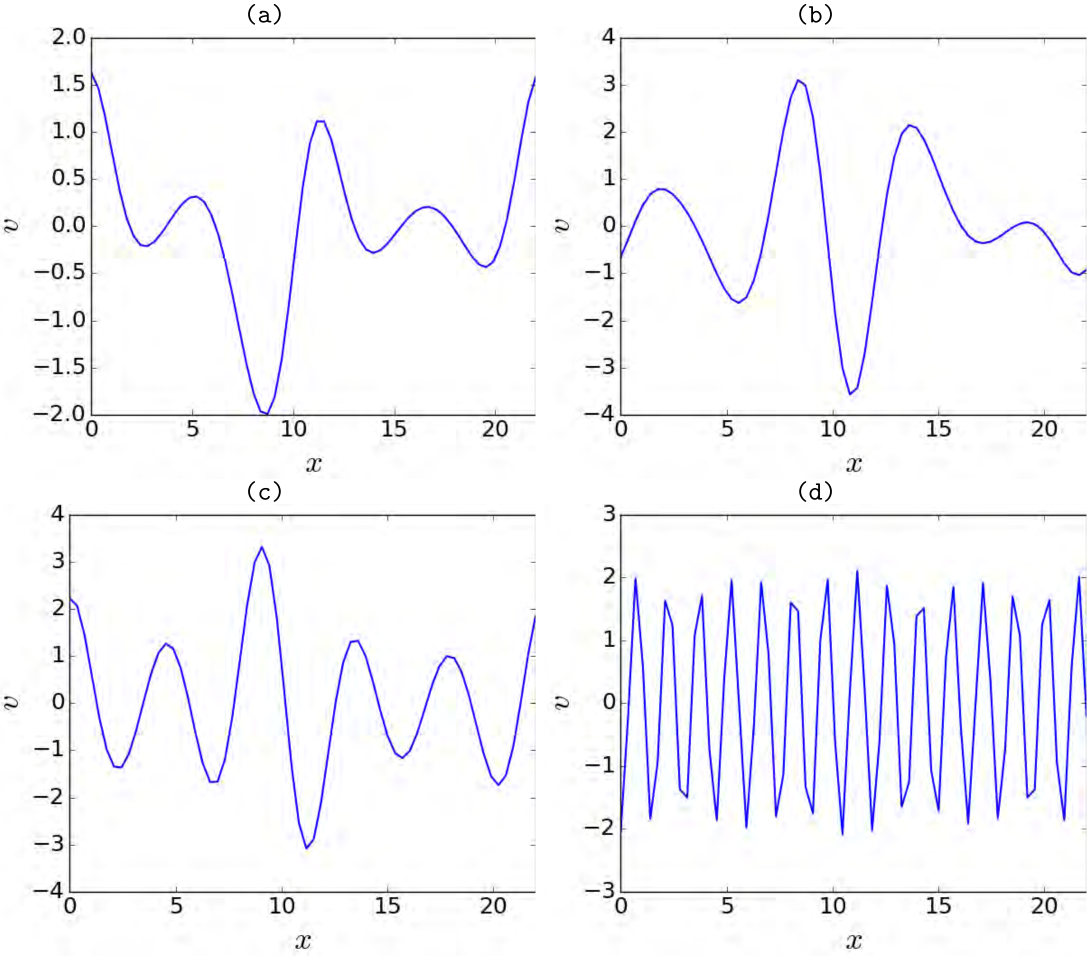

Figure 18: Floquet vectors of $\overline{ppo}_{10.25}$ at $t = 0$ in Figure 15. (a) is the real part of the 1st Floquet vector. (b), (c) and (d) are the 5th, 10th, and 30th Floquet vectors.

other; while the remaining Floquet vectors almost concentrate on a single Fourier mode and are decoupled from each other; more specifically, the ith Floquet vector with $i \geq 9$ peaks at the $\lceil \frac{i}{2} \rceil$th[1] mode in Figure 20. Takeuchi *et al.* [79, 90] observe similar features in covariant vectors along ergodic trajectories and by measuring the tangency between these two groups of covariant vectors, they reach a reasonable conclusion about the dimension of the inertial manifold in Kuramoto-Sivashinsky equation and complex Ginzburg-Landau equation. Therefore, we anticipate that analyzing the tangency of Floquet vectors along different pre/relative periodic orbits can also lead to the same conclusion, which will be discussed in detail in Chapter 4.

3.5 Unstable manifolds and shadowing

Unstable manifolds of the three equilibria and the two relative equilibria, and their connecting orbits in the full state space have been discussed in detail in [21]. With the advance in the technique of symmetry reduction, we have a better picture of the in-slice state space. Moreover, relative periodic orbits become periodic in the slice, which helps us organize the

---

[1] Here, $\lceil x \rceil$ denotes the smallest integer no less than x.

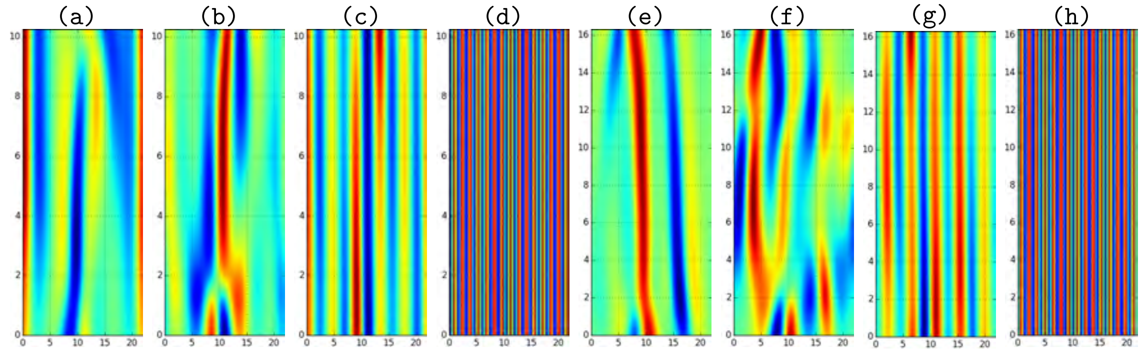

Figure 19: (a) ∼ (d) : the 1st (real part), 5th, 10th and 30th Floquet vector along $\overline{ppo}_{10.25}$ for one prime period. (e) ∼ (h) : the 1st, 4th (real part), 10th (imaginary part) 30th (imaginary part) Floquet vector along $\overline{rpo}_{16.31}$ for one prime period. Axes and color scale are the same as Figure 15.

pre/relative periodic orbits in our database. In this section, we will discuss the unstable manifolds of (relative) equilibria and show shadowing incidences of different orbits.

3.5.1 O(2) symmetry reduction

Sect. 3.2 introduces the 1st mode slice to reduce SO(2) in the one-dimensional Kuramoto-Sivashinsky equation. Here, we go one step further, i.e., quotienting out reflection symmetry in the 1st mode slice. Different from the invariant polynomial approach used by N. B. Budanur [11, 12], we turn to the fundamental domain.

In Sect. 3.2, the 1st mode slice (137) is defined as the half hyperplane $c_1 = 0$, i.e., the imaginary part of the 1st mode vanishes. Here, when reducing reflection in the slice, we find it is more convenient to define the slice as

$$b_1 = 0,\ c_1 > 0\,, \tag{140}$$

namely, we let the real part of the 1st mode vanish. Literature [14, 27] all chooses (137). That is why we insist on using (137) to define the 1st mode slice in other chapters of this thesis. Thus conversion (140) is only used in this section. The benefit of using (140) instead of (137) in this section is that the reflection axis is parallel to the slice (140) such that the reflection rule does not change from the full state space to the slice.

Example 3.2 Reflection rule is invariant under $SO(2)$ reduction by (140) *Suppose two states u_1 and u_2 in the full state space are related to each other by reflection, $u_2 = Ru_1$. Let $\hat{u}_1$ and $\hat{u}_2$ be their reduced states in the slice (140). If the 1st Fourier mode of u_1 is $(b_1 + ic_1)$, then the 1st Fourier mode of u_2 is $(-b_1 + ic_1)$. So if $g(\phi_1)$ transforms u_1 onto the positive imaginary axis in (b_1, c_1) plane, that is, $\hat{u}_1 = g(\phi_1)u_1$, then $\hat{u}_2 = g(-\phi_1)u_2$ as shown in Figure 21. Therefore,*

$$\hat{u}_2 = g(-\phi_1)Ru_1 = Rg(\phi_1)u_1 = R\hat{u}_1\,.$$

Here we have used the anti-commuting relation $g(-\phi)R = Rg(\phi)$. So we see that the choice of slice (140) keeps the reflection rule unchanged.

The reflection operator is $R = \mathrm{Diag}(-1,\ 1,\ -1,\ 1, \cdots)$. Since $\hat{b}_1 = 0$ in the slice, thus $\hat{b}_k$ with $k > 1$ changes sign after reflection. We define the fundamental domain in the slice as

$$\hat{b}_2 > 0\,. \tag{141}$$

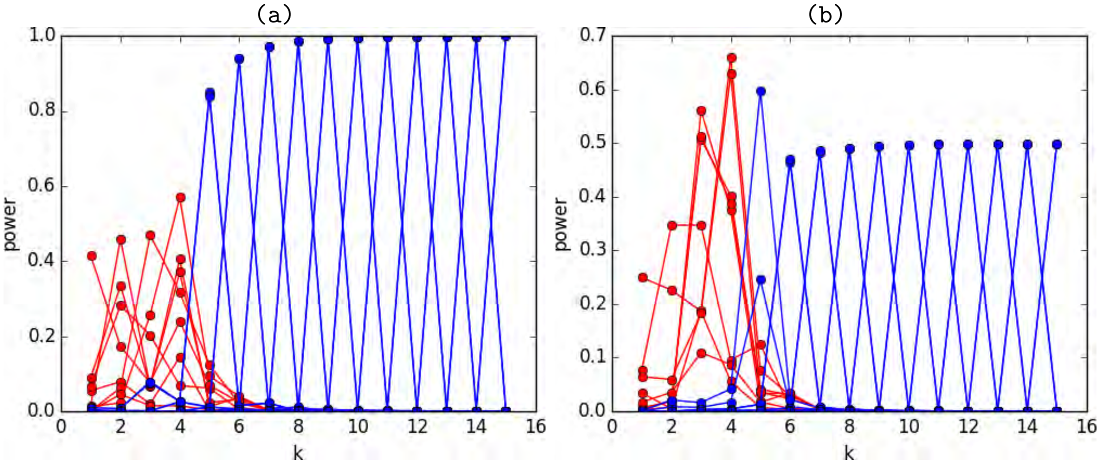

Figure 20: The power spectrum of the first 30 Floquet vectors for $\overline{ppo}_{10.25}$ (left) and $\overline{rpo}_{16.31}$ (right) at $t = 0$. Red lines correspond to the leading 8 Floquet vectors; while the blue lines correspond to the left 22 Floquet vectors with the ith one localized at index $\lceil \frac{i}{2} \rceil$. Power at index k is defined to be the square of the k_{th} Fourier coefficient's magnitude of Floquet vectors. The x-axis is labeled by the Fourier mode indices. Only the $k > 0$ part is shown, and the part for negative k follows by reflection. For complex Floquet vectors, the power spectra of the real part and imaginary part are calculated separately. Since almost all contracting Floquet vectors of $\overline{rpo}_{16.31}$ form complex conjugate pairs, their power peaks are far less than 1, as shown in panel (b).

Whenever an in-slice orbit leaves the fundamental domain, we transform it back by reflection. With the sacrifice of allowing discontinuity, we quotient out O(2) symmetry in the one-dimensional Kuramoto-Sivashinsky equation.

3.5.2 Unstable manifold of E_2

There are three equilibria E_1, E_2 and E_3 and two relative equilibria TW_1 and TW_2 in this system. E_2 and E_3 are symmetric under shifts by $L/2$ and $L/3$ respectively as shown in Figure 12. As shown in [21], one branch of the unstable manifold of E_1 and the unstable manifold of E_3 terminate at E_2 or its symmetry-equivalent counterparts in the full state space. Also, the unstable manifold of E_2 is a set of homoclinic orbits of itself. Therefore, we believe that E_2 has a large influence on the geometrical structure of the in-slice state space.

Figure 22 shows the unstable manifold of E_2 and several pre/relative periodic orbits in the fundamental domain projected into some Fourier mode subspace. Since E_2 and E_3 are in the slice border, their SO(2) symmetry can not be quotiented out by the 1st mode slice. The blue and green straight lines are the group orbits of E_2 and E_3 in the slice respectively. These two lines depict the slice border in this three-dimensional subspace. Note, this does not mean that the unstable manifold of E_2 should also live in the slice. Actually, E_2 has one pair of unstable complex conjugate stability eigenvectors, which do have nonzero first Fourier mode components. Hence, the corresponding unstable manifolds have unique locations, determined by the first Fourier mode phase of this pair of eigenvectors, in the symmetry reduced state space.

There are a few interesting observations in Figure 22. First, the pre/relative periodic

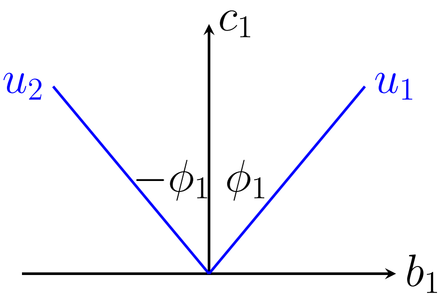

Figure 21: Illustration of the phase relation in Example 3.2.

orbits look continuous, but in fact, they are discontinuous in the fundamental domain. We choose the three-dimensional subspace to be $(\hat{c}_1, \hat{c}_3, \hat{c}_2)$ which is invariant under reflection. Thus reflection has no effect on this specific projection. Second, the unstable manifold of E_2 is discontinuous. Whenever it crosses the slice border, there is a phase jump by π, which causes $\hat{c}_3$ to change sign. Third, we can see that both `ppo8` ($\overline{ppo}_{41.08}$) and `rpo3` ($\overline{rpo}_{33.50}$) shadow the unstable manifold of E_2 for a certain period of time. Actually, there are plenty of pre/relative periodic orbits in our database that shadow the unstable manifold of E_2. In this sense, E_2 plays a substantial role in shaping the dynamics.

3.5.3 Shadowing among orbits

In Figure 22, we see that `ppo2` ($\overline{ppo}_{14.33}$) is quite similar to `rpo1` ($\overline{rpo}_{16.31}$). Actually, these two orbits shadow each other and have similar periods. There are a lot of other shadowing incidences between different pre/relative periodic orbits. For example, in Figure 23(a), $\overline{rpo}_{57.59}$ shadows $\overline{rpo}_{16.31}$ and $\overline{rpo}_{35.97}$ closely. The period of this longer orbit is close to the sum of the periods of the two shorter orbits. In Figure 23(b), $\overline{ppo}_{57.67}$ shadows $\overline{ppo}_{14.33}$ for a certain period of time. Shadowing helps us classify all the pre/relative periodic orbits and helps build the symbolic dynamics of this system. This is important for the spectral determinant (73) to converge quickly when it is expanded by only a few short orbits [22].

On the other hand, preperiodic orbits and relative periodic orbits frequently show up in pairs in the one-dimensional Kuramoto-Sivashinsky equation. For instance, $\overline{rpo}_{57.59}$ in Figure 23(a) and $\overline{ppo}_{57.67}$ in Figure 23(b) are such a pair. N. B. Budanur and P. Cvitanović [12] believe that this phenomenon comes from symmetry-breaking bifurcation as the domain size L is varied.

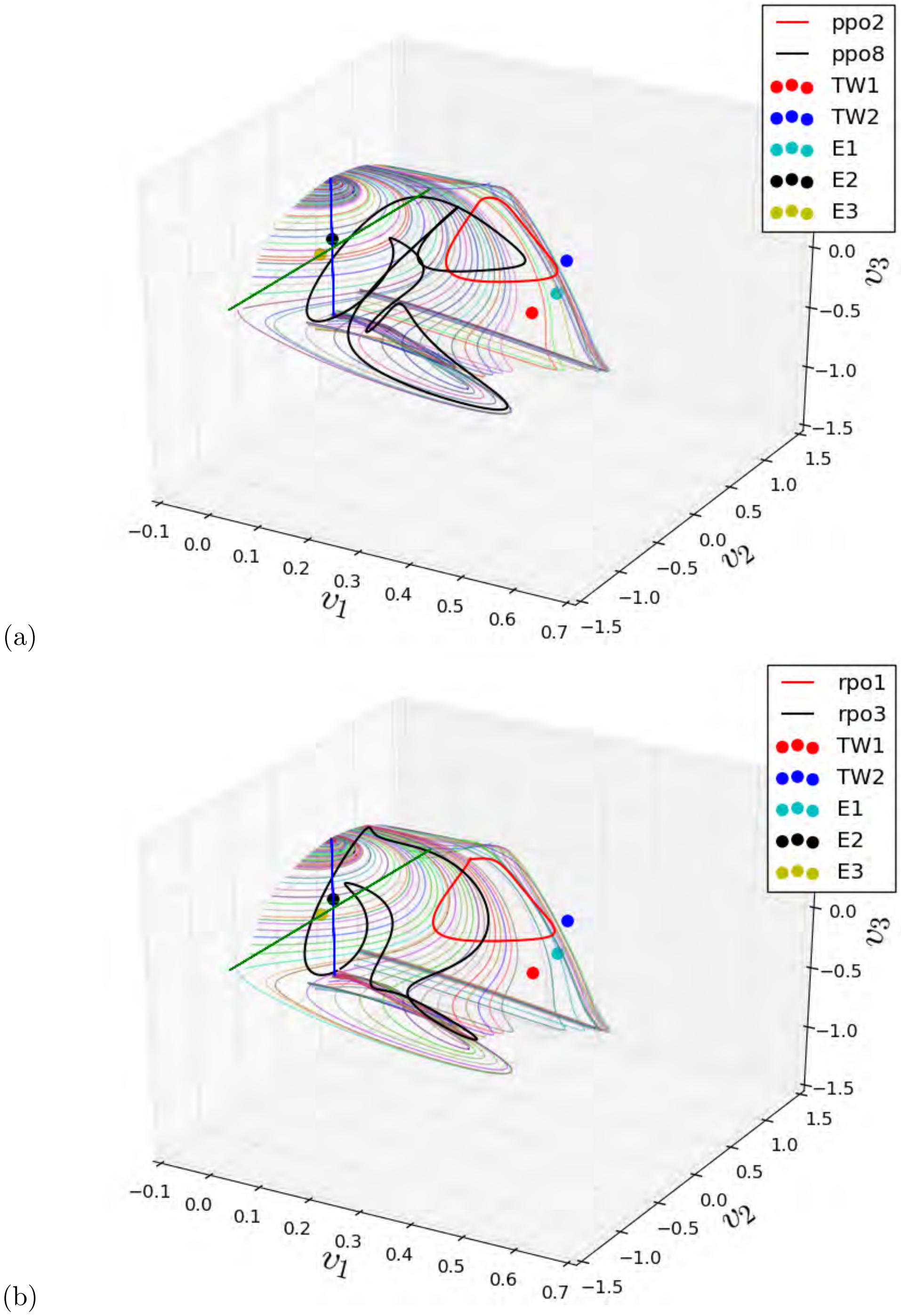

Figure 22: The unstable manifold of E_2 in the fundamental domain in the slice. The dense set of thin curves is the unstable manifold of E_2. The blue and green straight lines are the group orbits of E_2 and E_3 respectively. `ppo2` is $\overline{ppo}_{14.33}$ in Figure 15. `rpo1` is $\overline{rpo}_{16.31}$. `ppo8` is $\overline{ppo}_{41.08}$. `rpo3` is $\overline{rpo}_{33.50}$. Projection axes are the imaginary parts of the first 3 Fourier modes $[v_1, v_2, v_3] = [\hat{c}_1, \hat{c}_3, \hat{c}_2]$. This set is invariant under reflection.

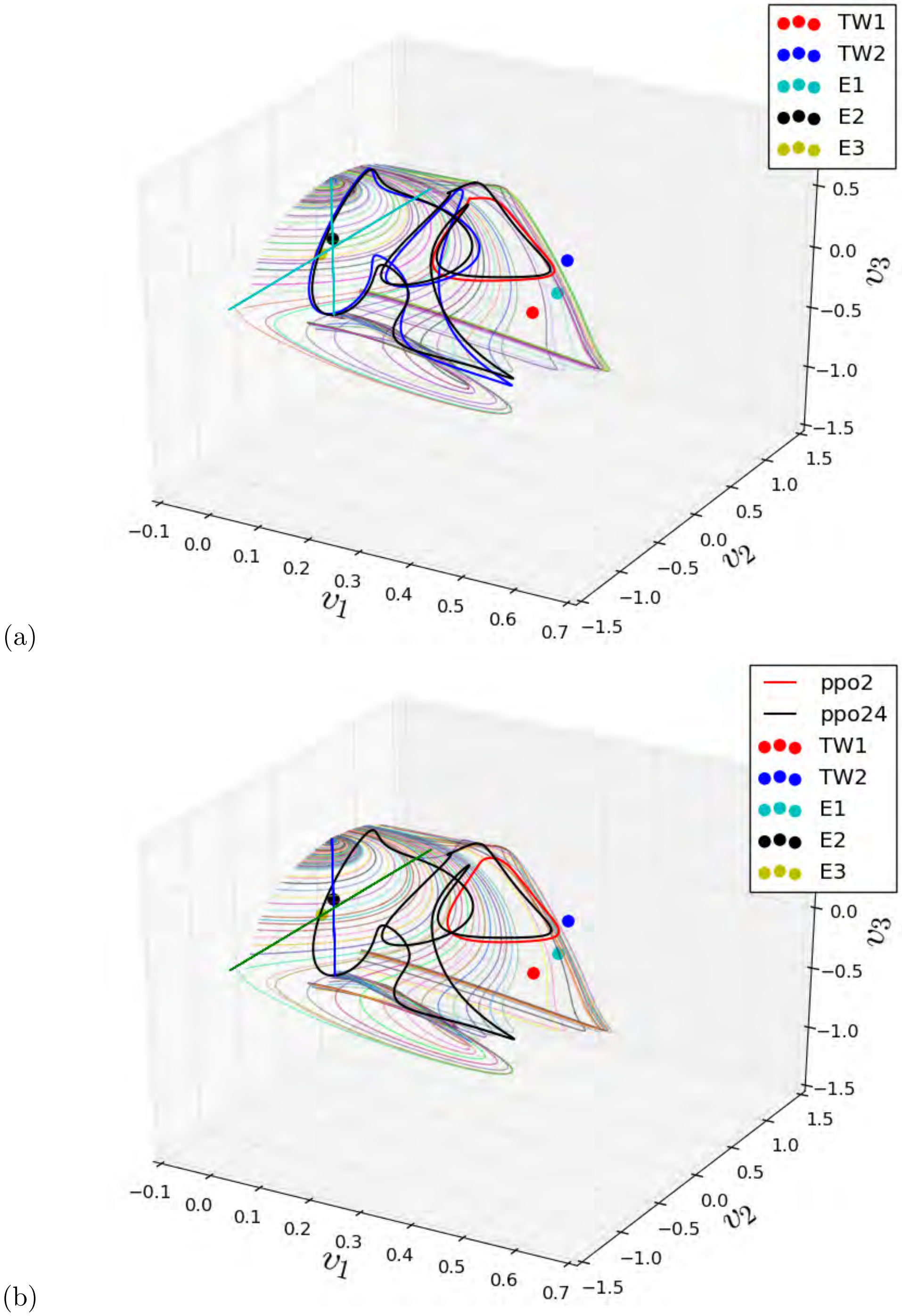

Figure 23: Shadowing among pre/relative periodic orbits in the fundamental domain. The dense set of thin curves is the unstable manifold of E_2. The two straight lines are the group orbits of E_2 and E_3 respectively. Projection axes are the imaginary parts of the first 3 Fourier modes $[v_1, v_2, v_3] = [\hat{c}_1, \hat{c}_3, \hat{c}_2]$. This set is invariant under reflection. (a) The three relative periodic orbits are (red) $\overline{rpo}_{16.31}$, (blue) $\overline{rpo}_{35.97}$ and (black) $\overline{rpo}_{57.59}$. (b) The red preperiodic orbit is `ppo2` ($\overline{ppo}_{14.33}$). The black preperiodic orbit is `ppo24` ($\overline{ppo}_{57.67}$).

CHAPTER IV

THE INERTIAL MANIFOLD OF A KURAMOTO-SIVASHINSKY SYSTEM

As stated in Sect. 1.2, dynamics in chaotic dissipative systems is expected to land, after a transient period of evolution, on the inertial manifold [18, 34, 70, 80, 81], which is a finite-dimensional object in state space. This is true even for infinite-dimensional systems described by partial differential equations, and offers hope that their asymptotic dynamics may be represented by a finite set of ordinary differential equations.

The existence of a finite-dimensional inertial manifold has been established for systems such as the Kuramoto-Sivashinsky, the complex Ginzburg-Landau, and some reaction-diffusion systems [81]. For the Navier-Stokes flows its existence remains an open problem [80], but dynamical studies, such as the determination of sets of periodic orbits embedded in turbulent flows [40, 86], strengthen the case for a geometrical description of turbulence.

In this chapter, we discuss the existence and the dimension of the global attractor and the inertial manifold for a particular one-dimensional Kuramoto-Sivashinsky system, defined on a "minimal domain". Our discussion has two parts. In Sect. 4.1, we review the mathematical proof of the existence of a global attractor and the rigorous bounds for the dimension of the inertial manifold. In Sect. 4.2, we determine the dimension of the inertial manifold by the numerical study of Floquet vectors along pre/relative periodic orbits for this particular system.

4.1 The existence of an inertial manifold

As discussed in Sect. 1.2.3, an inertial manifold is the graph of a map $\Phi : P_n\mathcal{M} \mapsto Q_n\mathcal{M}$, where P_n is the projection to the eigenspace spanned by the eigenvectors of $\partial_{xx} + \partial_{xxxx}$, corresponding to its smallest n eigenvalues. $\partial_{xx} + \partial_{xxxx}$ has eigenvalues $-q_k^2 + q_k^4$ with Fourier modes as eigenvectors. Thus the existence of an inertial manifold indicates that a finite number of low frequency Fourier modes can describe the asymptotic behavior of this system. Any trajectory will be attracted to this manifold exponentially fast. This expectation is also reflected in (135), where the velocity field of a high frequency Fourier mode, i.e., a_k with large k, is dominated by the linear part $(q_k^2 - q_k^4)\, a_k$. Thus, high frequency Fourier modes are almost decoupled from other modes.

An inertial manifold exists in a system which possesses the *strong squeezing property* (22)–(25). As shown in Theorem 1.7, as long as the spectrum of $\partial_{xx}+\partial_{xxxx}$ has a sufficiently large gap for some n, then an inertial manifold exists. The kth eigenvalue of $\partial_{xx} + \partial_{xxxx}$ is $\lambda_k = -q_k^2 + q_k^4$. so $\lambda_{n+1} - \lambda_n$ is unboundedly increasing with respect to n. In one-dimensional Kuramoto-Sivashinsky equation (134), the nonlinear part of the velocity field is $-uu_x$. If we can determine a Lipschitz constant C_1 for $-uu_x$, then surely there is an n such that $\lambda_{n+1} - \lambda_n > 4C_1$. As a result, an inertial manifold exists.

Strong squeezing property has been shown to hold for one-dimensional Kuramoto-Sivashinsky equation (Theorems 3.2 and corollary 3.7 in [35], Theorem 4 in [69]). Moreover, Robinson (Corollary 5 in [69]) states that if there is an absorbing ball with radius $O(L^{\alpha})$ [1] in the one-dimensional Kuramoto-Sivashinsky equation, then an inertial manifold exists with dimension bounded above by $O(L^{3\alpha/5+3/2})$. Also, Theorem 1.3 says that a global attractor exists if an absorbing set exists in the state space. Therefore, both a global attractor and an inertial manifold exist, provided the existence of an absorbing set in the state space, which is a Hilbert space with the L^2 norm

$$\| u \|_2 = \left(\int_0^L u^2 dx \right)^{1/2} .$$

4.1.1 Rigorous upper bounds

In 1985, Nicolaenko, Scheurer and Temam [65] gave the first asymptotic boundedness of the L^2 norm of $u(x,t)$ in the antisymmetric subspace, showing the existence of an absorbing ball $S = \{u : \| u \|_2 \leq CL^{5/2}\}$ for antisymmetric solutions. They also show that the Hausdorff dimension of the global attractor is bounded above by $O(L^{13/8})$. This antisymmetric assumption was later removed by Goodman [43]. The estimate was improved by Collet *et al.* [17] who extended it to the whole state space and improved the exponent from 5/2 to 8/5. In 2006, Bronski and Gammbill [10] gave a better upper bound

$$\limsup_{t\to\infty} \| u \|_2 = O(L^{\frac{3}{2}}) . \tag{142}$$

All these results were obtained through the Lyapunov function approach, the main idea of which is to find an appropriate gauge function $\Phi(x)$:

$$u(x,t) = v(x,t) + \Phi(x) \tag{143}$$

such that the transformed field $\| v(x,t) \|_2$ is bounded. Upper bound (142) is claimed to be the best result one can get by the Lyapunov function approach. On the other hand, by treating Kuramoto-Sivashinsky equation as a perturbation of Burgers' equation, Giacomelli and Otto [39] proved that [2]

$$\limsup_{t\to\infty} \|u\|_2 = o(L^{\frac{3}{2}}) . \tag{144}$$

Later on, Otto [67] shows that

$$\limsup_{t\to\infty} \frac{1}{T} \int_0^T dt \, \| \, |\partial_x|^{\alpha} u \, \|^2 = O(L \cdot \ln^{10/3} L) , \qquad 1/3 < \alpha \leq 2 ,$$

and claims that it is the optimal bound for the one-dimensional Kuramoto-Sivashinsky equation. The norm of the time-averaged fractional derivatives of $u(x,t)$ is almost proportional to $L^{1/2}$. Bronski and Gammbill [10] also claim that 1/2 is believed to be the best possible exponent.

Based on an upper bound of size of the attracting set, we can estimate the dimension of the inertial manifold. In 1988, Foias, Nicolaenko, Sell and Temam [35] gave an upper bound $O(L^{7/2})$ for the dimension of the inertial manifold. Better estimate $O(L^{2.46})$ is

---

[1] The big-O notation: $f(x) = O(g(x))$ if and only if there exists a positive real number M and a real number x_0 such that $|f(x)| \leq M|g(x)|$ for all $x \geq x_0$.

[2] The little-O notation : $f(x) = o(g(x))$ if and only if there exists a a real number x_0 such that $|f(x)| \leq M|g(x)|$ for all $x \geq x_0$ and for all positive real number M.

given in ref. [33, 50]. Based on bound (144), the upper bound can be further improved to $o(L^{12/5})$ [39].

In the remaining part of this section, we show the existence of an absorbing ball through the Lyapunov function approach. The main result comes from the work of Collet *et al.* [17]. Though the estimate is not optimal, it demonstrates the general process of obtaining the upper bound by choosing an appropriate gauge function in (143).

4.1.2 Existence of an absorbing ball

Due to Galilean invariance of the Kuramoto-Sivashinsky equation, we impose zero mean velocity $\int_0^L u(x,t)dx = 0$ in the state space. Then we state that

Theorem 4.1 *There is an absorbing ball S with radius $CL^{8/5}$ in the one-dimensional Kuramoto-Sivashinsky equation defined on a periodic domain $[0, L]$. Here, C is a constant.*

Here, for simplicity, we only provide the proof of theorem 4.1 for the antisymmetric case. For the full proof, please refer [17, 50]. That is , we impose that both $v(x,t)$ and $\Phi(x)$ in (143) have period L and are antisymmetric: $v(-x,t) = -v(x,t)$, $\Phi(-x) = -\Phi(x)$. Then rewriting Kuramoto-Sivashinsky equation (134) in terms of $v(x,t)$, we have

$$v_t = (-\partial_x^2 - \partial_x^4)(v + \Phi) - vv_x - v\Phi_x - \Phi v_x - \Phi\Phi_x \,.$$

Multiplying on both sides of the above equation with v and integrating over the whole domain, we get

$$\begin{aligned}\frac{1}{2}\partial_t \int v^2 &= \int v(-\partial_x^2 - \partial_x^4)(v+\Phi) - \int v^2 v_x - \int v^2\Phi_x - \int v\Phi v_x - \int v\Phi\Phi_x \\ &= \int v(-\partial_x^2 - \partial_x^4)(v+\Phi) - 0 - \int v^2\Phi_x + \frac{1}{2}\int v^2\Phi_x - \int v\Phi\Phi_x \\ &= \int v(-\partial_x^2 - \partial_x^4)(v+\Phi) - \frac{1}{2}\int v^2\Phi_x - \int v\Phi\Phi_x \,. \qquad (145)\end{aligned}$$

In the above, $\int v^2 v_x$ vanishes because of the periodic boundary condition. From (145), we see that the evolution of $\| v(x,t) \|_2^2$ depends on the choice of the gauge function. In order to bound $\| v(x,t) \|_2$, we need to bound the right side of (145) for some carefully chosen gauge function $\Phi(x)$. Before that, we define notation

$$(v_1, v_2)_{\gamma\Phi} = \int v_1(\partial_x^2 + \partial_x^4 + \gamma\Phi_x)v_2 \,. \qquad (146)$$

Therefore, (145) becomes

$$\frac{1}{2}\partial_t \int v^2 = -(v,v)_{\Phi/2} - (v,\Phi)_\Phi \,. \qquad (147)$$

To bound the right side of (147), we bring up two propositions.

Proposition 4.2 *There is a constant K and an antisymmetric gauge function $\Phi(x)$ such that for all $\gamma \in [\frac{1}{4}, 1]$ and all antisymmetric $v(x,t)$ one have inequalities*

$$(v,v)_{\gamma\Phi} \geq \frac{1}{4}\int (v_{xx}^2 + v^2) \quad \textit{and} \qquad (148)$$

$$(\Phi,\Phi)_{\gamma\Phi} \leq KL^{16/5} \,. \qquad (149)$$

Proposition 4.3 *Definition (146) defines an inner product in the L^2 space.*

With these two propositions, we then continue from (147),

$$\begin{aligned}
\frac{1}{2}\partial_t \int v^2 &\leq -(v,v)_{\Phi/2} + (v,v)_{\Phi}^{1/2} (\Phi,\Phi)_{\Phi}^{1/2} &(150)\\
&= -(v,v)_{\Phi/2} + (\epsilon (v,v)_{\Phi})^{1/2} \left(\frac{1}{\epsilon}(\Phi,\Phi)_{\Phi}\right)^{1/2} \\
&\leq -(v,v)_{\Phi/2} + \frac{\epsilon}{2}(v,v)_{\Phi} + \frac{1}{2\epsilon}(\Phi,\Phi)_{\Phi} \\
&= -\int v \left((1-\frac{\epsilon}{2})(\partial_x^2 + \partial_x^4) + (\frac{1}{2} - \frac{\epsilon}{2})\gamma \Phi_x \right) v + \frac{1}{2\epsilon}(\Phi,\Phi)_{\Phi} \\
&= -(1-\frac{\epsilon}{2})(v,v)_{\Phi(\frac{1}{2}-\frac{\epsilon}{2})/(1-\frac{\epsilon}{2})} + \frac{1}{2\epsilon}(\Phi,\Phi)_{\Phi} \\
&\leq -(1-\frac{\epsilon}{2})\frac{1}{4}\int (v_{xx}^2 + v^2) + \frac{1}{2\epsilon}(\Phi,\Phi)_{\Phi} &(151)\\
&\leq -(1-\frac{\epsilon}{2})\frac{1}{4}\int v^2 + \frac{1}{2\epsilon}(\Phi,\Phi)_{\Phi}\,.
\end{aligned}$$

We set $\epsilon = 2/3$ to make $(\frac{1}{2} - \frac{\epsilon}{2})/(1-\frac{\epsilon}{2}) = 1/4$, so we get

$$\partial_t \int v^2 \leq -\frac{1}{3}\int v^2 + \frac{3}{2}(\Phi,\Phi)_{\Phi}\,. \tag{152}$$

Step (150) has used proposition 4.3 such that Cauchy-Schwarz inequality can be applied : $(v,\Phi)^2 \leq (v,v)(\Phi,\Phi)$. Step (151) has used (148) in proposition 4.2. Derivative of $\int v^2$ is bounded as shown in (152) and note that term $\frac{3}{4}(\Phi,\Phi)_{\Phi}$ does not depend on time, so applying lemma 1.5, we obtain

$$\int v(x,t)^2 dx \leq e^{-t/3}\int v(x,0)^2 dx + \frac{9}{2}(1-e^{t/3})(\Phi,\Phi)_{\Phi}\,. \tag{153}$$

Since $u(x,t) = v(x,t) + \Phi(x)$, we therefore obtained an absorbing ball in the Kuramoto-Sivashinsky equation centered at $\Phi(x)$ with radius $\rho > \rho_0$, where

$$\rho_0 = 3\sqrt{\frac{(\Phi,\Phi)_{\Phi}}{2}} = O(L^{8/5})\,. \tag{154}$$

Here, we have used relation (149). Actually, Jolly, Rosa, and Temam [50] constructed a gauge function such that the L^2 norm of Φ is bounded $\| \Phi \|_2 = O(L^{3/2})$. Therefore, the center of the absorbing ball can be moved to the origin. Thus

$$\limsup_{t\to\infty} \| u(x,t) \|_2 = O(L^{8/5}) + O(L^{3/2}) = O(L^{8/5})\,.$$

As shown in (154), the radius of the absorbing ball depends on the choice of the gauge function $\Phi(x)$. To make the radius as small as possible, we try to minimize the exponent in (149) and at the same time to meet the requirement of (148). This requires us to choose the gauge function with the least norm which also supports (149) and proposition 4.3. Actually, proposition 4.3 is a natural corollary of proposition 4.2. The reason is as follows. Apparently, the bilinear form (146) satisfies relations $(\lambda v_1 + \mu v_2, v_3)_{\gamma\Phi} = \lambda(v_1,v_3)_{\gamma\Phi} + \mu(v_2,v_3)_{\gamma\Phi}$ and $(v_1,v_2)_{\gamma\Phi} = (v_2,v_1)_{\gamma\Phi}$. In order to make it an inner product, we only need to demonstrate that $(v,v)_{\gamma\Phi} \geq 0$ with equality if and only if $v = 0$. Equation (148) provides this relation. Therefore, we only need to prove proposition 4.2, which is given in appendix B.

4.2 Numerical evidence provided by Floquet vectors

While mathematical approaches provide rigorous bounds on dimensions of inertial manifolds, their constructive description remains a challenge. In this section, we provide numerical evidence that gives a specific integer dimension of the inertial manifold inside the one-dimensional Kuramoto-Sivashinsky equation. We show that the finite-dimensional physical manifold can be precisely embedded in its infinite-dimensional state space, thus opening a path towards its explicit construction. The key idea [22] is to populate the inertial manifold by an infinite hierarchy of unstable time-invariant solutions, such as periodic orbits, an invariant skeleton which, together with the local "tiles" obtained by linearization of the dynamics, fleshes out the physical manifold. Chaos can then be viewed as a walk on the inertial manifold, chaperoned by the nearby unstable solutions embedded in the physical manifold. Unstable periodic orbits have already been used to compute global averages of spatiotemporally chaotic flows [16, 21, 40, 56].

In our analysis, we use 200 preperiodic orbits and 200 relative periodic orbits. These are the shortest periodic orbits taken from the set of over 60 000 determined in ref. [21] by near-recurrence searches. The method preferentially finds orbits embedded in the long-time attracting set but offers no guarantee that all orbits up to a given period have been found. There are infinitely many unstable orbits, and each of them possesses infinitely many Floquet modes. While in the example that we study here we do not have a detailed understanding of the organization of periodic orbits (their symbolic dynamics), we show that one only needs to consider a finite number of them to tile the physical manifold to a reasonable accuracy. We also show, for the first time, that each local tangent tile spanned by the Floquet vectors of an unstable periodic orbit splits into a set of physical Floquet modes and the remaining set of spurious modes. Furthermore, we verify numerically that the physical Floquet manifold coincides locally with the physical manifold determined by the covariant Lyapunov vectors approach.

4.2.1 Motivation from covariant vectors

Recent progress towards this aim came from numerical investigations of the covariant vectors of spatiotemporally chaotic flows [79, 90], made possible by the algorithms developed in refs. [41, 42, 87]. These works have revealed that the tangent space of a generic spatially-extended dissipative system is split into two hyperbolically decoupled subspaces: a finite-dimensional subspace of "entangled" or "physical" Lyapunov modes (referred to in what follows as the "physical manifold"), which is presumed to capture all long-time dynamics, and the remaining infinity of transient ("isolated," "spurious") Lyapunov modes. Covariant (Lyapunov) vectors span the Oseledec subspaces [28, 66] and thus indicate the intrinsic directions of growth or contraction at every point on the physical manifold. The dynamics of the vectors that span the physical manifold is entangled, with frequent tangencies between them. The spurious modes, on the other hand, are damped so strongly that they are isolated - at no time do they couple by tangencies to the physical modes. Specifically, for domain size $L = 22$, the physical manifold consists of the leading 8 covariant vectors.

It was conjectured in ref. [79, 90] that the physical manifold provides a local linear approximation to the inertial manifold at any point on the attractor, and that the dimension of the inertial manifold is given by the number of the physical Lyapunov modes. Further support for this conjecture was provided by ref. [89], which verified that the vectors connecting pairs of recurrent points –points on the chaotic trajectory far apart in time but nearby each other in state space– are confined within the local tangent space of the physical manifold.

While these works showed that the physical manifold captures the finite dimensionality of the inertial manifold, they do not tell us much about how this inertial manifold is actually laid out in state space. This is the primary reason that we instead study the set of pre/relative periodic orbits inside this system as they form the backbone the attractor.

4.2.2 Decoupling of local Floquet exponents

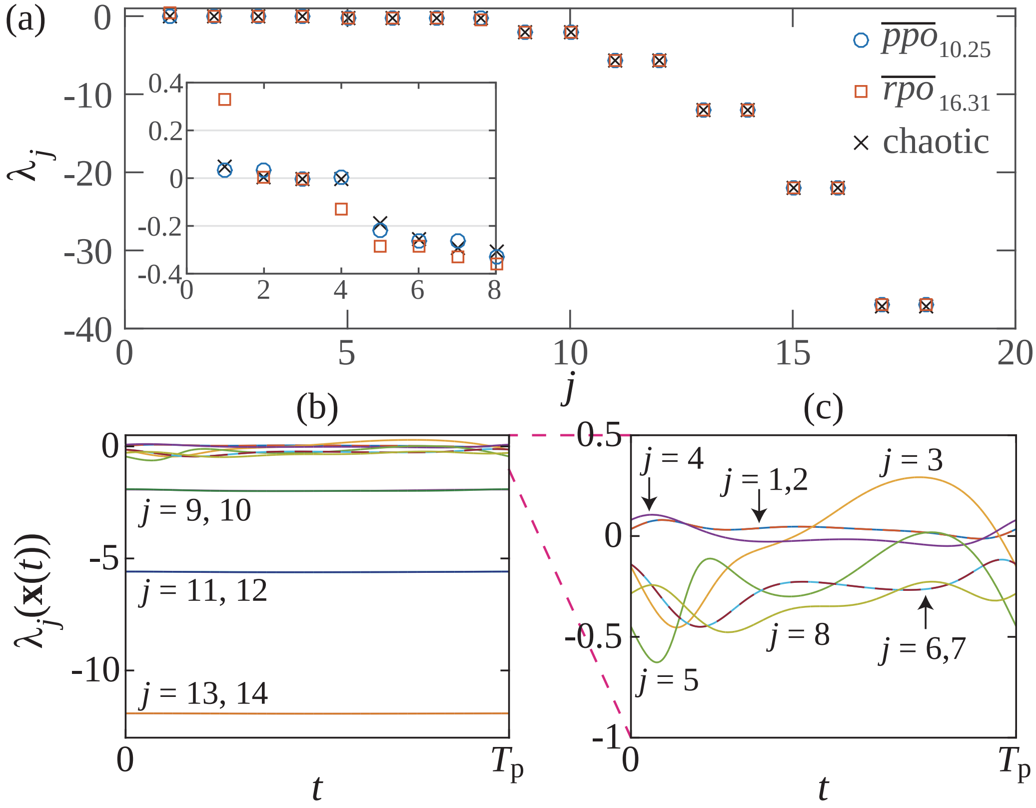

Figure 24: (a) Floquet exponents for $\overline{ppo}_{10.25}$ (circles), $\overline{rpo}_{16.31}$ (squares), and Lyapunov exponents of a chaotic trajectory (crosses). The inset shows a close-up of the 8 leading exponents. For the full Floquet spectrum of these two orbits, see Table 7. (b) Time series of local Floquet exponents $\lambda_j(u(t))$ for $\overline{ppo}_{10.25}$. (c) Close-up of (b) showing the 8 leading exponents. Dashed lines indicate degenerate exponent pairs corresponding to complex Floquet multipliers.

The definitions of Floquet exponents and Floquet vectors are given in Sect. 1.3.1. More specifically, for preperiodic orbits and relative periodic orbits defined in Sect. 3.2, Floquet multipliers Λ_j and vectors $\boldsymbol{e}_j(u)$ are the eigenvalues and eigenvectors of Jacobian matrix $J_p = RJ^{T_p}$ or $J_p = g(\theta_p)J^{T_p}$ for pre-periodic or relative periodic orbits, respectively, explained in Sect. 3.2. The Floquet exponents λ_j (if complex, we shall only consider their real parts, with multiplicity 2) are related to multipliers by $\lambda_j = \ln|\Lambda_j|/T_p$. For an orbit $(\lambda_j, \boldsymbol{e}_j)$ denotes the jth Floquet (exponent, vector); for a chaotic trajectory it denotes the jth Lyapunov (exponent, vector).

Figure 24 (a) shows the Floquet exponents spectra for the two shortest orbits, $\overline{ppo}_{10.25}$ and $\overline{rpo}_{16.31}$, overlaid on the Lyapunov exponents computed from a chaotic trajectory. The basic structure of this spectrum is shared by all 400 orbits used in our study. [3] For chaotic trajectories, hyperbolicity between an arbitrary pair of Lyapunov modes can be characterized by a property called the domination of Oseledec splitting (DOS) [7, 68]. Consider a set of finite-time Lyapunov exponents

$$\lambda_j^\tau(u) \equiv \frac{1}{\tau} \ln ||J^\tau(u) \boldsymbol{e}_j(u)|| \,, \tag{155}$$

with L^2 normalization $\| \boldsymbol{e}_j(u) \| = 1$. A pair of modes $j < \ell$ is said to fulfill 'DOS strict ordering' if $\lambda_j^\tau(u) > \lambda_\ell^\tau(u)$ along the entire chaotic trajectory, for τ larger than some lower bound τ_0. Then this pair is guaranteed not to have tangencies [7, 68]. For chaotic trajectories, DOS turned out to be a useful tool to distinguish physical modes from hyperbolically decoupled spurious modes [79, 90]. Periodic orbits are by definition the infinite-time orbits (τ can be any repeat of T_p), so generically all nondegenerate pairs of modes fulfill DOS. Instead, we find it useful to define, by analogy to the 'local Lyapunov exponent' [9], the 'local Floquet exponent' as the action of the strain rate tensor [57] $2\, D(u) = A(u)^\top + A(u)$ (where A is the stability matrix (28)) on the normalized jth Floquet eigenvector,

$$\lambda_j(u) = \boldsymbol{e}_j(u)^\top D(u)\, \boldsymbol{e}_j(u) = \lim_{\tau \to 0} \lambda_j^\tau(u) \,. \tag{156}$$

We find that time series of local Floquet exponents $\lambda_j(u(t))$ indicate a decoupling of the leading 'physical' modes from the rest of the strictly ordered, strongly negative exponents [Figure 24 (b) and (c)]. Another example, the local Floquet exponents of $\overline{rpo}_{16.31}$ is shown in Figure 25. Perhaps surprisingly, for every one of the 400 orbits we analyzed, the number of the physical Floquet modes was *always* 8, equal to the previously reported number of the physical Lyapunov modes for this system [89]. [4] This leads to our first surmise: (1) each individual orbit embedded in the attracting set carries enough information to determine the dimension of the physical manifold.

4.2.3 Decoupling of Floquet vectors

For an infinite-time chaotic trajectory, hyperbolicity can be assessed by measuring the distribution of minimal principal angles [6, 53] between any pair of subspaces spanned by Lyapunov vectors [41, 79, 90]. For any two subspaces U and V, the kth principal angle θ_k is defined as $\cos(\theta_k) = \max(u^\top v)$. Here, u and v are two normalized vectors in U and V and are subject to restriction $u^\top u_i = 0\,, v^\top v_i = 0$ for $i = 1, \ldots, k-1$. Here, u_i and v_i achieve the ith principal angle. Therefore, we can also write $\cos(\theta_k) = (u_k^\top v_k)$. Principle angles provide information about the relative position of these two subspaces in their embedding space. For our purpose, we are only interested in the first principal angle which is the smallest angle that can be formed by two arbitrary vectors from these two subspaces. Let $U = Q_u R_u$ and $V = Q_v R_v$ be the QR decomposition of U and V respectively, then the first principal angle is given as $\theta_1 = \arccos(\sigma_1)$, with σ_1 the smallest singular value of $Q_u^\top Q_v$. In the following, whenever we say principal angle θ or ϕ, we shall be referring to the first principal angle.

---

[3] Refs. [79, 89, 90] include the marginal Galilean symmetry mode in the mode count; here this mode is absent, as we have set $\int u(x,t)dx = 0$. Consequently, the number of the physical modes (the dimension of the physical manifold) differs by one.

[4] see footnote 3 on page 62.

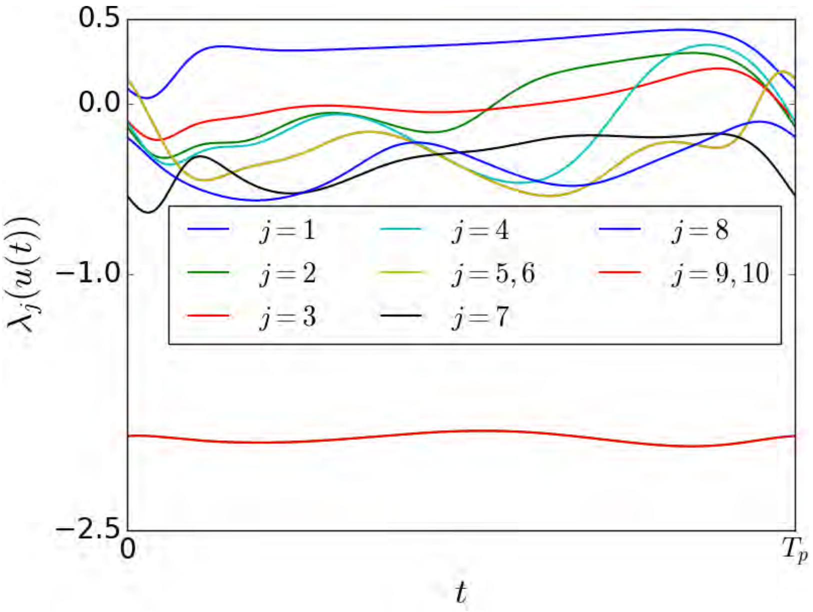

Figure 25: The leading 10 local Floquet exponents of $\overline{rpo}_{16.31}$ along the orbit for one period. The (5th, 6th) and (9th, 10th) exponents are complex conjugate pairs. See Table 7 for its full spectrum.

Numerical work indicates that as the physical and spurious modes are hyperbolically decoupled, the distribution of the angles between these subspaces is bounded away from zero, and that observation yields a sharp physical-spurious threshold. This strategy cannot be used for individual orbits, as each one is of a finite period, and the minimal principal angle reached by a pair of Floquet subspaces remains strictly positive. Instead, we measure the angle distribution for a *collection* of orbits, and find that the physical-spurious threshold is as sharp as for a long chaotic trajectory: Figure 26 shows the principal angle distribution between two subspaces S_n and $\bar{S}_n$, with S_n spanned by the leading n Floquet vectors and $\bar{S}_n$ by the rest. As in the Lyapunov analysis of long chaotic trajectories [90], the distributions for small n indicate strictly positive density as $\phi \to 0$. In contrast, the distribution is strictly bounded away from zero angles for $n \geq 8$, the number determined above by the local Floquet exponents analysis. This leads to our second surmise: (2) the distribution of principal angles for collections of periodic orbits enables us to identify a finite set of *physical Floquet modes*, the analogue of the chaotic trajectories' physical covariant vector modes.

4.2.4 Shadowing controlled by Floquet vectors

It is known, at least for low-dimensional chaotic systems, that a dense set of periodic orbits constitutes the skeleton of a strange attractor [22]. Chaotic trajectories meander around these orbits, approaching them along their stable manifolds, and leaving them along their unstable manifolds. If trajectories are indeed confined to a finite-dimensional physical manifold, such shadowing events should take place within the subspace of physical Floquet modes of the shadowed orbit. To analyze such shadowing, we need to measure the distances between the chaotic trajectories and the invariant orbits. But due to SO(2) symmetry, such shadowing actually happens between two tori, so we work in the 1st mode slice (137) defined in Sect. 3.2 to investigate shadowing incidences.

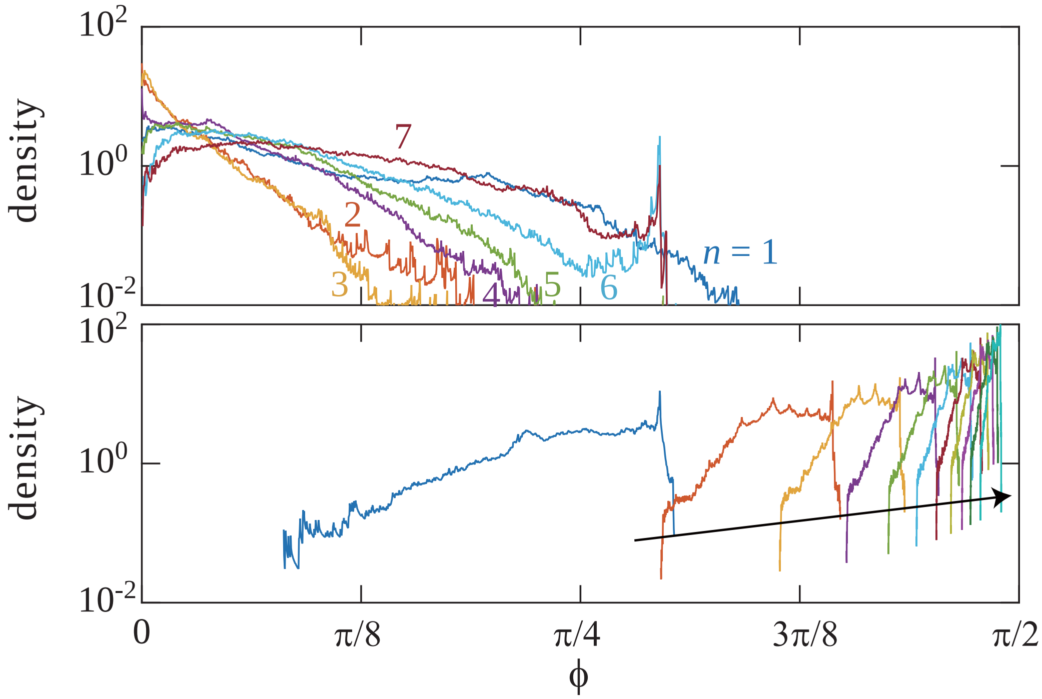

Figure 26: A histogram of the principal angles ϕ between S_n (the subspace spanned by the n leading Floquet vectors) and $\bar{S}_n$ (the subspace spanned by the remaining $d - n$ Floquet vectors), accumulated over the 400 orbits used in our analysis. (top panel) For $n = 1, 2, \cdots, 7$ (S_n within the physical manifold) the angles can be arbitrarily small. (bottom panel) For $n = 8, 10, 12, \cdots, 28$ (in the order of the arrow), for which all physical modes are contained in S_n, the angles are bounded away from unity.

The dimension of the slice subspace is one less than that of the full state space: slice eliminates the marginal translational direction, while the remaining Floquet multipliers Λ_j are unchanged. Therefore, for the system studied here, there are only seven physical modes, with one marginal mode (time invariance) in the in-slice description, instead of eight and two, respectively, in the full state space description. Although we calculate Floquet vectors in the full state space, relation (129) tells us how to get in-slice Floquet vectors from Floquet vectors in the full state space.

A shadowing of an orbit $u_p(x, t')$ by a nearby chaotic trajectory $u(x, t)$ is then characterized by the in-slice separation vector

$$\Delta\hat{u}(x, t) \equiv \hat{u}(x, t) - \hat{u}_p(x, t_p), \tag{157}$$

where t_p is chosen to minimize the in-slice distance $||\Delta\hat{u}||$. Now we test whether the $\Delta\hat{u}(x, t)$ is confined to the tangent space spanned by the physical in-slice Floquet vectors. To evaluate this confinement, one needs to take into account the nonlinearity of the stable and unstable manifolds for finite amplitude of $\Delta\hat{u}(x, t)$. We decompose the separation vector as

$$\Delta\hat{u}(x, t) = \hat{v}_n(x, t) + \hat{w}_n(x, t), \tag{158}$$

where $\hat{v}_n(x, t)$ is a vector in the subspace $\hat{S}_n$ spanned by the leading n in-slice Floquet vectors and $\hat{w}_n(x, t)$ is in the orthogonal complement of $\hat{S}_n$. If n is large enough so that $\hat{S}_n$ contains

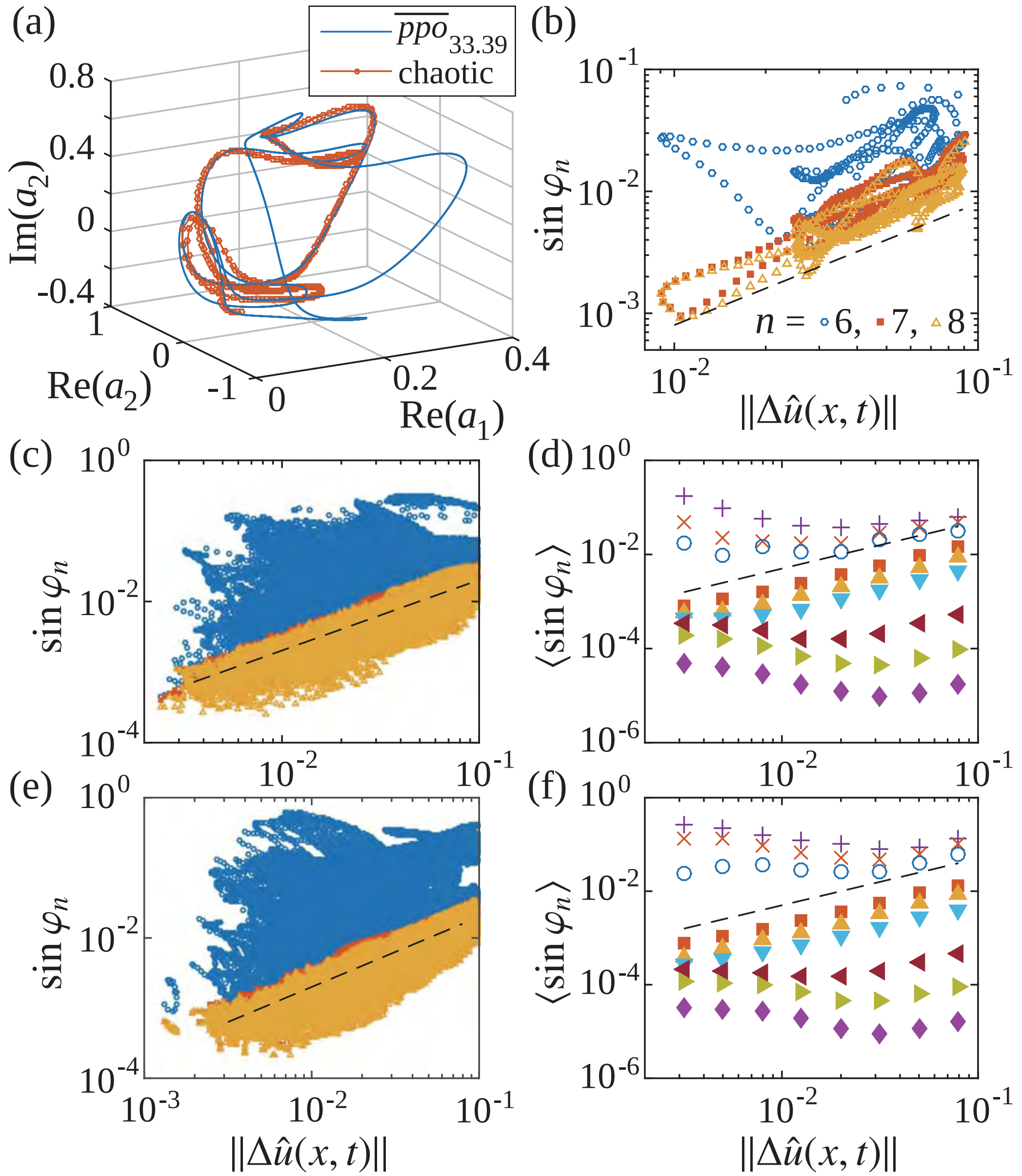

Figure 27: (a) Shadowing event between a chaotic trajectory and $\overline{ppo}_{33.39}$, drawn over $2\,T_p$. (b) Parametric plot of $\sin\varphi_n(t)$ vs $||\Delta\hat{u}(x,t)||$ during the single shadowing event shown in (a), for $n = 6, 7, 8$. (c) Same as (b), but a total of 230 shadowing events of $\overline{ppo}_{33.39}$ are used. (d) Average of $\sin\varphi_n$ in (c), taken within each bin of the abscissa, for $n = 4, 5, 6, 7, 9, 11, 17, 21, 25$ from top to bottom. (e)(f) Same as (c)(d), respectively, but for 217 shadowing events with $\overline{rpo}_{34.64}$. The dashed lines show $\sin\varphi_n \propto ||\Delta\hat{u}||$ in all panels.

the local approximation of the inertial manifold, we expect $||\hat{w}_n|| \sim ||\hat{v}_n||^2 \sim ||\Delta\hat{u}||^2$ because of the smoothness of the inertial manifold; otherwise $||\hat{w}_n||$ does not vanish as $||\Delta\hat{u}|| \to 0$. In terms of the angle φ_n between $\hat{S}_n$ and $\Delta\hat{u}$, $\sin\varphi_n \sim ||\hat{w}_n||/||\hat{v}_n|| \sim ||\Delta\hat{u}||$ for n above the threshold, while $\sin\varphi_n$ remains non-vanishing otherwise.

Following this strategy, we collected segments of a long chaotic trajectory during which it stayed sufficiently close to a specific orbit for at least one period of the orbit. Figure 27 (a) illustrates such a shadowing event for $\overline{ppo}_{33.39}$. A parametric plot of $\sin\varphi_n(t)$ vs. $||\Delta\hat{u}(x,t)||$ during this event is shown in Figure 27 (b) for $n = 6, 7, 8$ (blue circles, red squares, orange triangles, respectively). We can already speculate from such a single shadowing event that $\sin\varphi_n$ does not necessarily decrease with $||\Delta\hat{u}||$ for $n < 7$, while it decreases linearly with $||\Delta\hat{u}||$ for $n \geq 7$. This threshold is clearly identified by accumulating data for all the recorded shadowing events with $\overline{ppo}_{33.39}$, Figure 27 (c): $\sin\varphi_n$ is confined below a line that depends linearly on $||\Delta\hat{u}||$ if and only if $n \geq 7$. Similarly, there is a clear separation in the average of $\sin\varphi_n$ taken within each bin of the abscissa [Figure 27 (d)]. This indicates that for $n < 7$ (empty symbols), typical shadowing events manifest significant deviation of $\Delta\hat{u}$ from the subspace $\hat{S}_n$, whereas for $n \geq 7$ (solid symbols) $\Delta\hat{u}$ is always confined to $\hat{S}_n$. We therefore conclude that shadowing events are confined to the subspace spanned by the leading 7 in-slice Floquet vectors, or equivalently, by all the 8 physical Floquet vectors in the full state space. The same conclusion was drawn for $\overline{rpo}_{34.64}$ [Figure 27 (e) and (f)] and five other orbits (not shown). We also verified that, when a chaotic trajectory approaches an orbit, the subspace spanned by all physical Floquet modes of the orbit coincides with that spanned by all physical Lyapunov modes of the chaotic trajectory. This implies our third surmise: (3) the physical Floquet manifold coincides locally with the physical Lyapunov manifold, with either capturing the local structure of the inertial manifold.

4.2.5 Summary

In summary, we used the Kuramoto-Sivashinsky system to demonstrate by six independent calculations that the tangent space of a dissipative flow splits into physical vs. spurious subspaces, and to determine the dimension of its inertial manifold. The *Lyapunov modes* approach of refs. [41, 79, 89, 90] identifies (1) the "physical" Lyapunov exponents, by the dynamics of finite-time Lyapunov exponents, (155); and (2) the "physical" tangent manifold, or "physical manifold," by measuring the distributions of angles between covariant vectors. The *Floquet modes* approach [24] developed here shows that (3) Floquet exponents of each *individual* orbit separate into physical vs. spurious, Figure 24; (4) for ensembles of orbits, the principal angles between hyperplanes spanned by Floquet vectors separate the tangent space into physical vs. spurious, Figure 26; (5) for a chaotic trajectory shadowing a given orbit the separation vector lies within the orbit's Floquet physical manifold, Figure 27; and (6) for a chaotic trajectory shadowing a given orbit the separation vector lies within the covariant vectors' physical manifold.

All six approaches yield the same inertial manifold dimension, reported in earlier work [89]. [5] The Floquet modes / unstable periodic orbits approach is constructive, in the sense that periodic points should enable us, in principle (but not attempted in this thesis), to tile the global inertial manifold by local tangent spaces of an ensemble of such points. Moreover, and somewhat surprisingly, our results on individual orbits' Floquet exponents, Figure 24 (b) and (c), and on shadowing of chaotic trajectories, Figure 27, suggest that *each individual orbit* embedded in the attracting set contains sufficient information to determine the physical-spurious threshold. However, the computation and organization of unstable periodic orbits is still a major undertaking, and can currently be carried out only for rather small computational domains [21, 86]. The good news is that the physical Lyapunov modes approach [90] suffices to determine the inertial manifold dimension, as Lyapunov modes calculations only require averaging over long chaotic trajectories, are much easier to implement,

---

[5] see footnote 3 on page 62.

and can be scaled up to much larger domain sizes than $L = 22$ considered here.

We hope the computational tools introduced here, namely, local Floquet exponents, principal angles obtained by Floquet vectors, and expansion errors of difference vectors in shadowing incidences, will eventually contribute to solving outstanding issues of dynamical systems theory, such as the existence of an inertial manifold in the transitional turbulence regime of the Navier-Stokes equations.

CHAPTER V

PERIODIC EIGENDECOMPOSITION ALGORITHM

When studying the dimension of an inertial manifold in Sect. 4.2, we have used the information of the Floquet spectra and Floquet vectors of pre-periodic orbits and relative periodic orbits. In this chapter, we discuss how to calculate them accurately.

The Floquet matrix can be naively obtained numerically by integrating (30) along the orbit. However, it is almost certain that this process will overflow or underflow at an exponential rates as the system evolves, or the resulting Jacobian is highly ill-conditioned. Thus, accurate calculation of expansion rate is not trivial for nonlinear systems, especially for those that evolve in high-dimensional spaces. In such cases, the expansion/contraction rates can easily range over many orders of magnitude, which raises a challenge to formulating an effective algorithm to tackle this problem. However, the semi-group property (31) enables us to factorize the Jacobian matrix into a product of short-time matrices with matrix elements of comparable orders of magnitude. So the problem is reduced to calculating the eigenvalues of the product of a sequence of matrices.

In this chapter, we introduce periodic eigendecomposition algorithm, which is designed to calculate the full Floquet spectrum and Floquet vectors. It is based on the covariant vector algorithm (Sect. 1.3.3) and the periodic Schur decomposition (Sect. 1.3.4).

5.1 Description of the problem

According to (31), Jacobian matrix can be integrated piece by piece along a state orbit:

$$J^t(u_0) = J^{t_m - t_{m-1}}(u(t_{m-1}), t_{m-1}) \cdots J^{t_2 - t_1}(u(t_1), t_1) J^{t_1 - t_0}(u(t_0), t_0)$$

with $t_0 = 0$, $t_m = t$ and u_0 the initial point. For periodic orbits, $u(t_m) = u_0$. The time sequence t_i, $i = 1, 2, \cdots, m-1$ is chosen properly such that the elements of the Jacobian matrix associated with each small time interval have a relatively similar order of magnitude. For simplicity, we drop all the parameters above and use a bold letter to denote the product:

$$\mathbf{J}^{(0)} = J_m J_{m-1} \cdots J_1 \,, \quad J_i \in \mathbb{R}^{n \times n},\ i = 1, 2, \cdots, m \,. \tag{159}$$

Let the eigendecomposition of $\mathbf{J}^{(0)}$ be

$$\mathbf{J}^{(0)} = E^{(0)} \Sigma (E^{(0)})^{-1} \,, \tag{160}$$

where Σ is a diagonal matrix which stores $\mathbf{J}^{(0)}$'s eigenvalues (Floquet multipliers), $\{\Lambda_1, \cdots, \Lambda_n\}$, and columns of matrix $E^{(0)}$ are the eigenvectors (Floquet vectors) of $\mathbf{J}^{(0)}$: $E^{(0)} = [\mathbf{e}_1^{(0)}, \cdots, \mathbf{e}_n^{(0)}]$. In this chapter all vectors are written in the column form, transpose of v is denoted $v^\top$, and Euclidean 'dot' product by $(v^\top u)$. The challenge associated with obtaining diagonalized form (160) is the fact that often $\mathbf{J}^{(0)}$ should not be written explicitly since the integration process (30) may overflow or the resulting matrix is highly ill-conditioned. Floquet multipliers can easily vary over hundreds of orders of magnitude, depending on the system under study and the period of the orbit; therefore, all transformations should be applied to the short-time Jacobian matrices J_i individually, instead of working with the full-time $\mathbf{J}^{(0)}$. Also, in order to characterize the geometry along a periodic orbit, not only the Floquet vectors at the initial point are required, but also the sets at each point on the orbit. Therefore, we also desire the eigendecomposition of the cyclic rotations of $\mathbf{J}^{(0)}$: $\mathbf{J}^{(k)} = J_k J_{k-1} \cdots J_1 J_m \cdots J_{k+1}$ for $k = 1, 2, \ldots, m-1$. Eigendecomposition of all $\mathbf{J}^{(k)}$ is called the *periodic eigendecomposition* of the matrix sequence $J_m, J_{m-1}, \cdots, J_1$.

The process of implementing eigendecomposition (160) proceeds in two stages. First, Periodic Real Schur Form (PRSF) is obtained by a similarity transformation for each J_i,

$$J_i = Q_i R_i Q_{i-1}^{\top} \,, \tag{161}$$

with Q_i orthogonal matrix, and $Q_0 = Q_m$. One of R_i above is quasi-upper triangular with $[1\times1]$ and $[2\times2]$ blocks on the diagonal, and the others are all upper triangular. Since the definition of $\mathbf{J}^{(k)}$ is cyclic, we can choose R_m to be quasi-upper triangular without loss of generality. The existence of PRSF, proved in ref. [8], provides the periodic QR algorithm that implements periodic Schur decomposition. Defining $\mathbf{R}^{(k)} = R_k R_{k-1} \cdots R_1 R_m \cdots R_{k+1}$, we have

$$\mathbf{J}^{(k)} = Q_k \mathbf{R}^{(k)} Q_k^{\top} \,, \tag{162}$$

with the eigenvectors of matrix $\mathbf{J}^{(k)}$ related to eigenvectors of quasi-upper triangular matrix $\mathbf{R}^{(k)}$ by orthogonal matrix Q_k. $\mathbf{J}^{(k)}$ and $\mathbf{R}^{(k)}$ have the same eigenvalues, stored in the $[1\times1]$ and $[2\times2]$ blocks on the diagonal of $\mathbf{R}^{(k)}$, and their eigenvectors are transformed by Q_k, so the second stage concerns the eigendecomposition of $\mathbf{R}^{(k)}$. Eigenvector matrix of $\mathbf{R}^{(k)}$ has the same structure as R_m. We evaluate it by two distinct algorithms. The first one is power iteration, while the second algorithm relies on solving a periodic Sylvester equation [44].

As all $\mathbf{R}^{(k)}$ have the same eigenvalues, and their eigenvectors are related by similarity transformations,

$$\mathbf{R}^{(k)} = (R_m \cdots R_{k+1})^{-1} \mathbf{R}^{(0)} (R_m \cdots R_{k+1}) \,, \tag{163}$$

one may be tempted to calculate the eigenvectors of $\mathbf{R}^{(0)}$, and obtain the eigenvectors of $\mathbf{R}^{(k)}$ by (163). The pitfall of this approach is that numerical errors accumulate when multiplying a sequence of upper triangular matrices, especially for large k, such that contracting eigenvectors are contaminated by expanding ones during this process.

Our work illustrates the connection between different algorithms in the two stages of implementing periodic eigendecomposition, pays attention to the case when eigenvectors appear as complex pairs, and demonstrates that eigenvectors can be obtained directly from periodic Sylvester equation without restoring PRSF.

5.2 Stage 1 : periodic real Schur form (PRSF)

This is the first stage of implementing periodic eigendecomposition. Eq. (162) represents the eigenvalues of matrix $\mathbf{J}^{(k)}$ as real eigenvalues on the diagonal, and complex eigenvalue pairs as $[2\times2]$ blocks on the diagonal of $\mathbf{R}^{(k)}$. More specifically, if the ith eigenvalue is real, it is given by the product of all the ith diagonal elements of matrices $R_1, R_2, \cdots, R_m$. In practice, the logarithms of magnitudes of these numbers are added, in order to overcome numerical overflow or underflow. If the ith and $(i+1)$th eigenvalues form a complex conjugate pair, all $[2\times2]$ matrices at position $(i, i+1)$ on the diagonal of $R_1, R_2, \cdots, R_m$ are multiplied with normalization at each step, and the two complex eigenvalues of the product are obtained. There is no danger of numerical overflow or underflow because all these $[2\times2]$ matrices are in the same position and in our applications their elements are of similar order of magnitude. Sect. 1.3.4 introduces the periodic Schur decomposition to achieve PRSF. An alternative is the first two stages of covariant vector algorithm in Sect. 1.3.3, which reduces to simultaneous iteration for periodic orbits. Actually, for a single matrix, simultaneous iteration is equivalent to QR iteration [84]. When it comes to matrix product, simultaneous iteration and periodic Schur decomposition both achieve the PRSF, but their computational complexities differ.

Simultaneous iteration The basic idea of simultaneous iteration is implementing QR decomposition in the process of power iteration. Assume all Floquet multipliers are real, without degeneracy, and order them by their magnitude: $|\Lambda_1| > |\Lambda_2| > \cdots > |\Lambda_n|$, with corresponding normalized Floquet vectors $\mathbf{e}_1, \mathbf{e}_2, \cdots, \mathbf{e}_n$. For simplicity, here we have dropped the upper indices of these vectors. An arbitrary initial vector $\tilde{q}_1 = \sum_{i=1}^{n} \alpha_i^{(1)} \mathbf{e}_i$ will converge to the first Floquet vector $\mathbf{e}_1$ after normalization under power iteration of $\mathbf{J}^{(0)}$,

$$\lim_{\ell\to\infty} \frac{(\mathbf{J}^{(0)})^{\ell} \tilde{q}_1}{||\cdot||} \to q_1 = \mathbf{e}_1 \,.$$

Here $||\cdot||$ denotes the Euclidean norm of the numerator ($||x|| = \sqrt{x^\top x}$). Let $\langle a, b, \cdots, c\rangle$ represent the space spanned by vector $a, b, \cdots, c$ in $\mathbb{R}^n$. Another arbitrary vector $\tilde{q}_2$ is then chosen orthogonal to subspace $\langle q_1\rangle$ by Gram-Schmidt orthonormalization, $\tilde{q}_2 = \sum_{i=2}^{n} \alpha_i^{(2)} [\mathbf{e}_i - (q_1^\top \mathbf{e}_i) q_1]$. Note that the index starts from $i = 2$ because $\langle q_1\rangle = \langle \mathbf{e}_1\rangle$. The strategy now is to apply power iteration of $\mathbf{J}^{(0)}$ followed by orthonormalization in each iteration.

$$\mathbf{J}^{(0)} \tilde{q}_2 = \sum_{i=2}^{n} \alpha_i^{(2)} [\Lambda_i \mathbf{e}_i - \Lambda_1 (q_1^\top \mathbf{e}_i) q_1] = \sum_{i=2}^{n} \alpha_i^{(2)} \Lambda_i [\mathbf{e}_i - (q_1^\top \mathbf{e}_i) q_1] + \sum_{i=2}^{n} \alpha_i^{(2)} (\Lambda_i - \Lambda_1)(q_1^\top \mathbf{e}_i) q_1 \,.$$

The second term in the above expression will disappear after performing Gram-Schmidt orthonormalization to $\langle q_1\rangle$, and the first term will converge to $q_2 = \mathbf{e}_2 - (q_1^\top \mathbf{e}_2) q_1$ (not normalized) after a sufficient number of iterations because of the descending magnitudes of Λ_i, and we also note that $\langle \mathbf{e}_1, \mathbf{e}_2\rangle = \langle q_1, q_2\rangle$. The same argument can be applied to $\tilde{q}_i$, $i = 3, 4, \cdots, n$ as well. In this way, after a sufficient number of iterations,

$$\lim_{\ell\to\infty} (\mathbf{J}^{(0)})^{\ell} [\tilde{q}_1, \tilde{q}_2, \cdots, \tilde{q}_n] \to [q_1, q_2 \cdots, q_n] \,,$$

where

$$q_1 = \mathbf{e}_1 \,, \qquad q_2 = \frac{\mathbf{e}_2 - (\mathbf{e}_2^\top q_1) q_1}{||\cdot||} \,, \qquad \cdots \,, \qquad q_n = \frac{\mathbf{e}_n - \sum_{i=1}^{n-1} (\mathbf{e}_n^\top q_i) q_i}{||\cdot||} \,.$$

Let matrix $Q_0 = [q_1, q_2, \cdots, q_n]$; then we have $\mathbf{J}^{(0)} Q_0 = Q_0 \mathbf{R}^{(0)}$ with $\mathbf{R}^{(0)}$ an upper triangular matrix because of $\langle q_1, q_2, \cdots, q_i\rangle = \langle \mathbf{e}_1, \mathbf{e}_2, \cdots, \mathbf{e}_i\rangle$, which is just $\mathbf{J}^{(0)} = Q_0 \mathbf{R}^{(0)} Q_0^\top$ (the Schur decomposition of $\mathbf{J}^{(0)}$). The diagonal elements of $\mathbf{R}^{(0)}$ are the eigenvalues of $\mathbf{J}^{(0)}$ in decreasing order. Numerically, the process described above can be implemented on an arbitrary initial full rank matrix $\tilde{Q}_0$ followed by QR decomposition at each step

$$J_s \tilde{Q}_{s-1} = \tilde{Q}_s \tilde{R}_s \tag{164}$$

with $s = 1, 2, 3, \cdots$ and $J_{s+m} = J_s$. For a sufficient number of iterations, $\tilde{Q}_s$ and $\tilde{R}_s$ converge to Q_s and R_s in (161) for $s = 1, 2, \cdots, m$, so we achieve (162) the periodic Schur decomposition of $\mathbf{J}^{(k)}$.

We have thus demonstrated that simultaneous iteration converges to PRSF for real non-degenerate eigenvalues. For complex eigenvalue pairs, the algorithm converges in the sense that the subspace spanned by a complex conjugate vector pair converges. So,

$$\mathbf{J}^{(0)}Q_0 = Q_0^{'}\mathbf{R}^{(0)} = Q_0 D\mathbf{R}^{(0)} \,, \tag{165}$$

where D is a block-diagonal matrix with diagonal elements ± 1 (corresponding to real eigenvalues) or $[2\times 2]$ blocks (corresponding to complex eigenvalue pairs). Absorb D into R_m, then R_m becomes a quasi-upper triangular matrix, and (161) still holds. Here, we focus on Q_0 instead of $Q_1, \cdots, Q_{m-1}$ because we assume R_m is quasi-upper triangular in (161).

5.3 Stage 2 : eigenvector algorithms

Upon achieving PRSF, the eigenvectors of $\mathbf{J}^{(k)}$ are related to the eigenvectors of $\mathbf{R}^{(k)}$ by orthogonal matrix Q_k from (161), and the eigenvector matrix of $\mathbf{R}^{(k)}$ has the same quasi-upper triangular structure as R_m. In addition, if we follow the simultaneous iteration method or implement periodic Schur decomposition without shift, eigenvalues are ordered by their magnitudes on the diagonal. Power iteration utilizing this property could be easily implemented to generate the eigenvector matrix. This is the basic idea of the first algorithm for generating eigenvectors of $\mathbf{R}^{(k)}$, corresponding to the 3rd and 4th stage in covariant vector algorithm in Figure 3. Alternatively, observation that the first eigenvector of $\mathbf{R}^{(k)}$ is trivial if it is real, $v_1 = (1, 0, \cdots, 0)^{\top}$, inspires us to reorder the eigenvalues so that the jth eigenvalue is in the first diagonal place of $\mathbf{R}^{(k)}$; in this way, the jth eigenvector is obtained. For both methods, attention should be paid to the complex conjugate eigenvector pairs. In this section, $v_i^{(k)}$ denotes the ith eigenvector of $\mathbf{R}^{(k)}$, contrast to $\mathbf{e}_i^{(k)}$ the eigenvectors of $\mathbf{J}^{(k)}$, and for most cases, the upper indices are dropped if no confusion occurs.

5.3.1 Iteration method

The prerequisite for iteration method is that all the eigenvalues are ordered in an ascending or descending way by their magnitude on the diagonal of $\mathbf{R}^{(k)}$. Assume that they are in descending order, which is the outcome of simultaneous iteration; therefore, the diagonal elements of $\mathbf{R}^{(k)}$ are $\Lambda_1, \Lambda_2, \cdots, \Lambda_n$, with magnitudes from large to small. If the ith eigenvector of $\mathbf{R}^{(k)}$ is real, then it has form $v_i = (a_1, a_2, \cdots, a_i, 0, \cdots, 0)^{\top}$. An arbitrary vector whose first i elements are non-zero $x = (b_1, b_2, \cdots, b_i, 0, \cdots, 0)^{\top}$ is a linear combination of the first i eigenvectors: $x = \sum_{j=1}^{i} \alpha_j v_j$. Use it as the initial condition for the power iteration by $(\mathbf{R}^{(k)})^{-1} = R_{k+1}^{-1} \cdots R_m^{-1} R_1^{-1} R_2^{-1} \cdots R_k^{-1}$ and after a sufficient number of iterations,

$$\lim_{\ell\to\infty} \frac{(\mathbf{R}^{(k)})^{-\ell} x}{||\cdot||} = v_i \,. \tag{166}$$

The property we used here is that $(\mathbf{R}^{(k)})^{-1}$ and $\mathbf{R}^{(k)}$ have the same eigenvectors but inverse eigenvalues. Moreover, matrix sequence $R_{k+1}^{-1} \cdots R_m^{-1} R_1^{-1} R_2^{-1} \cdots R_k^{-1}$ is applied sequentially in (166), so if the ith eigenvector $v_i^{(k)}$ of $(\mathbf{R}^{(k)})^{-1}$ converges, then the ith eigenvector of $(\mathbf{R}^{(k-1)})^{-1}$ is obtained by $v_i^{(k-1)} = R_k^{-1} v_i^{(k)}$ (need to be normalized). Therefore, the ith eigenvectors of $(\mathbf{R}^{(k)})$ for $k = 0, 1, \cdots, m$ are obtained almost simultaneously. Note, there is no numerical instability here as in (163) because (166) finds the most expanding direction in the subspace that only the first i elements are non-zero.

For a $[2\times 2]$ block on the diagonal of $\mathbf{R}^{(k)}$, the corresponding conjugate complex eigenvectors form a two-dimensional subspace. Any real vector selected from this subspace will rotate under power iteration. In this case, power iteration still converges in the sense that the subspace spanned by the complex conjugate eigenvector pair converges. Suppose the ith and $(i+1)$th eigenvectors of $\mathbf{R}^{(k)}$ form a complex pair. Two arbitrary vectors x_1 and x_2 whose first $i+1$ elements are non zero can be written as the linear superposition of the first $i+1$ eigenvectors, $x_{1,2} = (\sum_{j=1}^{i-1} \alpha_j^{(1,2)} v_j) + \alpha_i^{(1,2)} v_i + (\alpha_i^{(1,2)} v_i)^*$, where $(*)$ denotes the complex conjugate. As for the real case, the first $i-1$ components will vanish after a sufficient number of iterations. Denote the two vectors at this instance to be $X_{1,2}$ and form matrix $X = [X_1, X_2]$. The subspace spanned by $X_{1,2}$ does not change and X will be rotated after another iteration,

$$(\mathbf{R}^{(k)})^{-1} X = X' = XC\,, \tag{167}$$

where C is a $[2\times 2]$ matrix which has two complex conjugate eigenvectors v_C and $(v_C)^*$. Transformation (167) relates the eigenvectors of $\mathbf{R}^{(k)}$ with those of C: $[v_i, (v_i)^*] = X[v_C, (v_C)^*]$. In practice, matrix C can be computed by QR decomposition; let $X = Q_X R_X$ be the QR decomposition of X, then $C = R_X^{-1} Q_X^\top X'$. On the other hand, complex eigenvectors are not uniquely determined in the sense that $e^{i\theta} v_i$ is also an eigenvector with the same eigenvalue as v_i for an arbitrary phase θ, so when comparing results from different eigenvector algorithms, we need a constraint to fix the phase of a complex eigenvector, such as letting the first element be real.

We should note that the performance of power iteration depends on the ratios of magnitudes of eigenvalues, so performance is poor for systems with clustered eigenvalues. We anticipate that proper modifications, such as shifted iteration or inverse iteration [84], may help improve the performance. Such techniques are beyond the scope of this paper.

5.3.2 Reordering method

There exists a direct algorithm to obtain the eigenvectors of every $\mathbf{R}^{(k)}$ at once without iteration. The idea is very simple: the eigenvector corresponding to the first diagonal element of an upper-triangular matrix is $v_1 = (1, 0, \cdots, 0)^\top$. By reordering the diagonal elements (or $[2\times 2]$ blocks) of $\mathbf{R}^{(0)}$, we can find any eigenvector by positioning the corresponding eigenvalue in the first diagonal position. Although in our application only reordering of $[1\times 1]$ and $[2\times 2]$ blocks is needed, we recapitulate here the general case of reordering two adjacent blocks of a quasi-upper triangular matrix following Granat *et al.* [44]. Partition R_i as

$$R_i = \left[\begin{array}{c|cc|c} R_i^{00} & * & * & * \\ \hline 0 & R_i^{11} & R_i^{12} & * \\ 0 & 0 & R_i^{22} & * \\ \hline 0 & 0 & 0 & R_i^{33} \end{array}\right] ,$$

where $R_i^{00}, R_i^{11}, R_i^{22}, R_i^{33}$ have size $[p_0\times p_0], [p_1\times p_1], [p_2\times p_2]$ and $[p_3\times p_3]$ respectively, and $p_0+p_1+p_2+p_3 = n$. In order to exchange the middle two blocks (R_i^{11} and R_i^{22}), we construct a non-singular periodic matrix sequence: $\hat{S}_i$, $i = 0, 1, 2, \cdots, m$ with $\hat{S}_0 = \hat{S}_m$,

$$\hat{S}_i = \left[\begin{array}{c|c|c} I_{p_0} & 0 & 0 \\ \hline 0 & S_i & 0 \\ \hline 0 & 0 & I_{p_3} \end{array}\right] ,$$

where S_i is a $[(p_1+p_2)\times(p_1+p_2)]$ matrix, such that $\hat{S}_i$ transforms R_i as follows:

$$\hat{S}_i^{-1} R_i \hat{S}_{i-1} = \tilde{R}_i = \left[\begin{array}{c|cc|c} R_i^{00} & * & * & * \\ \hline 0 & R_i^{22} & 0 & * \\ 0 & 0 & R_i^{11} & * \\ \hline 0 & 0 & 0 & R_i^{33} \end{array}\right], \tag{168}$$

which is

$$S_i^{-1} \left[\begin{array}{cc} R_i^{11} & R_i^{12} \\ 0 & R_i^{22} \end{array}\right] S_{i-1} = \left[\begin{array}{cc} R_i^{22} & 0 \\ 0 & R_i^{11} \end{array}\right].$$

The problem is to find the appropriate matrices S_i which satisfy the above condition. Assume S_i has form

$$S_i = \left[\begin{array}{cc} X_i & I_{p_1} \\ I_{p_2} & 0 \end{array}\right],$$

where matrix X_i has dimension $[p_1 \times p_2]$. We obtain periodic Sylvester equation [44]

$$R_i^{11} X_{i-1} - X_i R_i^{22} = -R_i^{12}, \quad i = 0, 1, 2, \cdots, m. \tag{169}$$

The algorithm to find eigenvectors is based on (169). If the ith eigenvalue of $\mathbf{R}^{(k)}$ is real, we only need to exchange the leading $[(i-1)\times(i-1)]$ block of R_k, $k = 1, 2, \cdots, m$ with its ith diagonal element. If the ith and $(i+1)$th eigenvalues form a complex conjugate pair, then the leading $[(i-1)\times(i-1)]$ block and the following $[2\times 2]$ block should be exchanged. Therefore X_i in (169) has dimension $[p_1 \times 1]$ or $[p_1 \times 2]$. In both cases, $p_0 = 0$.

Real eigenvectors In this case, matrix X_i is just a column vector, so (169) is equivalent to

$$\left[\begin{array}{cccccc} R_1^{11} & -R_1^{22} I_{p_1} & & & & \\ & R_2^{11} & -R_2^{22} I_{p_1} & & & \\ & & R_3^{11} & -R_3^{22} I_{p_1} & & \\ & & & \ddots & \cdots & \\ -R_m^{22} I_{p_1} & & & & & R_m^{11} \end{array}\right] \left[\begin{array}{c} X_0 \\ X_1 \\ X_2 \\ \cdots \\ X_{m-1} \end{array}\right] = \left[\begin{array}{c} -R_1^{12} \\ -R_2^{12} \\ -R_3^{12} \\ \cdots \\ -R_m^{12} \end{array}\right], \tag{170}$$

where R_i^{22} is the (p_1+1)th diagonal element of R_i. The accuracy of eigenvectors is determined by the accuracy of solving sparse linear equation (170). In our application to periodic orbits in the one-dimensional Kuramoto-Sivashinsky equation, Gaussian elimination with partial pivoting is enough. For a more technical treatment, such as cyclic reduction or preconditioned conjugate gradients, to name a few, please see [1, 30, 45].

Now we get all vectors X_i by solving periodic Sylvester equation, but how are they related to the eigenvectors? In analogy to $\mathbf{R}^{(0)}$, defining $\tilde{\mathbf{R}}_0 = \tilde{R}_m \tilde{R}_{m-1} \cdots \tilde{R}_1$, we get $\hat{S}_m^{-1} \mathbf{R}^{(0)} \hat{S}_m = \tilde{\mathbf{R}}_0$ by (168). Since $p_0 = 0$ and $p_2 = 1$ in (168), the first eigenvector of $\tilde{\mathbf{R}}_0$, the one corresponding to eigenvalue Λ_{p_1+1} is $\tilde{e} = (1, 0, \cdots, 0)^\top$. Apart from normalization, the corresponding eigenvector of $\mathbf{R}^{(0)}$ is

$$v_{p_1+1}^{(0)} = \hat{S}_m \tilde{e} = \left[X_0^\top, 1, 0, 0, \cdots, 0\right]^\top.$$

This is the eigenvector of matrix $\mathbf{R}^{(0)} = R_m R_{m-1} \cdots R_1$ in (162) for $k = 0$. For $\mathbf{R}^{(1)} = R_1 R_m \cdots R_2$, the corresponding periodic Sylvester equation will be cyclically rotated one row up in (170), which means X_1 will be shifted to the first place, and thus the corresponding eigenvector of $\mathbf{R}^{(1)}$ is $v^{(1)}_{p_1+1} = [X_1^\top, 1, 0, \cdots, 0]^\top$. The same argument goes for all the remaining $\mathbf{R}^{(k)}$. In conclusion, solution of (170) contains the eigenvectors for all $\mathbf{R}^{(k)}, k = 0, 1, \cdots, m-1$. Another benefit of reordering method is that we can selectively get the eigenvectors corresponding to some specific eigenvalues. This merit is important in high-dimensional nonlinear systems for which only a subset of Floquet vectors suffices to characterize the dynamics in tangent space, and thus we avoid wasting time in calculating the remaining unimportant subset.

Complex eigenvector pairs As in the real eigenvalue case, we have $p_0 = 0$, but now $p_2 = 2$, so matrix X_i has dimension $[p_1 \times 2]$. Using the same notation as ref. [44], let $v(X_i)$ denote the vector representation of X_i with the columns of X_i stacked on top of each other, and let $A \otimes B$ denote the Kronecker product of two matrices, with the (i, j)-block element be $a_{ij} B$.

Now, the periodic Sylvester equation (169) is equivalent to

$$\begin{bmatrix} I_2 \otimes R_1^{11} & -(R_1^{22})^\top \otimes I_{p_1} & & & \\ & I_2 \otimes R_2^{11} & -(R_2^{22})^\top \otimes I_{p_1} & & \\ & & I_2 \otimes R_3^{11} & -(R_3^{22})^\top \otimes I_{p_1} & \\ & & & \ddots & \cdots \\ -(R_m^{22})^\top \otimes I_{p_1} & & & & I_2 \otimes R_m^{11} \end{bmatrix} \begin{bmatrix} v(X_0) \\ v(X_1) \\ v(X_2) \\ \cdots \\ v(X_{m-1}) \end{bmatrix} = \begin{bmatrix} -v(R_1^{12}) \\ -v(R_2^{12}) \\ -v(R_3^{12}) \\ \cdots \\ -v(R_m^{12}) \end{bmatrix} . \tag{171}$$

After switching R_i^{11} and R_i^{22}, we can get the first two eigenvectors of $\tilde{\mathbf{R}}_0$ by multiplying the first $[2 \times 2]$ diagonal blocks of $\tilde{R}_i$: $R^{22} = R_m^{22} R_{m-1}^{22} \cdots R_1^{22}$. Let the eigenvectors of R^{22} be v and v^* of size $[2 \times 1]$, then the corresponding eigenvectors of $\tilde{\mathbf{R}}_0$ are $\tilde{e}_1 = (v^\top, 0, 0, \cdots, 0)^\top$ and $\tilde{e}_2 = (\tilde{e}_1)^*$ (the additional zeros make the length of the eigenvectors be n). Therefore, the corresponding eigenvectors of $\mathbf{R}^{(0)}$ are

$$\left[v^{(0)}_{p_1+1}, v^{(0)}_{p_1+2} \right] = \hat{S}_m [\tilde{e}_1, \tilde{e}_2] = \begin{bmatrix} X_0 \\ I_2 \\ 0 \quad 0 \\ 0 \quad 0 \\ \vdots \\ 0 \quad 0 \end{bmatrix} [v, v^*] \,.$$

For other $\mathbf{R}^{(k)}$, the same argument in the real case applies here too, so we obtain all the complex eigenvector pairs for $\mathbf{R}^{(k)}, k = 1, 2, \cdots, m$.

5.4 Computational complexity and convergence analysis

In this section, we make no attempt at conducting a strict error analysis of the algorithms presented. However, for practical applications, it is important to understand their computational costs. Periodic eigendecomposition is conducted in two stages: (1) PRSF, and (2) determination of all eigenvectors. In each stage, there are two candidate algorithms, so the efficiency of periodic eigendecomposition depends on the choice of the specific algorithm chosen in each stage.

Periodic Schur decomposition algorithm and simultaneous iteration are both effective to achieve PRSF. We estimate the complexity of periodic Schur decomposition algorithm in analogy with the single matrix case. For a single $[n \times n]$ matrix, $O(n^3)$ flops (floating-point operations) are required [84] to reduce it to upper Hessenberg form. Accordingly, the first stage in Figure 4 takes $O(mn^3)$ flops. Then the implicit QR iteration process for a single matrix takes $O(n^2)$ flops for a single iteration, so each iteration of the second stage in Figure 4 takes $O(mn^2)$ flops. Usually, the number of iterations exceeds by far the dimension of the matrix. Therefore, the average complexity of one iteration in periodic Schur decomposition algorithm is $O(mn^2)$. For a detailed discussion see [8, 84]. On the other hand, simultaneous iteration (164) requires m QR decomposition $O(mn^3)$ and m matrix-matrix multiplication $O(mn^3)$ in each iteration, giving a total computational cost of $O(mn^3)$. Moreover, the convergence of both algorithms depends linearly on the ratio of adjacent eigenvalues of $\mathbf{R}^{(0)}$: $|\Lambda_i|/|\Lambda_{i+1}|$ without shift [37]. Therefore, the ratio of costs between periodic Schur decomposition algorithm and simultaneous iteration is approximately of the order $O(mn^2)/O(mn^3) = O(1/n)$, implying that the periodic Schur decomposition algorithm is much cheaper than the simultaneous iteration if the dimension of matrices involved is large.

The second stage of periodic eigendecomposition is to find all the eigenvectors of $\mathbf{J}^{(k)}$ via quasi-upper triangular matrices $\mathbf{R}^{(k)}$. The first candidate is power iteration. The computational cost of one iteration (166) for the ith eigenvector is $O(mi^2)$. The second candidate, reordering method, relies on an effective method to solve periodic Sylvester equation (169). For example, Gaussian elimination with partial pivoting is suitable for well-conditioned matrix (170) and (171) with a computational cost of $O(mi^2)$ for the ith eigenvector. Here, we have taken account of the sparse structure of (170) and (171). For a detailed discussion, see ref. [44]. So, the total complexity of reordering method is approximately the same as that of one iteration in power iteration.

In summary, if we only consider the computational complexity, the combination of periodic Schur decomposition algorithm and reordering method is preferable for periodic eigendecomposition.

5.5 *Application to Kuramoto-Sivashinsky equation*

Our ultimate goal of implementing periodic eigendecomposition is to analyze the stability of periodic orbits and the associated stable/unstable manifolds in dynamical systems, for the hope of getting a better understanding of pattern formation and turbulence. As an example, we focus on the one-dimensional Kuramoto-Sivashinsky equation(134) and its Fourier space form (135). We follow Sect. 3.1 to integrate this system. For the calculation of Floquet spectrum and vectors, we use the combination of periodic Schur decomposition algorithm and reordering algorithm. In addition, Gaussian elimination with partial pivoting is stable for solving (170) and (171) if the time step in Kuramoto-Sivashinsky integrator is not too large.

Here we show how well periodic eigendecomposition works by applying it to one representative preperiodic orbit $\overline{ppo}_{10.25}$ (the 1st subplot in Figure 15) and two relative periodic orbits $\overline{rpo}_{16.31}$ (the 4th subplot in Figure 15) and $\overline{rpo}_{57.60}$ which is documented in ref. [21].

5.5.1 Accuracy

Table 7 shows that the 2nd and 3rd, respectively 3rd and 4th exponents of $\overline{rpo}_{16.31}$, respectively $\overline{ppo}_{10.25}$, are marginal. Even though the inaccuracy of the closure of the orbit contributes to the error, we note that the absolute error takes values as low as 10^{-12}. Table 7 and Figure 17 show that periodic Schur decomposition is capable of resolving Floquet multipliers differing by thousands of orders of magnitude: when using $N = 64$ Fourier modes, the smallest Floquet multiplier magnitude for $\overline{ppo}_{10.25}$ is $|\Lambda_{62}| \simeq e^{-6080.4 \times 10.25} \simeq 10^{-27067}$. This cannot be achieved if we try to compute a single Jacobian matrix for the whole orbit.

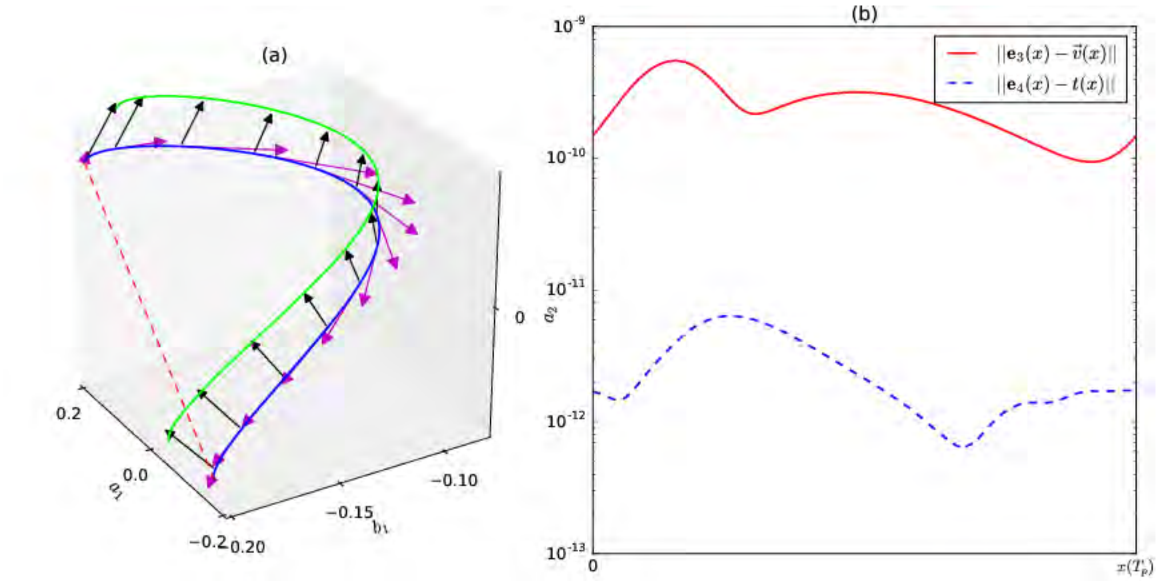

Figure 28: Marginal vectors and the associated errors. (a) $\overline{ppo}_{10.25}$ in one period projected into $[b_1, c_1, b_2]$ subspace (blue curve), and its counterpart (green line) generated by a small group transformation $g(\phi)$, here arbitrarily set to $\phi = 0.1$. Magenta and black arrows represent the first and the second marginal Floquet vectors $\mathbf{e}_3(x)$ and $\mathbf{e}_4(x)$ along the prime orbit. (b) The solid red curve is the Euclidean difference between $\mathbf{e}_3(x)$ and the velocity field $v(x)$ along the orbit, and the blue dashed curve is the difference between $\mathbf{e}_4(x)$ and the group tangent $t(x) = \mathbf{T}x$.

The two marginal directions have a simple geometrical interpretation and provide a metric for us to measure the convergence of periodic eigendecomposition. Figure 28 (a) depicts the two marginal vectors of $\overline{ppo}_{10.25}$ projected into the subspace spanned by $[b_1, c_1, b_2]$ (the real, imaginary parts of the first mode and the real part of the second Fourier mode). The first marginal direction (the 3rd Floquet vector in Table 7) is aligned with the velocity field along the orbit, and the second marginal direction (the 4th Floquet vector) is aligned with the group tangent. The numerical difference between the unit vectors along these two marginal directions and the corresponding physical directions is shown in Figure 28 (b). The difference is under 10^{-9} and 10^{-11} for these two directions, which demonstrates the accuracy of the algorithm. As shown in Table 7, for a preperiodic orbit, such as $\overline{ppo}_{10.25}$, the velocity field and the group tangent have eigenvalue +1 and −1 respectively, and are thus distinct. However, the two marginal directions are degenerate for a relative periodic orbit, such as $\overline{rpo}_{16.31}$. So these two directions are not fixed, but the two-dimensional plane spanned by them is uniquely determined. Figure 29 shows that the velocity field and group tangent along orbit $\overline{rpo}_{16.31}$ indeed lie in the subspace spanned by these two marginal directions.

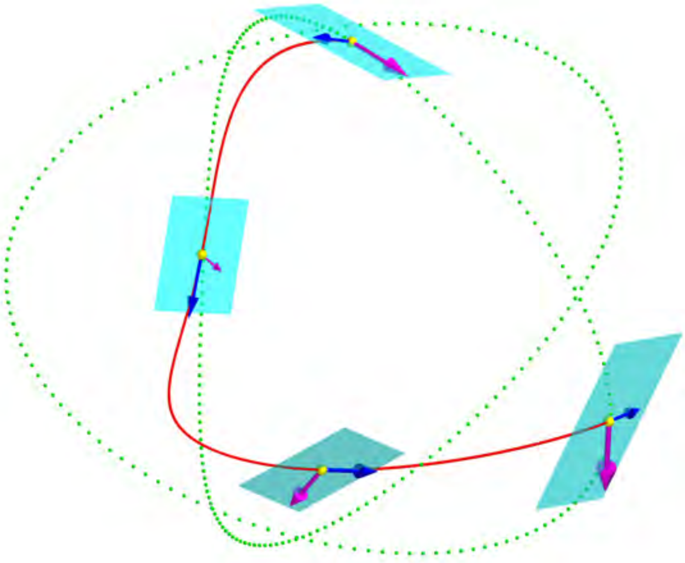

Figure 29: Projection of relative periodic orbit $\overline{rpo}_{16.31}$ into the Fourier modes subspace $[b_2, c_2, b_3]$ (red curve). The dotted curve (lime) is the group orbit connecting the initial and final points. Blue and magenta arrows represent the velocity field and group tangent along the orbit, respectively. Two-dimensional planes (cyan) are spanned by the two marginal Floquet vectors at each point (yellow) along the orbit.

5.5.2 The choice of the number of orbit segments

We have noted above that the semi-group property of Jacobian matrix (31) enables us to factorize $\mathbf{J}^{(k)}$ into a product of short-time matrices with matrix elements of comparable order of magnitude. In practice, caution should be exercised when trying to determine the optimal number of time increments that the orbit should be divided into. If the number of time increments m is too large, then, according to the estimates of Sect. 5.4, the computation may be too costly. If m is too small, then the elements of the Jacobian matrix corresponding to the corresponding time increment may range over too many orders of magnitude, causing periodic eigendecomposition to fail to resolve the most contracting Floquet vector along the orbit. One might also vary the time step according to the velocity at a given point on the orbit. Here we determined satisfactory m's by numerical experimentation shown in Figure 30. Since larger time step means fewer time increments of the orbit, a very small time step ($h_0 \approx 0.001$) is chosen as the base case, and it is increased to test whether the corresponding Floquet exponents change substantially or not. As shown in Figure 30 (a), up to $6h_0$ the whole Floquet spectrum varies within 10^{-12} for both $\overline{ppo}_{10.25}$ and $\overline{rp}_{57.60}$. These two orbits represent two different types of invariant solutions which have short and long periods respectively, so we presume that time step $6h_0$ is good enough for other short or long orbits too. On the other hand, if only the first few Floquet exponents are desired, the time step can be increased further to fulfill the job. As shown in Figure 30 (b), if we are only interested in the first 35 Floquet exponents, then time step $30h_0$ is small enough. In high-dimensional nonlinear systems, often we are not interested in very contraction directions

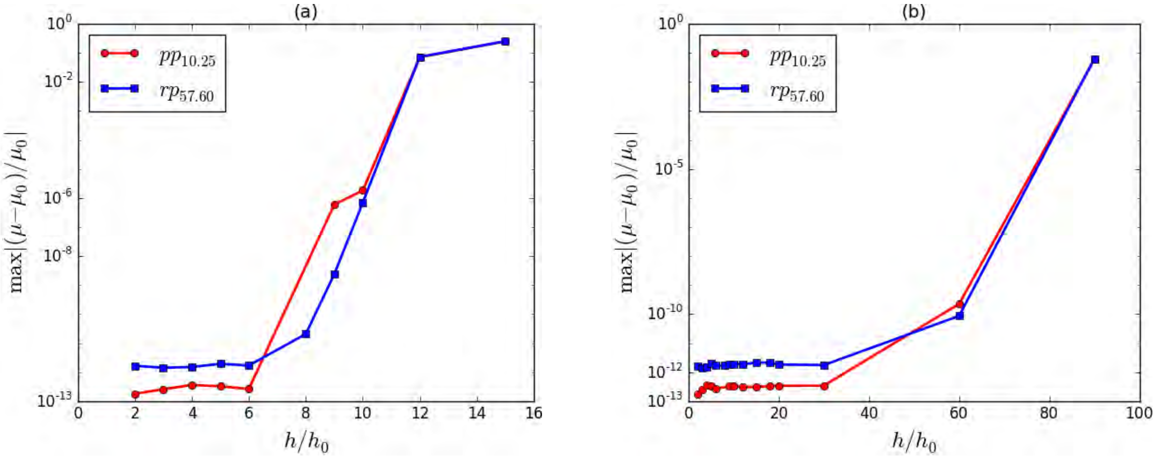

Figure 30: Relative error of the real part of Floquet exponents associated with different time steps with which the Floquet matrix is integrated. Two orbits $\overline{ppo}_{10.25}$ and $\overline{rpo}_{57.60}$ are used as an example with the base case $h_0 \approx 0.001$. (a) The maximal relative difference of the whole set of Floquet exponents with increasing time step (decreasing the number of ingredient segments of the orbit). (b) Only consider the first 35 Floquet exponents.

because dynamics in these directions are transient and shed little insight into the system properties. Therefore, large time step could be used to save time.

5.6 Conclusion and future work

In this chapter we have used the one-dimensional Kuramoto-Sivashinsky system to illustrate the effectiveness of periodic eigendecomposition applied to stability analysis in dissipative nonlinear systems. In future, we hope to apply the method to the study of orbits of much longer periods, as well as to the study of high-dimensional numerically exact time-recurrent unstable solutions of the full Navier-Stokes equations. We anticipate the need for optimizing and parallelizing such algorithms. Also, if periodic eigendecomposition is to be applied to Hamiltonian systems, additional adjustments will be required to guarantee the preservation of symmetries of Floquet spectrum imposed by the symplectic structure of Hamiltonian flows.

CHAPTER VI

CONCLUSION AND FUTURE WORK

In this thesis, we have investigated the dimension of the inertial manifold in the one-dimensional Kuramoto-Sivashinsky equation and determined that the dimension is 8 for domain size 22. In order to reach this conclusion, we had to develop a number of theoretical and numerical tools. Here, we summarize the contributions of this thesis in two categories, theoretical and numerical contributions, and discuss open future directions.

6.1 Theoretical contributions

In Sect. 2.2.2, we define the projection operator from full state space to the slice. Also, in Sect. 2.2.3, we give the precise relation between the in-slice Jacobian and the Jacobian in the full state space. Therefore, in-slice stability eigenvectors can be obtained easily from those in the full state space.

In Sect. 3.5.1, we reduce the O(2) symmetry by using the fundamental domain and argue that defining the 1st mode slice to have vanishing real part of the first Fourier mode will keep the reflection rule unchanged in the slice. Such a simplification can be adopted in other systems with O(2) symmetry too, such as complex Ginzburg-Landau equation.

In Sect. 4.2, we use three different numerical approaches, i.e., local Floquet exponents, principal angles obtained by Floquet vectors, and expansion errors of difference vectors in shadowing incidences, to estimate the dimension of the inertial manifold in one-dimensional Kuramoto-Sivashinsky equation. The results are consistent among all these three approaches and with the previous research on covariant Lyapunov vectors conducted on ergodic trajectories.

6.2 Numerical contributions

In Chapter 5, we provide a detailed description of the periodic eigendecomposition needed to calculate the stability of periodic orbits of a chaotic system. Its effectiveness and accuracy are tested in the one-dimensional Kuramoto-Sivashinsky equation in Sect. 5.5. The `C++` implementation can be found at my GitHub repository github.com/dingxiong/research.

This repository also contains the `C++` implementation of some other algorithms that are frequently used in the study of chaotic systems, such as GMRES [74] to solve linear equation $Ax = b$ by Krylov subspace iteration, Levenberg-Marquardt algorithm [59, 62], inexact Newton backtracking method [77], Newton-GMRES-Hookstep algorithm [15] to find (relative) periodic orbits, and the integrator for the one-dimensional Kuramoto-Sivashinsky equation.

6.3 Future work

In this section, I list two potential directions for the future research in this field.

6.3.1 Spatiotemporal averages in Kuramoto-Sivashinsky equation

We have gained valuable intuition about the geometrical structure of the global attractor by the experience of working with these shadowing cases in Sect. 3.5. We observe that the global attractor has a very thin structure. Orbits can shadow the unstable manifold of E_2 and different orbits can shadow each other. Experience with such shadowing incidences helps us choose appropriate Poincaré sections to capture the transition rules between different subregions. One is in a position to investigate the symbolic dynamics of the system. Namely, one can try to partition the fundamental domain into several subregions and figure out the transition rule between different subregions. This transition rule, also called the symbolic dynamics, helps us classify the over 60 000 pre/relative periodic orbits by their topological lengths. Then the spectral determinant (73) could be accurately approximated by the shortest pre/relative periodic orbits. If this is implemented, spatiotemporal averages could be obtained efficiently, without longtime simulations.

6.3.2 The dimensions of inertial manifolds of other systems

We believe that the numerical techniques developed in Chapter 4 can be used to determine the dimensions of inertial manifolds for other nonlinear dissipative dynamical systems. The previous studies [79, 89, 90], based on covariant vectors, have estimated the dimension of the inertial manifold of the one-dimensional complex Ginzburg-Landau equation,

$$A_t = A + (1 + i\alpha)A_{xx} - (1 + i\beta)|A|^2 A\,,$$

where $A(x, t)$ is a complex field, and α and β are real parameters. As shown in Figure 31, one-dimensional complex Ginzburg-Landau equation exhibits spatiotemporal chaos similar to the Kuramoto-Sivashinsky Figure 11. We believe (but have not carried out the requisite computations) that the analysis based on relative periodic orbits will also in this case determine the dimension of inertial manifold. Similar to the one-dimensional Kuramoto-Sivashinsky equation, this equation has a spatial reflection symmetry $A(x, t) \to A(-x, t)$ and SO(2)×SO(2) spatial and phase translational symmetries $A(x, t) \to e^{i\phi}A(x+\ell, t)$. Thus the symmetry-reduction techniques discussed in Sect. 2.2 can also be applied here, and one can restrict the analysis to a fundamental domain in a slice, as we did in Sect. 3.5.1. In two pubications not reported in detail in this thesis [25, 26], we have constructed a "minimal" spatial domain and have determined a variety of equilibria, relative equilibria, and relative periodic orbits for this system. This sets the stage for application of methods discussed in Sect. 4.2, i.e., evaluation of local Floquet exponents, principal angles among sets of Floquet vectors, and expansion errors of difference vectors during close shadowing episodes, in order to estimate dimensions of the inertial manifold in system of complex Ginzburg-Landau type.

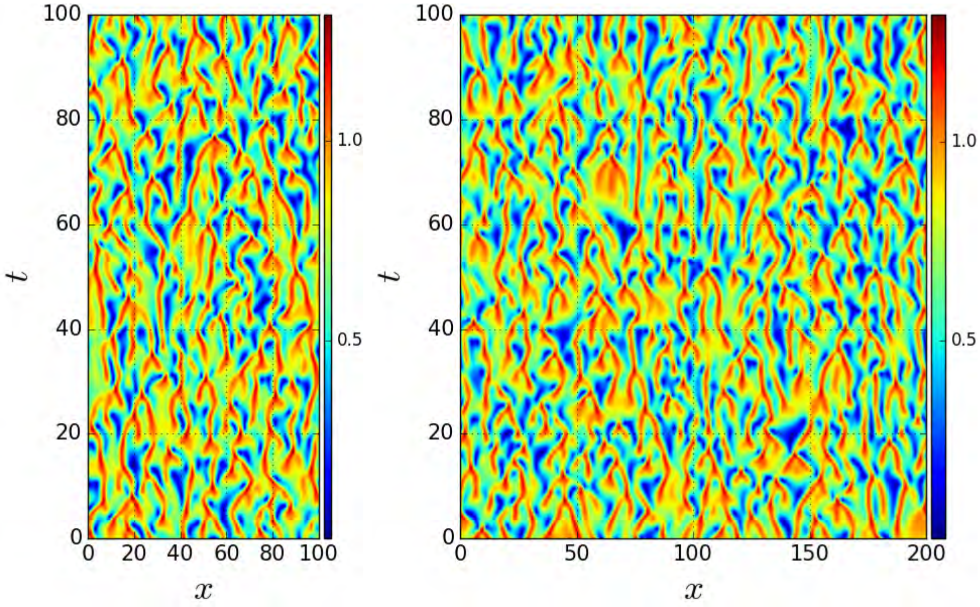

Figure 31: Spatiotemporal plots of complex Ginzburg-Landau equation with $\alpha = 2$ and $\beta = -2$ for two different domain sizes $L = 100$ and 200. The color represents the magnitude of the field $|A(x,t)|$. Random initial condition is used, with the initial transient discarded. Compare with Figure 11.

APPENDIX A

FLOQUET THEOREM AND PERIODIC ORBITS

A linear ordinary differential equation with periodic coefficients is an old topic. Solutions of such type of equations can be decomposed into the product of a time-exponential part and a bounded periodic part. The rigorous statement is given by

Theorem A.1 *[32] If $\Phi(t)$ is a fundamental matrix solution of linear system $\dot{x} = A(t)x$ with periodic coefficients $A(t+T) = A(t)$, T being the period, then $\Phi(t)$ can be decomposed as*

$$\Phi(t) = P(t)e^{tB} \quad \textit{with} \quad P(t) = P(t+T)\,.$$

Here $P(t)$ is called monodromy matrix, and B is a constant matrix. Eigenvalues of B are called Floquet exponents. The eigenvectors are called Floquet vectors.

The proof of this theorem is very simple. First, it is easy to see that if $\Phi(t)$ is solution matrix, so is $\Phi(t+T)$. Their relation is given by $\Phi(t+T) = \Phi(t)C(t,T)$, where $C(t,T) = \Phi^{-1}(t)\Phi(t+T)$. Second, $C(t,T)$ is independent of time which can be shown by taking time derivative at both sides of $\Phi(t)C(t,T) = \Phi(t+T)$,

$$\begin{aligned} &\dot{\Phi}(t)C(t,T) + \Phi(t)\dot{C}(t,T) = \dot{\Phi}(t+T) \\ \Longrightarrow\ &A(t)\Phi(t)C(t,T) + \Phi(t)\dot{C}(t,T) = A(t+T)\Phi(t+T) \\ \Longrightarrow\ &\dot{C}(t,T) = 0\,. \end{aligned}$$

So matrix $C(T)$ is only parametrized by the period. Furthermore,

$$C(nT) = \prod_{k=0}^{n-1} \left(\Phi^{-1}(t+kT)\,\Phi(t+(k+1)T)\right) = C(T)^n\,;$$

thus $C(T)$ has form e^{TB}, where B is a constant matrix. So $\Phi(t+T) = \Phi(t)e^{TB}$. Last, If we define a new matrix $P(t) = \Phi(t)e^{-tB}$, then

$$P(t+T) = \Phi(t+T)e^{-TB-tB} = \Phi(t)e^{-tB} = P(t)\,.$$

In this way, we decompose the fundamental matrix solution into a periodic part $P(t)$ and a time exponential part e^{tB}, even though we do not know the explicit form of $P(t)$.

Floquet theorem in condensed matter physics is under another name: **Bloch theorem**, which states that wave function in a periodic potential can be written as $\psi(\vec{r}) = e^{i\vec{k}\cdot\vec{r}}u(\vec{r})$. Here $u(\vec{r})$ is a periodic function with the same potential period. Eigenstates are classified into different bands by different profiles of $u(\vec{r})$.

For our interest, dynamics in the tangent space in a nonlinear dynamical system is governed by $\dot{J} = AJ$. Especially, for periodic orbits, A is periodic, and if we start with $J(t_0) = I$, then Jacobian corresponding to one period J_p is just the exponential part e^{TB} in theorem A.1. This is the theoretical basis of periodic eigendecomposition algorithm, which tries to calculate the eigenvalues and eigenvectors of J_p. On the other hand, the periodic part $P(t)$ in theorem A.1 evolves Floquet vectors along the periodic orbit, and returns to the initial value after one period. This information is revealed in the reordering stage of periodic eigendecomposition algorithm.

APPENDIX B

PROOF OF PROPOSITION 4.2

The proof of proposition 4.2 provided by Collet *et al.* [17] concerns the calculation in the Fourier space. Let

$$v(x,t) = i \sum_{n=-\infty}^{\infty} v_n(t) e^{inqx} \,, \quad \Phi_x(x) = -\sum_{n=-\infty}^{\infty} \psi_n e^{inqx}$$

with $q = 2\pi/L$. Here, we modify the form of Fourier transform by taking into consideration the fact that both $v(x,t)$ and $\Phi(x)$ are antisymmetric. Therefore, v_n and ψ_n are all real numbers and we have relations

$$v_n = -v_{-n} \,, \quad \psi_n = \psi_{-n} \,. \tag{172}$$

We also impose $\psi_0 = 0$. Note that we define the Fourier mode for $\Phi_x(x)$ not $\Phi(x)$. With this setup, now we try to prove (148). We first calculate $\int v^2 \Phi_x(x)$ and $\int v(\partial_x^2 + \partial_x^4)v$.

$$\begin{aligned} \int v^2 \Phi_x(x) &= \sum_{k,l,m} \int v_k v_l \psi_m e^{i(k+l+m)qx} \\ &= L \sum_{k+l+m=0} v_k v_l \psi_m = L \sum_{k,l} v_k v_l \psi_{-k-l} = L \sum_{k,l} v_k v_l \psi_{|k+l|} \,. \end{aligned}$$

$$\begin{aligned} \int v(\partial_x^2 + \partial_x^4)v &= \sum_{k,l} \int v_k(-n^2q^2 + n^4q^4) v_l e^{i(k+l)qx} \\ &= L \sum_{k} (-n^2q^2 + n^4q^4) v_k^2 \,. \end{aligned}$$

In the above derivation, we have used relation (172) and $\psi_0 = 0$. Then

$$\begin{aligned} (v,v)_{\gamma\Phi} &= \int v(\partial_x^2 + \partial_x^4 + \gamma\Phi_x)v \\ &= L \sum_{k} (-n^2q^2 + n^4q^4) v_k^2 + \gamma L \sum_{k,l} v_k v_l \psi_{|k+l|} \\ &= 2L \sum_{k>0} (-n^2q^2 + n^4q^4) v_k^2 + \gamma L \sum_{k,l>0} v_k v_l (\psi_{|k+l|} + \psi_{|-k-l|} - \psi_{|k-l|} - \psi_{|-k+l|}) \\ &= 2L \left(\sum_{k>0} (-n^2q^2 + n^4q^4) v_k^2 + \gamma \sum_{k,l>0} v_k v_l (\psi_{|k+l|} - \psi_{|k-l|}) \right) \\ &= 2L \left(\sum_{k>0} (-n^2q^2 + n^4q^4 + \gamma\psi_{2k}) v_k^2 + \gamma \sum_{\substack{k,l>0 \\ k\neq m}} v_k v_l (\psi_{|k+l|} - \psi_{|k-l|}) \right) \\ &= 2L \left(\sum_{k>0} (-n^2q^2 + n^4q^4 + \gamma\psi_{2k}) v_k^2 + 2\gamma \sum_{k>l>0} v_k v_l (\psi_{k+l} - \psi_{|k-l|}) \right) \end{aligned} \tag{173}$$

and

$$\begin{aligned}\frac{1}{4}\int(v_{xx}^2+v^2) &= -\frac{1}{4}\sum_{k,l}\int v_k(n^4q^4+1)v_l e^{i(k+l)qx}\\ &= \frac{L}{4}\sum_k (n^4q^4+1)v_k^2\\ &= \frac{L}{2}\sum_{k>0}(n^4q^4+1)v_k^2\,. \end{aligned}\tag{174}$$

In order to show $(v,v)_{\gamma\Phi} \geq \frac{1}{4}\int(v_{xx}^2+v^2)$, we choose as ψ_n as follows

$$\psi_n = \begin{cases} 0, & \text{for } n \text{ odd}\\ \begin{cases} 4, & \text{when } 1 \leq |n| \leq 2M \\ 4f(|n|/2M-1), & \text{when } 2M \leq |n| \end{cases}, & \text{for } n \text{ even} \end{cases}. \tag{175}$$

Here $f(n)$ is a non-increasing function whose first-order derivative is continuous. It satisfies $f(0)=1,\ f'(0)=0$ and

$$f \geq 0\,, \quad \sup|f'| < 1\,, \quad \int_0^\infty dk(1+k)^2|f(k)|^2 < \infty\,. \tag{176}$$

Integer M satisfies

$$M \geq \frac{2}{q} \tag{177}$$

and its exact value will be determined later. Therefore

$$\begin{aligned}-n^2q^2+n^4q^4+\gamma\psi_{2k} &= \frac{1}{2}(n^2q^2-1)^2+\frac{1}{2}(n^4q^4+1)+\gamma\psi_{2k}-1\\ &\geq \frac{1}{2}(n^4q^4+1)\,.\end{aligned}$$

Here, we have used the fact that $\psi_{2k} > 0$ when $nq > 2$ and $\psi_{2k} > 4$ when $nq \leq 2$ together with $\gamma \in [1/4, 1]$. With this inequality, we try to give lower bound of (173). Before that, for notation convenience, we define

$$\tau_n = \sqrt{\frac{q^4n^4+1}{2}}\,, \quad \omega_n = \tau_n v_n\,. \tag{178}$$

Then from (173) we have

$$(v,v)_{\gamma\Phi} \geq 2L\left(\sum_{k>0}\omega_k^2 + 2\gamma\sum_{k>l>0}\omega_k\frac{\psi_{k+l}-\psi_{|k-l|}}{\tau_k\tau_l}\omega_l\right)\,.$$

and (174) becomes

$$\frac{1}{4}\int(v_{xx}^2+v^2) = L\sum_{k>0}\omega_k^2\,.$$

In order to make $(v,v)_{\gamma\Phi} \geq \frac{1}{4}\int(v_{xx}^2+v^2)$, we need to prove

$$\sum_{k>0}\omega_k^2 + 4\gamma\sum_{k>l>0}\omega_k\frac{\psi_{k+l}-\psi_{|k-l|}}{\tau_k\tau_l}\omega_l > 0$$

for $\gamma \in [1/4, 1]$. One sufficient but not necessary condition is

$$\sum_{k>l>0} \left| \frac{\psi_{k+l} - \psi_{|k-l|}}{\tau_k \tau_l} \right|^2 < \frac{1}{16}\,.$$

Now, we show that the above relation is valid given the choice of ψ_k in (175).

$$\begin{aligned}
&\sum_{k>l>0} \left| \frac{\psi_{k+l} - \psi_{|k-l|}}{\tau_k \tau_l} \right|^2 \\
&= \sum_{m=1}^{\infty} \tau_m^{-2} \sum_{k=m+1}^{\infty} (\psi_{k+m} - \psi_{k-m})^2 \tau_k^{-2} \\
&\leq \frac{16}{M^2} \sum_{m=1}^{M} m^2 \tau_m^{-2} \sum_{k=2M-m+1}^{\infty} \tau_k^{-2} + \frac{16}{M^2} \sum_{m=M+1}^{\infty} m^2 \tau_m^{-2} \sum_{k=m+1}^{\infty} \tau_k^{-2} \\
&\leq \frac{16}{M^2} \sum_{m=1}^{M} m^2 \tau_m^{-2} \int_{2M-m}^{\infty} \tau_k^{-2} dk + \frac{16}{M^2} \sum_{m=M+1}^{\infty} m^2 \tau_m^{-2} \int_{m}^{\infty} \tau_k^{-2} dk \\
&= \frac{32}{M^2} \sum_{m=1}^{M} m^2 \tau_m^{-2} \int_{2M-m}^{\infty} \frac{1}{q^4 k^4 + 1} dk + \frac{32}{M^2} \sum_{m=M+1}^{\infty} m^2 \tau_m^{-2} \int_{m}^{\infty} \frac{1}{q^4 k^4 + 1} dk \\
&\leq \frac{32}{M^2} \sum_{m=1}^{M} m^2 \tau_m^{-2} \int_{2M-m}^{\infty} \frac{1}{q^4 k^4} dk + \frac{32}{M^2} \sum_{m=M+1}^{\infty} m^2 \tau_m^{-2} \int_{m}^{\infty} \frac{1}{q^4 k^4} dk \\
&= \frac{32}{3M^2 q^4} \sum_{m=1}^{M} m^2 \tau_m^{-2} \frac{1}{(2M-m)^3} + \frac{32}{3M^2 q^4} \sum_{m=M+1}^{\infty} m^2 \tau_m^{-2} \frac{1}{m^3} \\
&\leq \frac{32}{3M^5 q^4} \sum_{m=1}^{M} m^2 \tau_m^{-2} + \frac{32}{3M^2 q^4} \sum_{m=M+1}^{\infty} m^{-1} \tau_m^{-2} \\
&\leq \frac{64}{3M^5 q^4} \int_0^{\infty} \frac{m^2}{q^4 m^4 + 1} dm + \frac{64}{3M^2 q^4} \int_M^{\infty} \frac{1}{m(q^4 m^4 + 1)} dm \\
&\leq \frac{64}{3M^5 q^4} \int_0^{\infty} \frac{m^2}{(q^4 m^4 + 1)^{1/2} (q^4 m^4)^{1/2}} dm + \frac{64}{3M^2 q^4} \int_M^{\infty} \frac{1}{m(q^4 m^4)} dm \\
&\leq \frac{64}{3M^5 q^6} \int_0^{\infty} \frac{1}{(q^4 m^4 + 1)^{1/2}} dm + \frac{16}{3M^6 q^8} \\
&= \frac{64}{3M^5 q^6} \frac{4\Gamma(\frac{5}{4})^2}{\sqrt{\pi} q} + \frac{16}{3M^6 q^8} \\
&< \frac{128}{3M^5 q^7} + \frac{16}{3M^6 q^8}\,.
\end{aligned}$$

We choose M to be the smallest integer larger than $4q^{-7/5} = 4(L/2\pi)^{7/5}$, then

$$\frac{128}{3M^5 q^7} + \frac{16}{3M^6 q^8} < \frac{128}{3 \cdot 4^5} + \frac{16}{3 \cdot 4^6 q^{-2/5}} < \frac{11}{256} < \frac{1}{16}\,.$$

In the above derivation, we have used the fact that $q = 2\pi/L < 1$. Also, note that the choice of M here satisfies the requirement (177). Therefore, (148) in proposition 4.2 is validated. Now we turn to the proof of (149).

$$
\begin{aligned}
(\Phi, \Phi)_{\gamma\Phi} &= \int_0^L \Phi(\partial_x^2 + \partial_x^4)\Phi dx \\
&= -\int_0^L \Phi_x(\partial_x + \partial_x^3)\Phi dx \\
&= -\int_0^L \sum_{m,n} \psi_m (1 - n^2 q^2)\psi_n e^{i(m+n)qx} dx \\
&= 2L \sum_{n=1}^{\infty} (n^2 q^2 - 1)\psi_n^2 \\
&= 2L \left(\sum_{n=1}^{2M} (n^2 q^2 - 1) 16 + \sum_{n=2M+1}^{\infty} (n^2 q^2 - 1) 16 f^2 (\frac{n}{2M} - 1) \right) \\
&\leq 32L \left(2M(2M)^2 q^2 + \int_{2M+1}^{\infty} dn (n^2 q^2 - 1) f^2 (\frac{n}{2M} - 1) \right) \\
&\leq 32L \left(8M^3 q^2 + \int_0^{\infty} dn 2M((n+1)^2 4M^2 q^2 - 1) f^2(n) \right) \\
&\leq 256 L M^3 q^2 \left(1 + \int_0^{\infty} dn (n+1)^2 f^2(n) \right) \\
&= 256 L \left(4 (\frac{2\pi}{L})^{-7/5} \right)^3 \left(\frac{2\pi}{L} \right)^2 \left(1 + \int_0^{\infty} dn (n+1)^2 f^2(n) \right) \\
&= K L^{16/5} \left(1 + \int_0^{\infty} dn (n+1)^2 f^2(n) \right) .
\end{aligned}
$$

From (176), we know that (149) is verified. Thus, we finish the proof of proposition 4.2.

References

[1] P. Amodio, J. R. Cash, G. Roussos, R. W. Wright, G. Fairweather, I. Gladwell, G. L. Kraut, and M. Paprzycki, "Almost block diagonal linear systems: sequential and parallel solution techniques, and applications", Numer. Linear Algebra Appl. **7**, 275–317 (2000).

[2] I. S. Aranson and L. Kramer, "The world of complex Ginzburg-Landau equation", Rev. Mod. Phys. **74**, 99–143 (2002).

[3] R. Artuso, E. Aurell, and P. Cvitanović, "Recycling of strange sets: I. Cycle expansions", Nonlinearity **3**, 325–359 (1990).

[4] R. Artuso, E. Aurell, and P. Cvitanović, "Recycling of strange sets: II. Applications", Nonlinearity **3**, 361–386 (1990).

[5] G. Benettin, L. Galgani, A. Giorgilli, and J. M. Strelcyn, "Lyapunov characteristic exponents for smooth dynamical systems and for Hamiltonian systems; a method for computing all of them. Part 1: theory", Meccanica **15**, 9–20 (1980).

[6] A. Björck and G. H. Golub, "Numerical methods for computing angles between linear subspaces", Math. Comput. **27**, 579–594 (1973).

[7] J. Bochi and M. Viana, "How frequently are dynamical systems hyperbolic?", in *Modern dynamical systems and applications*, edited by M. Brin, B. Hasselblatt, and Y. Pesin (Cambridge Univ. Press, Cambridge, 2004), pp. 271–297.

[8] A. Bojanczyk, G. H. Golub, and P. V. Dooren, The periodic Schur decomposition. Algorithms and applications, in Proc. SPIE Conference (1992), pp. 31–42.

[9] H. Bosetti and H. A. Posch, "What does dynamical systems theory teach us about fluids?", Commun. Theor. Phys. **62**, 451–468 (2014).

[10] J. C. Bronski and T. N. Gambill, "Uncertainty estimates and L_2 bounds for the Kuramoto-Sivashinsky equation", Nonlinearity **19**, 2023–2039 (2006).

[11] N. B. Budanur, Exact Coherent Structures in Spatiotemporal Chaos: From Qualitative Description to Quantitative Predictions, PhD thesis (School of Physics, Georgia Inst. of Technology, Atlanta, 2015).

[12] N. B. Budanur and P. Cvitanović, "Unstable manifolds of relative periodic orbits in the symmetry-reduced state space of the Kuramoto-Sivashinsky system", J. Stat. Phys., 1–20 (2015).

[13] N. B. Budanur, D. Borrero-Echeverry, and P. Cvitanović, "Periodic orbit analysis of a system with continuous symmetry - A tutorial", Chaos **25**, 073112 (2015).

[14] N. B. Budanur, P. Cvitanović, R. L. Davidchack, and E. Siminos, "Reduction of the SO(2) symmetry for spatially extended dynamical systems", Phys. Rev. Lett. **114**, 084102 (2015).

[15] G. J. Chandler and R. R. Kerswell, "Invariant recurrent solutions embedded in a turbulent two-dimensional Kolmogorov flow", J. Fluid Mech. **722**, 554–595 (2013).

[16] F. Christiansen, P. Cvitanović, and V. Putkaradze, "Spatiotemporal chaos in terms of unstable recurrent patterns", Nonlinearity **10**, 55–70 (1997).

[17] P. Collet, J. P. Eckmann, H. Epstein, and J. Stubbe, "A global attracting set for the Kuramoto-Sivashinsky equation", Commun. Math. Phys. **152**, 203–214 (1993).

[18] P. Constantin, C. Foias, B. Nicolaenko, and R. Temam, *Integral manifolds and inertial manifolds for dissipative partial differential equations* (Springer, New York, 1989).

[19] S. M. Cox and P. C. Matthews, "Exponential time differencing for stiff systems", J. Comput. Phys. **176**, 430–455 (2002).

[20] M. C. Cross and P. C. Hohenberg, "Pattern formation outside of equilibrium", Rev. Mod. Phys. **65**, 851–1112 (1993).

[21] P. Cvitanović, R. L. Davidchack, and E. Siminos, "On the state space geometry of the Kuramoto-Sivashinsky flow in a periodic domain", SIAM J. Appl. Dyn. Syst. **9**, 1–33 (2010).

[22] P. Cvitanović, R. Artuso, R. Mainieri, G. Tanner, and G. Vattay, *Chaos: Classical and Quantum* (Niels Bohr Inst., Copenhagen, 2017).

[23] R. L. Devaney, Chaos in the Classroom, Boston Univ. 1995.

[24] X. Ding and P. Cvitanović, "Periodic eigendecomposition and its application in Kuramoto-Sivashinsky system", SIAM J. Appl. Dyn. Syst. **15**, 1434–1454 (2016).

[25] X. Ding and P. Cvitanović, Exploding relative periodic orbits in cubic-quintic complex Ginzburg–Landau equation, In preparation, 2017.

[26] X. Ding and S. H. Kang, Adaptive time-stepping exponential integrators for cubic-quintic complex Ginzburg–Landau equations, 2017.

[27] X. Ding, H. Chaté, P. Cvitanović, E. Siminos, and K. A. Takeuchi, "Estimating the dimension of the inertial manifold from unstable periodic orbits", Phys. Rev. Lett. **117**, 024101 (2016).

[28] J.-P. Eckmann and D. Ruelle, "Ergodic theory of chaos and strange attractors", Rev. Mod. Phys. **57**, 617–656 (1985).

[29] S. V. Ershov and A. B. Potapov, "On the concept of stationary Lyapunov basis", Physica D **118**, 167–198 (1998).

[30] G. Fairweather and I. Gladwell, "Algorithms for almost block diagonal linear systems", SIAM Rev. **46**, 49–58 (2004).

[31] J. D. Farmer, E. Ott, and J. A. Yorke, "The dimension of chaotic attractors", in *The theory of chaotic attractors*, edited by B. R. Hunt, T.-Y. Li, J. A. Kennedy, and H. E. Nusse (Springer, New York, 1983), pp. 142–169.

[32] G. Floquet, "Sur les équations différentielles linéaires à coefficients périodiques", Ann. Sci. Ec. Norm. Sér **12**, 47–88 (1883).

[33] C. Foias, B. Nicolaenko, G. R. Sell, and R. Temam, "Inertial manifold for the Kuramoto-Sivashinsky equation", C. R. Acad. Sci. Paris, Ser. I **301**, 285–288 (1985).

[34] C. Foias, G. R. Sell, and R. Temam, "Inertial manifolds for nonlinear evolutionary equations", J. Diff. Equ. **73**, 309–353 (1988).

[35] C. Foias, B. Nicolaenko, G. R. Sell, and R. Temam, "Inertial manifolds for the Kuramoto-Sivashinsky equation and an estimate of their lowest dimension", J. Math. Pure Appl. **67**, 197–226 (1988).

[36] C. Foias, M. S. Jolly, I. G. Kevrekidis, G. R. Sell, and E. S. Titi, "On the computation of inertial manifolds", Phys. Lett. A **131**, 433–436 (1988).

[37] J. G. F. Francis, "The QR transformation: A unitary analogue to the LR transformation. I", Comput. J. **4**, 265–271 (1961).

[38] P. Frederickson, J. L. Kaplan, E. D. Yorke, and J. A. Yorke, "The Liapunov dimension of strange attractors", J. Diff. Eqn. **49**, 185–207 (1983).

[39] L. Giacomelli and F. Otto, "New bounds for the Kuramoto-Sivashinsky equation", Commun. Pure Appl. Math. **58**, 297–318 (2005).

[40] J. F. Gibson, J. Halcrow, and P. Cvitanović, "Visualizing the geometry of state-space in plane Couette flow", J. Fluid Mech. **611**, 107–130 (2008).

[41] F. Ginelli, P. Poggi, A. Turchi, H. Chaté, R. Livi, and A. Politi, "Characterizing dynamics with covariant Lyapunov vectors", Phys. Rev. Lett. **99**, 130601 (2007).

[42] F. Ginelli, H. Chaté, R. Livi, and A. Politi, "Covariant Lyapunov vectors", J. Phys. A **46**, 254005 (2013).

[43] J. Goodman, "Stability of the Kuramoto-Sivashinsky and related systems", Commun. Pure Appl. Math. **47**, 293–306 (1994).

[44] R. Granat and B. Kågström, "Direct eigenvalue reordering in a product of matrices in periodic Schur form", SIAM J. Matrix Anal. Appl. **28**, 285–300 (2006).

[45] R. Granat, I. Jonsson, and B. Kågström, "Recursive blocked algorithms for solving periodic triangular Sylvester-type matrix equations", in *Applied Parallel Computing. State of the Art in Scientific Computing* (Springer, New York, 2007), pp. 531–539.

[46] P. Grassberger and I. Procaccia, "Characterization of strange attractors", Phys. Rev. Lett. **50**, 346–349 (1983).

[47] M. Hamermesh, *Group Theory and Its Application to Physical Problems* (Dover, New York, 1962).

[48] M. Hochbruck and A. Ostermann, "Exponential integrators", Acta Numerica **19**, 209–286 (2010).

[49] B. R. Hunt, "Maximum local Lyapunov dimension bounds the box dimension of chaotic attractors", Nonlinearity **9**, 845–852 (1996).

[50] M. Jolly, R. Rosa, and R. Temam, "Evaluating the dimension of an inertial manifold for the Kuramoto-Sivashinsky equation", Advances in Differential Equations **5**, 31–66 (2000).

[51] J. L. Kaplan and J. A. Yorke, "Chaotic behavior of multidimensional difference equations", in *Functional differential equations and approximation of fixed points*, Vol. 730, edited by H.-O. Peitgen and H.-O. Walther, Lect. Notes Math. (Springer, Berlin, 1979), pp. 204–227.

[52] A.-K. Kassam and L. N. Trefethen, "Fourth-order time-stepping for stiff PDEs", SIAM J. Sci. Comput. **26**, 1214–1233 (2005).

[53] A. V. Knyazev and M. E. Argentati, "Principal angles between subspaces in an A-based scalar product: Algorithms and perturbation estimates", SIAM J. Sci. Comput. **23**, 2008–2040 (2002).

[54] P. V. Kuptsov and U. Parlitz, "Theory and computation of covariant Lyapunov vectors", J. Nonlinear Sci. **22**, 727–762 (2012), http://arXiv.org/abs/1105.5228.

[55] Y. Kuramoto and T. Tsuzuki, "On the formation of dissipative structures in reaction–diffusion systems", Progr. Theor. Phys. **54**, 687–699 (1975).

[56] Y. Lan and P. Cvitanović, "Unstable recurrent patterns in Kuramoto-Sivashinsky dynamics", Phys. Rev. E **78**, 026208 (2008).

[57] L. D. Landau and E. M. Lifshitz, *Fluid mechanics* (Pergamon Press, Oxford, 1959).

[58] R. E. LaQuey, S. M. Mahajan, P. H. Rutherford, and W. M. Tang, "Nonlinear saturation of the trapped-ion mode", Phys. Rev. Lett. **34**, 391–394 (1974).

[59] K Levenberg, "A method for the solution of certain non-linear problems in least squares", Quart. Appl. Math. **2**, 164–168 (1944).

[60] K. Lust, "Improved numerical Floquet multipliers", Int. J. Bifur. Chaos **11**, 2389–2410 (2001).

[61] M. Marion and R. Temam, "Nonlinear Galerkin methods", SIAM J. Numer. Anal. **26**, 1139–1157 (1989).

[62] D. M. Marquardt, "An algorithm for least-squares estimation of nonlinear parameters", J. Soc. Indust. Appl. Math. **11**, 431–441 (1963).

[63] D. M. Michelson and G. I. Sivashinsky, "Nonlinear analysis of hydrodynamic instability in laminar flames—II. Numerical experiments", Acta Astronaut. **4**, 1207–1221 (1977).

[64] H. Montanelli and N. Bootland, Solving stiff PDEs in 1D, 2D and 3D with exponential integrators, 2016.

[65] B. Nicolaenko, B. Scheurer, and R. Temam, "Some global dynamical properties of the Kuramoto-Sivashinsky equations: nonlinear stability and attractors", Physica D **16**, 155–183 (1985).

[66] V. I. Oseledec, "A multiplicative ergodic theorem. Liapunov characteristic numbers for dynamical systems", Trans. Moscow Math. Soc. **19**, 197–221 (1968).

[67] F. Otto, "Optimal bounds on the KuramotoSivashinsky equation", J. Funct. Anal. **257**, 2188–2245 (2009).

[68] C. Pugh, M. Shub, and A. Starkov, "Stable ergodicity", Bull. Amer. Math. Soc **41**, 1–41 (2004).

[69] J. C. Robinson, "Inertial manifolds for the Kuramoto-Sivashinsky equation", Phys. Lett. A **184**, 190–193 (1994).

[70] J. C. Robinson, "Finite-dimensional behavior in dissipative partial differential equations", Chaos **5**, 330–345 (1995).

[71] J. C Robinson, *Infinite-dimensional dynamical systems: An introduction to dissipative parabolic PDEs and the theory of global attractors* (Cambridge Univ. Press, 2001).

[72] D. Ruelle, "Ergodic theory of differentiable dynamical systems", Publ. Math. IHES **50**, 27–58 (1979).

[73] D. A. Russell, J. D. Hanson, and E. Ott, "Dimension of strange attractors", Phys. Rev. Lett. **45**, 1175–1178 (1980).

[74] Y. Saad and M. H. Schultz, "GMRES: A generalized minimal residual algorithm for solving nonsymmetric linear systems", SIAM J. Sci. Stat. Comput. **7**, 856–869 (1986).

[75] T. Shlang and G. I. Sivashinsky, "Irregular flow of a liquid film down a vertical column", J. Physique **43**, 459–466 (1982).

[76] B. I. Shraiman, A. Pumir, W. van Saarloos, P. C. Hohenberg, H. Chaté, and M. Holen, "Spatiotemporal chaos in the one-dimensional complex Ginzburg-Landau equation", Physica D **57**, 241–248 (1992).

[77] J. P. Simonisk, Inexact Newton Methods Applied to Under-Determined Systems, PhD thesis (Polytechnic Inst., Worcester, MA, 2006).

[78] Y. G. Sinai, *Introduction to Ergodic Theory* (Princeton Univ. Press, Princeton, 1976).

[79] K. A. Takeuchi, H. L. Yang, F. Ginelli, G. Radons, and H. Chaté, "Hyperbolic decoupling of tangent space and effective dimension of dissipative systems", Phys. Rev. E **84**, 046214 (2011).

[80] R. Temam, "Inertial manifolds", Math. Intelligencer **12**, 68–74 (1990).

[81] R. Temam, *Infinite-Dimensional Dynamical Systems in Mechanics and Physics*, 2nd ed. (Springer, New York, 2013).

[82] M. Tinkham, *Group theory and quantum mechanics* (Dover, New York, 2003).

[83] L. N. Trefethen, *Spectral Methods in MATLAB* (SIAM, Philadelphia, 2000).

[84] L. N. Trefethen and D. Bau, *Numerical Linear Algebra* (SIAM, Philadelphia, 1997).

[85] D. S. Watkins, "Francis's algorithm", Amer. Math. Monthly **118**, 387–403 (2011).

[86] A. P. Willis, K. Y. Short, and P. Cvitanović, "Symmetry reduction in high dimensions, illustrated in a turbulent pipe", Phys. Rev. E **93**, 022204 (2016).

[87] C. L. Wolfe and R. M. Samelson, "An efficient method for recovering Lyapunov vectors from singular vectors", Tellus A **59**, 355–366 (2007).

[88] H.-l. Yang and G. Radons, "Comparison between covariant and orthogonal Lyapunov vectors", Phys. Rev. E **82**, 046204 (2010), http://arXiv.org/abs/1008.1941.

[89] H. L. Yang and G. Radons, "Geometry of inertial manifold probed via Lyapunov projection method", Phys. Rev. Lett. **108**, 154101 (2012).

[90] H. L. Yang, K. A. Takeuchi, F. Ginelli, H. Chaté, and G. Radons, "Hyperbolicity and the effective dimension of spatially extended dissipative systems", Phys. Rev. Lett. **102**, 074102 (2009).